Numerical and Experimental Study of Contact Maturing in Sand

by

Dowon Park

A dissertation submitted in partial fulfillment
of the requirements for the degree of
Doctor of Philosophy
(Civil Engineering)
in the University of Michigan
2019

Doctoral Committee:

Professor Radoslaw L. Michalowski, Chair
Associate Professor Adda Athanasopoulos-Zekkos
Professor James R. Barber
Professor Roman Hryciw

Dowon Park

dowon@umich.edu

ORCID iD: 0000-0002-5513-5848

DEDICATION

To my family

Christina Sungrye Ahn and Leo Ihyun Park.

ACKNOWLEDGEMENTS

This PhD study would not have been possible without the support and nurturing that I received from many people. I would like to first express a very big thank you to my supervisor, Professor Radoslaw Michalowski, for endless support. Professor Michalowski, who has unparalleled knowledge, intuition, and patience, always inspired me by his curiosity, enthusiasm, and hardworking. In addition to academic supervision, I express my deepest appreciation for his warm care. I owe him a great debt of gratitude. I would also like to extend my sincere thanks to my dissertation committee members, Professors Adda Athanasopoulos-Zekkos, James Barber, and Roman Hryciw, for brilliant comments and suggestions that provide the basis of my PhD study: numerical modeling and contact mechanics. Their invaluable advices and feedback enabled me to overcome numerous obstacles I have been facing through each stage of the process. I would like to acknowledge other faculty members, especially Professors Richard Woods and Dimitrios Zekkos, for inspiring my interest in the new subjects, and nurturing me. I am indebted to Professor Seung-Rae Lee who gave me passion to pursue academic career during my M.S. degree. Thanks to him, I realized that geotechnical engineering is something I will devote my entire life to.

Special thanks go to Dr. Zhijie Wang for his useful contributions and fruitful discussions. I thank Geotech Group colleagues for friendship. It is a great fortune to have known you since I started my studies in Ann Arbor four years ago. Also, I would like to thank other friends making my life in Ann Arbor enjoyable. I have many pleasant memories and I am always with you.

I cannot begin to express my thanks to my family, Christina Sungrye Ahn and Leo Ihyun Park, for unconditional love. My deep and sincere gratitude goes to my parents for selflessly encouraging me to pursue my studies. It is a pleasure to thank my parents-in-law who pray for me and always show support.

I would like to acknowledge the research support from the National Science Foundation, Grants Nos. 1537222 and 1901582 from the Civil, Mechanical and Manufacturing Innovation Program (CMMI) of the Directorate for Engineering, and the Rackham Predoctoral Fellowship from U-M Horace Rackham School of Graduate Studies.

TABLE OF CONTENTS

LIST OF TABLES

LIST OF FIGURES

ABSTRACT

While time effects in silica sand are well documented, there is a distinct knowledge gap in regards to understanding the mechanisms that promote the time-dependent behavior of sand. A *contact maturing hypothesis*, also referred to as *static fatigue hypothesis*, is advocated in this study, with an emphasis on the time-dependent behavior of inter-granular contacts. The rich surface texture of silica sand grains makes the surface asperities vulnerable to sub-critical fracturing, which is manifested as a delayed response to sustained loads. The study focuses on understanding the contact maturing process and the mechanism that bridges the microscopic contact maturing to the mesoscale sand ageing. Laboratory observations and testing showed time-dependent fracturing and crushing of asperities at contacts, supporting the contact maturing hypothesis. Numerical models were constructed to mimic the maturing process of individual contacts. The study not only supports static fatigue hypothesis as a key cause of the time-dependent behavior of sands, but also improves the current understanding of underlying mechanisms of time and size dependent frictional behavior in rocks. The time-dependent increasing number of contact points attributed to delayed fracturing of contact asperities leads to stronger and stiffer inter-granular contacts, thereby increasing macroscopic stiffness.

Chapter 1

Introduction

1.1. Background and Motivation

Sands have a tendency to change their properties over time, the effect often referred to as “sand aging” in geotechnical engineering. Accounting for sand aging in the development of construction sites and pile foundation systems would lead to economic benefits, but the aging process is not fully understood. Sand aging is ubiquitous in natural environments and it particularly affects the behavior of freshly deposited or disturbed sand (e.g., after compaction). Substantial changes in small strain stiffness, cone penetration resistance, and liquefaction resistance have been observed after sand compaction at various construction sites. Associated with sand aging is also an increase in shaft resistance of displacement foundation piles, where the shaft capacity of the pile may double within one year. This research focuses on the fundamental understanding of the phenomenon, collecting evidence to support the working hypothesis, and on the development of numerical capabilities for predicting the time effects in sand.

Various hypotheses were suggested in the last several decades to explain the phenomenon of sand aging, among them: chemical cementation at sand grain contacts due to mineral precipitation (Mitchell and Solymar, 1984), time-dependent changes in the structure of grain assemblies (Mesri et al., 1990, Schmertmann, 1991, Bowman and Soga, 2003), microbiological

processes (Kroll, 1990, Mitchell and Santamarina, 2005, DeJong et al., 2006), time-dependent fracturing of grains (Lade and Karimpour, 2010), and, most recently, static fatigue at the contacts between sand grains (Michalowski et al., 2018b). However, there has been no consensus on the driving mechanisms behind this phenomenon. Predicting consequences of sand aging is not possible without thorough understanding of the mechanisms causing the process; therefore, the overarching objective of this research is to identify the key mechanisms responsible for time-dependent evolution of sand properties and to apply them to practical engineering problems at the macro-scale.

1.2. Dissertation organization

This thesis begins by examining the literature regarding the time-dependent behavior of sand (Chapter 2). The chapter gives a brief overview of the recent history of those topics. It will then go on to research objectives of this dissertation (Chapter 3). The next three chapters (Chapter 4-6) are concerned with contact maturing hypothesis as a key cause of the time-dependent behavior of sands.

Chapter 4 presents qualitative and quantitative evidence of contact maturing hypothesis obtained from the laboratory observation and testing. The microscopic observation of grain surfaces before and after sustained loading showed: (i) a rich texture of surface morphology, and (ii) surface damage and asperity crushing at contact, supporting the hypothesis. The statistical approach sheds light on the effect of aging time on contact evolution. Grain-scale laboratory experiments indicate that the time-dependent response of single grain are strongly dependent on roughness of grain surfaces.

Chapter 5 addresses the development of numerical tools to capture key characteristics of contact maturing process at grain contacts. A hybrid model introduced in this study successfully estimates grain convergence caused by both creep in grain core material and micro-fracturing of contact asperities. The simulation results indicate the increased number of contacts and associated force chains, leading to stiffer contacts. Last, but not least, a preliminary study for delayed grain split is carried out. The suggested model is a complementary tool in the way that it can reproduce

a valuable information that cannot be tracked with physical tests and predict contact behaviors for a very long time span.

In Chapter 6, a discrete asperity model is introduced and validated with the literature. Based on the physical parameters obtained from the statistical analysis, it is implemented for the grain-scale laboratory experiments to understand the time-dependent contact behavior on the nominal contact. Discrete asperity model, also examines frictional aging simulation in rocks. In addition to two plausible mechanisms responsible for the frictional aging in the literature, increase in contact area and strengthening of contact bond, the increased number of contact points is also taken into account for time-dependent analysis of geomaterials. In the simulation, the influence of three mechanisms on the contact strength and stiffness is studied.

Chapter 7 serves as the summary and conclusions of this dissertation. This chapter summarizes findings in this study, and highlights achievements and contributions to the topics. Lastly, the directions of future research and recommendations are discussed.

Chapter 2

Literature Review

The existing literature on the time effects of sand is extensive and focuses particularly on sand aging. Awareness of sand aging is not recent, having noticeably been observed in the Jebba Dam hydroelectric project development on the Niger River, Nigeria, by Mitchell and Solymar (1984). Since then, a considerable amount of literature has been published on the field and laboratory observations of sand aging, and they are summarized in this chapter. These studies report the time-dependent changes of the soil stiffness (Afifi and Woods, 1971, Afifi and Richart, 1973, Anderson and Stokoe, 1978, Mesri et al., 1990, Jamiolkowski et al., 1995, Daramola, 1980, Howie et al., 2002, Baxter and Mitchell, 2004), penetration resistance (Denisov et al., 1963, Mitchell and Solymar, 1984, Skempton, 1986, Dowding and Hryciw, 1986, Dumas and Beaton, 1988, Schmertmann, 1991, Charlie et al., 1992, Joshi et al., 1995, Baxter and Mitchell, 2004, Ashford et al., 2004, Narsilio et al., 2009), shear strength (Daramola, 1980), liquefaction resistance (Seed, 1979, Arango et al., 2000, Leon et al., 2006), and pile setup (Tavenas and Audy, 1972, Chow et al., 1998, Axelsson, 2000, Bowman and Soga, 2005, Jardine et al., 2006, Zhang and Wang, 2014). Collectively, these studies outline a critical role for time effect in sands, but a key mechanism of the time effect is yet to be determined.

2.1. Field and laboratory measurements of time effects in sand

Soils stiffness

It has been demonstrated in the literature that sand aging results in the increase in the soil stiffness over time. An experimental demonstration of the time-dependent stiffness increase was possibly first carried out by Afifi and Woods (1971). They conducted long-term resonant column tests on sand samples confined for different durations. The measured shear modulus of different aged samples increased as a logarithmic function of time up to 430 days, whereas no measurable change in vertical strain was observed during the tests as shown in Fig. 2.1. This indicated that the increase in shear modulus can be achieved without a volume change associated with the change in the void ratio. The magnitude of the shear modulus growth is more intense when the particle size of samples is small; 2-5 % increase in air-dry sands and 5-12% increase in silts after 1,000 minutes of initial consolidation stage.

In the subsequent paper, Afifi and Richart (1973) examined the effect of time on soil stiffness considering a wide range of soils with different grain sizes, loading and consolidation time. In the resonant column tests, they measured the dynamic shear modulus at small-strain (G) over time. In the case of the soils with grain size greater than 0.04 mm, a little increase in the small-strain shear modulus was observed with increase in the time of the confining pressure. This type of soils showed negligible influence of consolidation time on shear modulus. For the finer soils with median grain size smaller than 0.04 mm, on the other hands, both influences of aging time and consolidation on the shear modulus were significant on the small-strain dynamic shear modulus.

In the same vein, Anderson and Stokoe (1978) carried out a number of resonant column tests to characterize the quantitative increase of small-strain shear modulus with time. The results showed that the increase of time-dependent shear modulus can be determined as follows

$$N_G = \frac{\Delta G}{G_{1000}} / \log(\frac{t_2}{t_{1000}}) \tag{2.1}$$

$$G_t = G_{1000}(1 + N_G \log\frac{t_2}{t_{1000}}) \tag{2.2}$$

where N_G is the dimensionless ratio of normalized shear modulus increase with time, t_{1000} is a reference time associated with 1,000 minutes primary consolidation, t_2 is a time of interest thereafter, ΔG is the increase in the shear modulus from t_2 to t_{1000}, G_t and G_{1000} are the small strain shear moduli at t_2 and t_{1000}, respectively. Mesri et al. (1990) reported the typical value of N_G for clean silts and sands is N_G = 0.02-0.03. Jamiolkowski et al. (1995) also presented the values of N_G for different soil types as shown in Table 2.1.

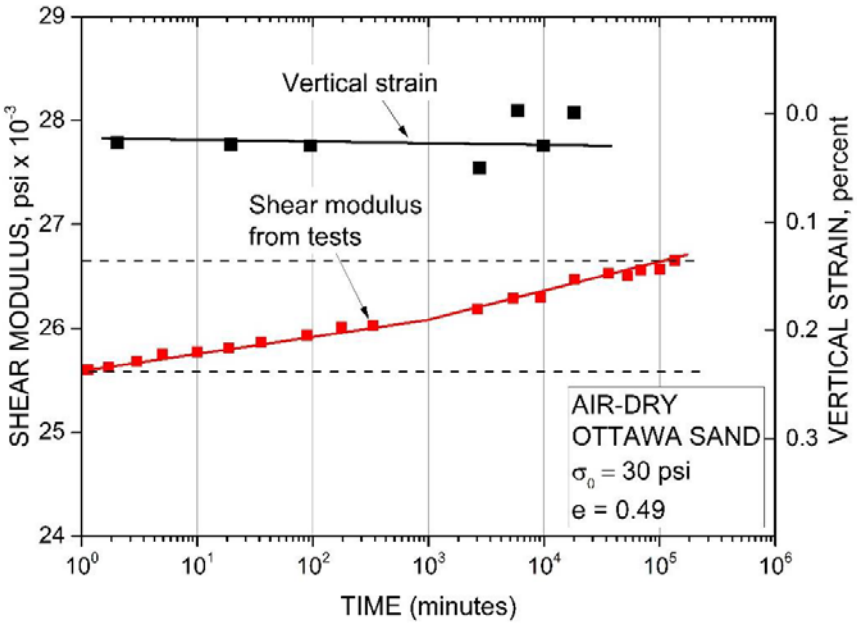

Figure 2.1. Shear modulus in air-dry Ottawa 20-30 sand (Afifi and Woods, 1971; after Wang, 2017).

Table 2.1. Shear modulus increase with time (Jamiolkowski et al., 1995).

Soil	d_{50} (mm)	PI (%)	N_G	Notes
Ticino sand	0.54	-	1.2	Predominantly silica
Hokksund sand	0.45	-	1.1	Predominantly silica
Messina sand and gravel	2.10	-	2.2 to 3.5	Predominantly silica
Messina sandy gravel	4.00	-	2.2 to 3.5	Predominantly silica
Glauconite sand	0.22	-	3.9	50% Quartz, 50% Glauconite
Quiou sand	0.71	-	5.3	Carbonatic
Kenya sand	0.13	-	12	Carbonatic
Pisa clay		23-46	13 to 19	
Avezzano silty clay		10-30	7 to 11	
Taranto clay		35-40	16	

When it comes to the elastic modulus, the secant Young's modulus is likely to be increased over time in the literature. In a study conducted by Daramola (1980), it was shown that the secant modulus of aged samples increased by approximately 50% for every log cycle of days (Fig. 2.2). He performed triaxial tests on saturated samples consolidated for 10, 30 and 152 days with 400 kPa isotropic pressure. While no measurable influence on the peak strength was found, a clear increase of stiffness was observed over time.

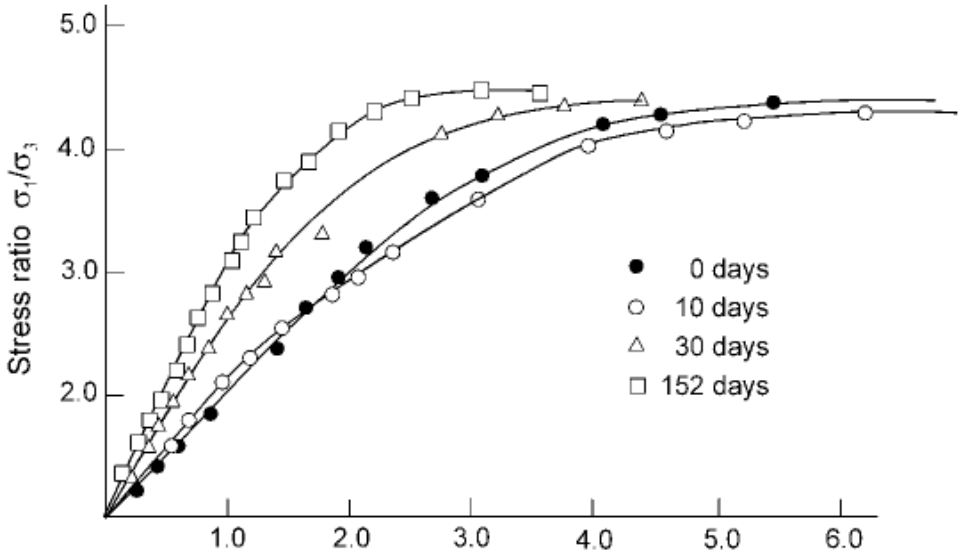

Figure 2.2. Stress-strain behavior of Ham River sand in triaxial tests of Daramola, 1980 (after Nadukuru, 2013).

In a comprehensive study of small strain Young's modulus, Howie et al. (2002) found that the stiffness shows a strong dependence on the confinement time prior to shearing and anisotropic confining stress ratio *R*. According to the results of triaxial compression tests using the very loose Fraser River sand samples, the amount of stiffness increase was proportional to the logarithm of aging time up to 10,000 minutes (1 week). During the first 1,000 minutes of aging in the tests, the stiffness of the samples with high anisotropic stress ratios increased several hundred percent, but those loaded isotropically showed only 60% increase in the stiffness. While the initial stiffness was greater for the samples with isotropic confining stress, the stiffness gain is more significant

with increasing anisotropic confining stress ratio *R*. The *G* (converted from the Young's modulus by assuming homogeneous isotropic linear elastic material) and N_G values are summarized in Table 2.2.

Table 2.2. Stiffness and dimensionless ratio of normalized shear modulus increase with time (data from Howie et al., 2002).

Stress ratio during aging (σ'_1/σ'_3)	*G* at 1 min (MPa)	*E* at 1 min (MPa)	N_G (%)	
			t_p = 1 min	t_p = 1000 min
G at 0.02% strain				
1.0	23	32	21	1
2.0	10	28	92	2
2.8	5.5	27	148	3
G at 0.1% strain				
1.0	14	18	10	< 0.5
2.0	7	11	25	1
2.8	4	9	50	1.2

Penetration resistance

To date, a number of studies have investigated the influence of sand aging on the penetration resistance in both fields and laboratory. There is a consensus among geotechnical researchers that the penetration resistance of sands increases with time as a result of sand aging. The possibly first discussions of the time-dependent increase of penetration resistance emerged during the 1960s with Denisov et al. (1963). In the study, the number of blows was counted to drive a cone (74 mm diameter and 60° cone angle) 10 cm into the soil. During the tests, the cone was driven with 60 kg hammer blows into hydraulically placed, saturated quartz river sand. The results revealed that the number of blows per 10 cm steadily rose on the average from 2.1 for 10-20 days of aging to 4.4 for 100-140 days of aging.

A significant observation and discussion on the changes in cone penetration resistance over time was presented by Mitchell and Solymar (1984). In the Jebba Dam project, Nigeria, the loose sand layer in the upper 40 m was densified with blasting and vibrocompaction to prevent liquefaction and settlements. Due to the disturbance caused by blast densification, a transient decrease of the cone penetration resistance was measured shortly after dynamic compaction. Thereafter, freshly deposited and densified sand gained a substantial increase of cone penetration resistance for several months as plotted in Fig. 2.3. This time-dependent increase in cone

penetration resistance doubled since the compaction took place. Mitchell and Solymar (1984)'s work on the penetration resistance with time is complemented by Skempton (1986)'s study of long-term Standard Penetration Tests (SPT). Skempton (1986) summarized the normalized N value, $(N_1)_{60}$, of normally consolidated fine sands with geologic aging time as presented in Table 2.3, where (D_r) is the relative density.

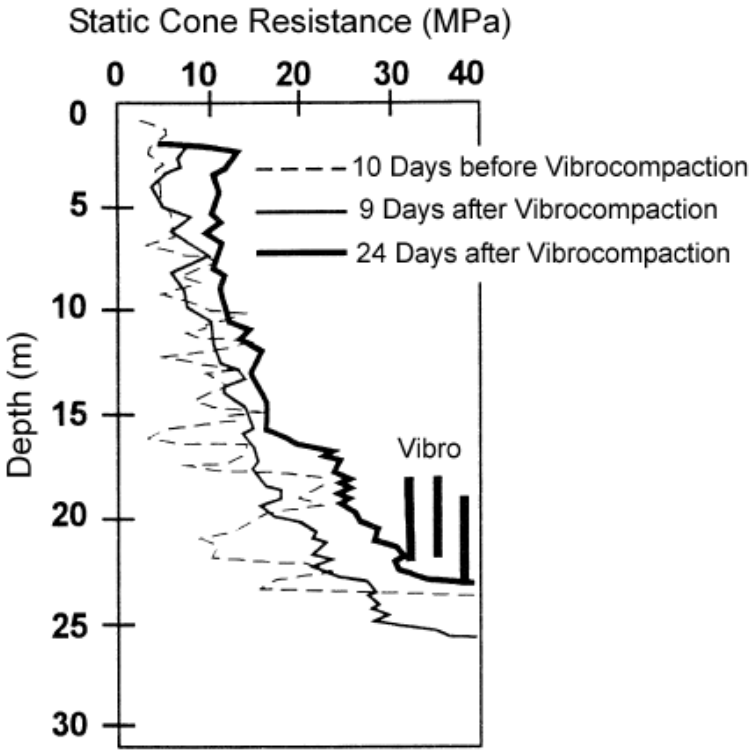

Figure 2.3. Increase in the Cone penetration test (CPT) resistance in the Jebba Dam site over time (Mitchell and Solymar, 1984).

Table 2.3. Influence of sand aging on the SPT N value (Skempton, 1986).

	Age (years)	$(N_1)_{60}/D_r^2$
Laboratory Tests	10^{-2}	35
Recent Fills	10	40
Natural Deposits	$> 10^2$	55

The laboratory study of the time-dependent penetration resistance was first carried out by Dowding and Hryciw (1986). In the minicone penetration testing of sand sample, single and two

explosive charges were fired with different time intervals, 0, 17, 25 and 50 ms, for blast densification. Due to the blasting, the initial relative density increased from 50% to the range of 60% to 78%. The increase in the cone penetration resistance caused by time effect of sand are presented in Fig. 2.4. The magnitude of the increase was much larger at positions near the charge and with larger number of explosive charges. It is interesting to note that the penetration resistance at the closest location (10 cm from the minicone) did not change compared to one of far distance or even dropped two charges were exploded.

Dumas and Beaton (1988), in the discussion paper of Mitchell (1986), reported a field observation of the time-dependent CPT resistance increase. As can be seen from Fig. 2.5, CPT resistance in 6- to 17-m thick deposit of medium- to coarse-grained sand at Sept-Iles, Quebec, site significantly increased after dynamic compaction. The magnitude of increase was up to 100% of the initial resistance at 18 days since the compaction. In comparison with the reported results by Mitchell and Solymar (1984), the rate of strength gain was more rapid, but no immediate strength reduction after compaction was measured at Sept-Iles site. The authors suspected that a very-short lived strength reduction might have happened, but it could not be measured due to a few hours of interval between finishing compaction and conducting tests. There was a clear trend of decreasing penetration strength gain with depth, indicating that generated dynamic stress by compaction attenuated with depth.

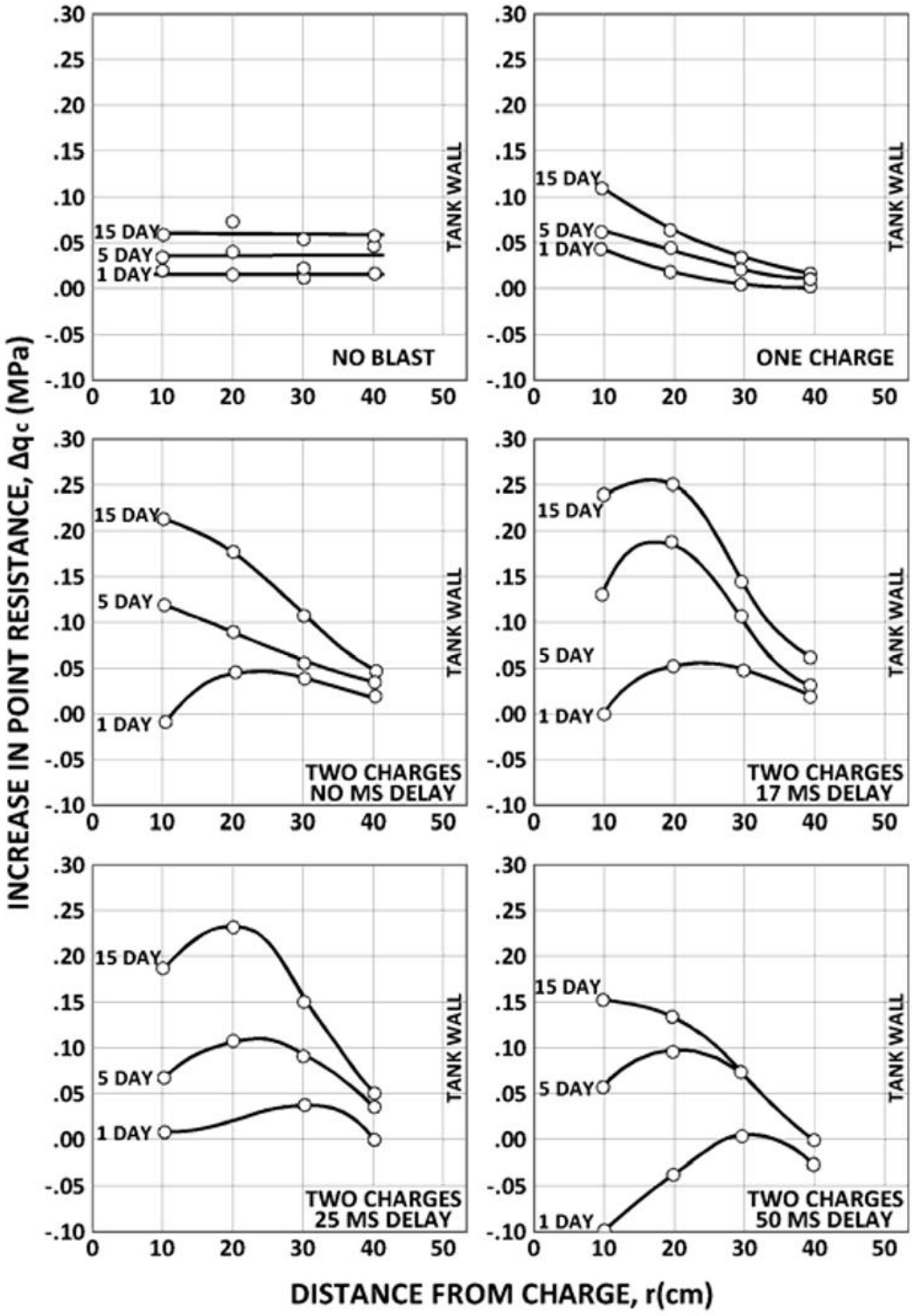

Figure 2.4. Time-dependent laboratory minicone penetration resistance densified with blasting (Dowding and Hryciw, 1986).

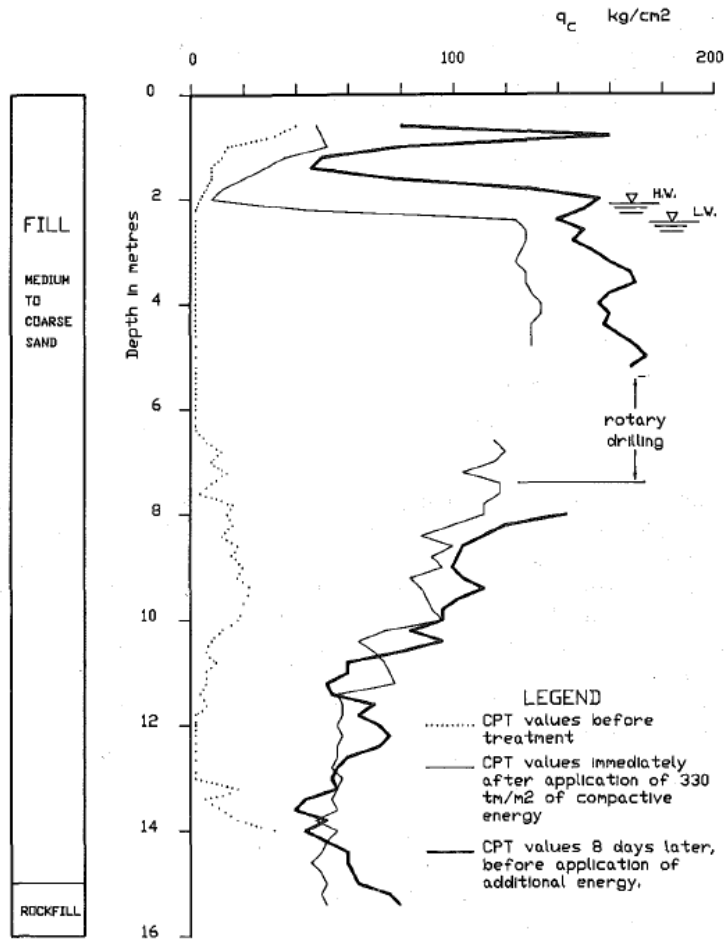

Figure 2.5. Change in field CPT resistance with time after dynamic compaction at Sept-Iles, Quebec (Dumas and Beaton, 1988).

The study by Schmertmann (1991) reported additional evidence of sand aging in penetration resistance in the field. The author measured the increased static-cone test bearing capacity after dynamic compaction in 10 m thick silty sand layer. The results were presented by the ratio of q_c to q_{c0} as a function of the time after compaction with different number of weight drops as shown in Fig. 2.6. The static cone bearing capacity rose significantly at 70 days after installation, and it also increased with the number of drops of a 33-ton weight from a height of

105 feet. The increase in bearing capacity became saturated after a rapid increase in the first two weeks.

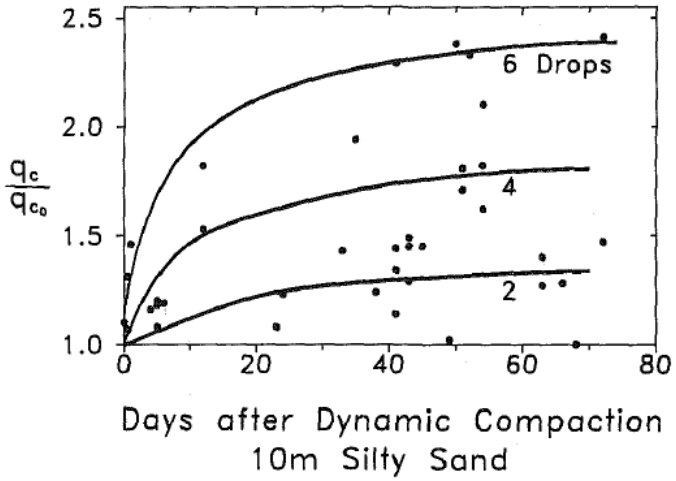

Figure 2.6. Increased static-cone test bearing capacity after dynamic compaction in 10 m thick silty sand layer (Schmertmann, 1991).

In a study conducted by Charlie et al. (1992), it was shown that three CPT measurements, tip resistance, local friction, and friction ratio, varied with time. Shortly after blasting, the measurements decreased by 62%, 30% and increased 100%. A possible explanation for the decrease in tip resistance might be the disturbance due to blasting. After 18 weeks, tip resistance increased 18% whereas local friction and friction ratio decreased 39% and 80%, respectively. The increased tip resistance is consistent with the previous CPT data (Mitchell and Solymar, 1984), but the magnitude was much smaller. The authors concluded that it may be due to the temperature affecting the time-dependent behavior of sand as the process involves chemical reaction (cementation bonds) between particles. Contrary to expectations, this study showed decreasing local friction over time, leading to the decreasing lateral stresses.

In a study investigating the effect of cementation, Joshi et al. (1995) reported that cementation associated with precipitation of salts and silica played an important role in the time-dependent increase in the penetration resistance. They performed minicone penetration tests using sands under the conditions of dry, submerged in distilled water, and sea water. Every sample showed the increased penetration resistance over time, but the magnitude was different with

environmental conditions. The amount of increased resistance ratio was the greatest in the sample submerged in sea water, whereas the smallest was in the dry conditions. The authors proposed that sand aging is affected not only by the mechanical process such as particle rearrangement, but also by the degree of cementation between sand grains.

A well-known experiment studying the influence of the precipitation of carbonate and silica on sand aging was conduced by Baxter and Mitchell (2004). The authors conducted the minicone penetration tests on Evanston beach sand and the Density sand, subjected up to 118 days of aging, with different relative densities, different temperature, and pore fluid composition. The time-dependent changes were observed in the small-strain shear modulus, electrical conductivity, and pore fluid chemistry, whereas no measurable increase in penetration resistance associated with temperature and pore fluid was observed with time. Although precipitation of carbonate and silica was observed by both mineralogical studies and chemical analyses in test samples, it only affected to small-strain stiffness and electrical conductivity, not penetration resistance. The authors pointed out that conditions in natural deposits and small-scale laboratory testing are different, suggesting that the time-dependent increase of penetration resistance caused by dissolution and precipitation might not be measured due to laboratory boundary condition and more research is needed to assess this mechanism.

There is a number of studies with different scale and time periods, which suggest the time-dependent increase in penetration resistance due to aging. For example, the full-scale blast-induced test was carried by Ashford et al. (2004). In the large-scale pilot testing, the long-term increase in penetration resistance was observed right after short-term decrease in penetration resistance, which is consistent with the literature. In terms of long-term observation, Narsilio et al. (2009) analyzed the CPT data after blast densification during the time period up to 1034 days. The results are plotted in Fig. 2.7. They stated that the noticeable increase in tip resistance was measured 2 years after blasting events, indicating that the required time for ground improvement induced by aging in very loose sand can be much longer than previously thought.

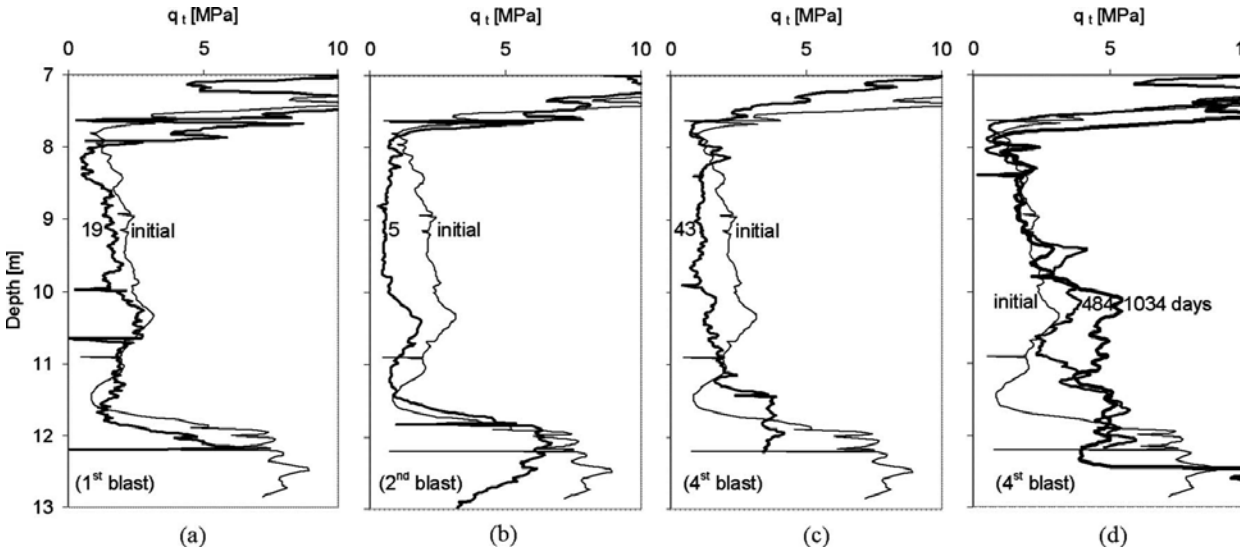

Figure 2.7. Effect of time on the CPT resistance of sand after blasting: (a) 19 days after the first blast, (b) 5 days after the second blast, (c) 43 days after the fourth blast, and (d) 484 days and 1034 days after the fourth blast (Narsilio et al., 2009).

Liquefaction resistance

Several studies have reported the relationship between sand aging and liquefaction resistance. Seed (1979) presented that the cyclic shear strength of sand fills increases with time. The normalized cyclic shear strength increase in aged sand with respect to the young deposit is plotted in Fig. 2.8. It is now well established from a variety of studies done by other researchers that the dynamic strength increases with time. Arango et al. (2000) investigated field cyclic strength of Miocene-age clayey sands from Charleston, SC, as shown by the thick line in Fig. 2.9. They plotted the overall results along with data from Seed (1979), Skempton (1986), Kulhawy and Mayne (1990), Lewis et al. (1999), Bechtel (1993, 1996), and Arango and Migues (1996), and demonstrated that there is a significant positive correlation between the age of a sand deposit and cyclic resistance ratio (CRR).

In an attempt to account for the age of sand deposit to assess liquefaction potential, Leon et al. (2006) suggested new empirical boundary curves of cyclic resistance ratio (CRR). They combined the classical in-situ soil indices (SPT, CPT, and V_s) with associated CRR values estimated from the aged sand deposits. The newly constructed curves describing the liquefaction resistance showed that old sand deposits are more resistant to liquefaction as much as 60%

comparing to the existing data (young soil deposits), indicating that the original curve leads to conservative design.

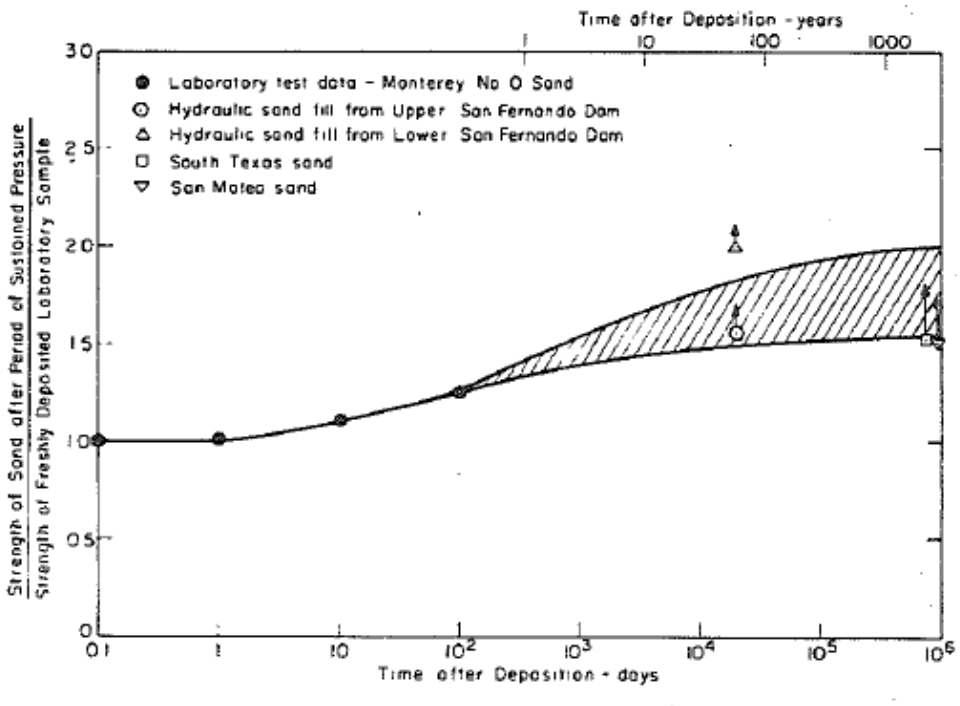

Figure 2.8. Influence of time on cyclic shear strength under confining pressure (Seed, 1979).

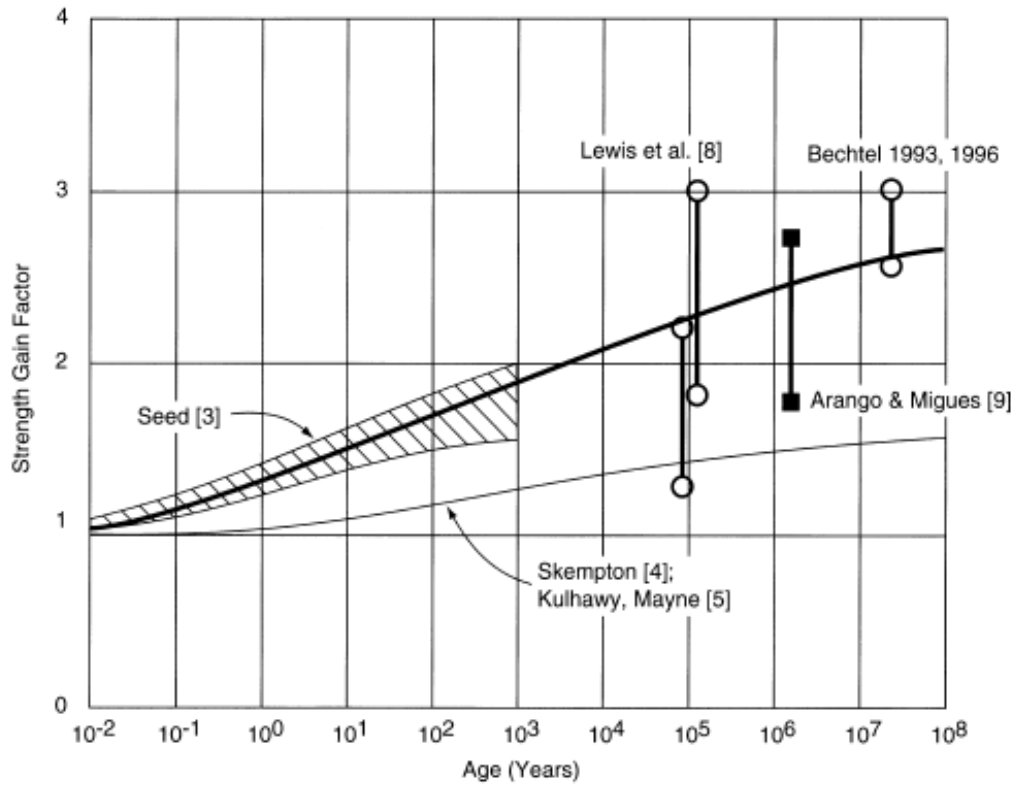

Figure 2.9. Updated cyclic shear strength with time (Arango et al., 2000).

Pile setup

The increase of the load capacity of the shaft of displacement piles in sand is one of the most significant outcomes caused by sand aging. After pore pressure dissipation, the gain in load-carrying capacity of the pile shaft significantly increases over months, and years.

Tavenas and Audy (1972) suggested that the pile formula estimating the static bearing capacity should include time effects of sand. In their study, 45 driving and load bearing tests showed that the ultimate bearing capacity increased 70% in the first two to three weeks after pile driving, and then reached the constant value as plotted in Fig. 2.10. This increase in the pile load capacity appeared to be unaffected by the pore water dissipation, as the hydraulic conductivity of sand is high enough ($k = 10^{-2}$ cm/s) to dissipate the pore pressure build up while pile driving. Considering the fact that the pore pressure is already dissipated, the authors suggested that the changes in sand structure around the pile may cause the time-dependent increase in the bearing capacity.

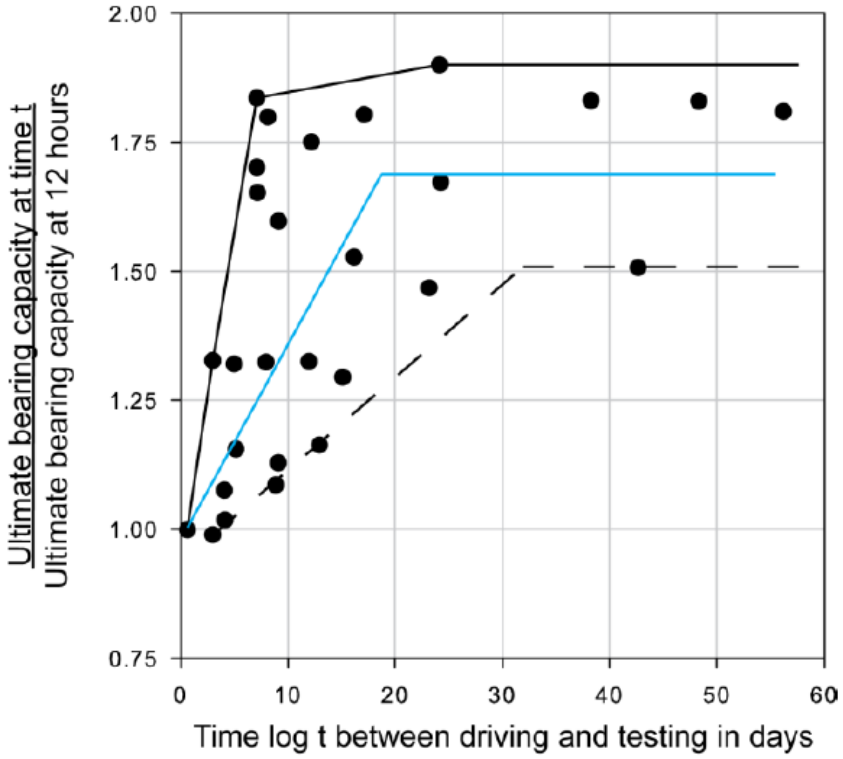

Figure 2.10. Change in ultimate bearing capacity of concrete piles with time (Tavenas and Audy, 1972).

To investigate the effects of sand aging on pile setup, Chow et al. (1998) compared the shaft resistance of open-ended pipe piles in a dense marine sand, measured in 1989 and 1994. During five years after installation, 85% increase in shaft capacity was observed. It is more interesting when they plotted their results along with data collected from the literature as shown in Fig. 2.11, where Q_{s0} is initial shaft capacity of pile and Q_s is the increased shaft capacity after time . The graph reveals that there is gradual rise in the shaft resistance over time after installation. They stated that creep results in the breakdown of circumferential arching developed around the pile, and thus leads to increase in radial stress acting on the pile shaft.

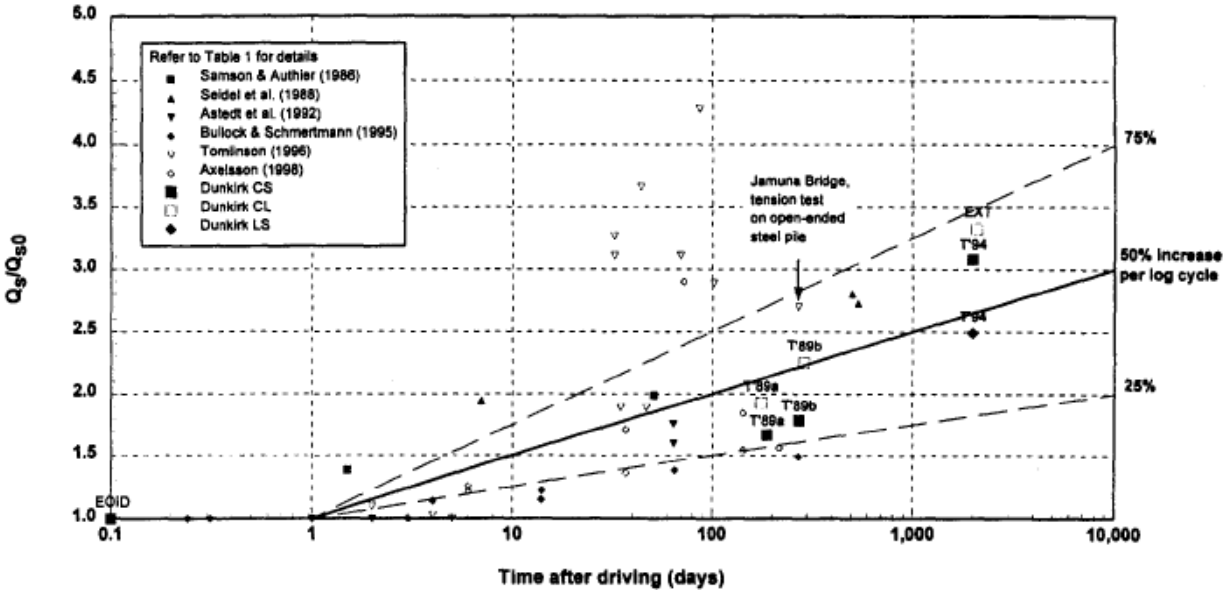

Figure 2.11. Change in shear resistance of piles over time (Chow et al., 1998).

Further observations of pile setup were offered by Axelsson (2000). He observed a linear correlation between pile capacity and the logarithm of time as presented in Fig. 2.12. The bearing capacity of square concrete piles in saturated medium dense sand increased 60% for 22 months after pile installation. While the average horizontal stress on the shaft is linearly increased over log-time which is similar to bearing capacity, vertical stress on the pile toe was almost constant during 22 months after driving. The author pointed out that time-dependent dilatant effect is the predominant cause behind of the increase in the bearing capacity.

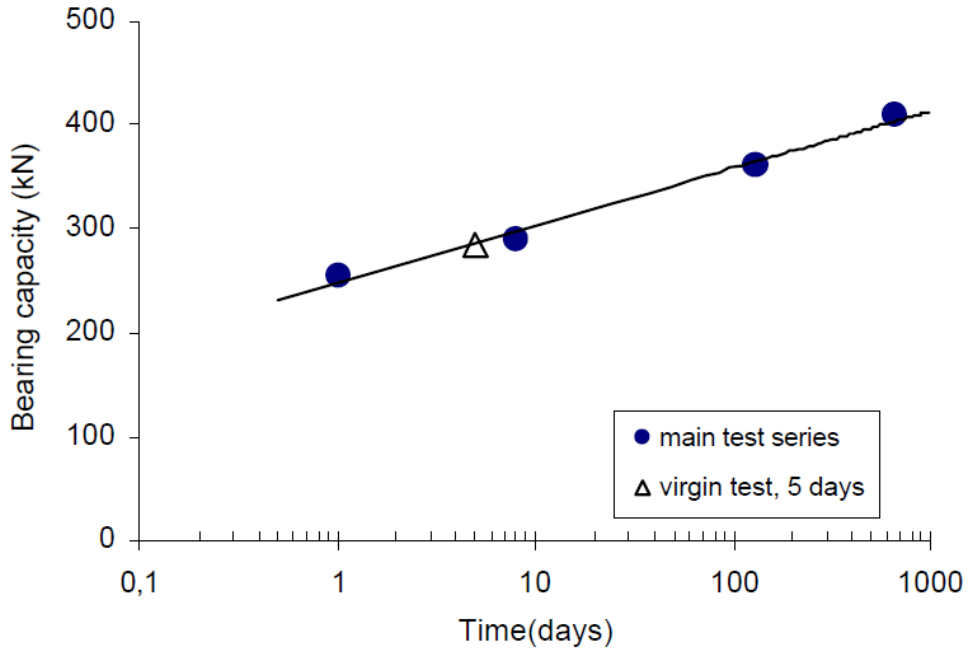

Figure 2.12. Increased bearing capacity of square concrete piles in saturated sand (Axelsson, 2000).

To better understand the mechanisms of sand aging and its effects on pile setup in granular soils, Bowman and Soga (2005) conducted a series of triaxial creep tests. The influences of particle shape, strength, relative density, and rate of loading on the creep over time were studied. In the tests, the stronger and denser sand dilates more with high stress ratio creep, producing greater pile setup. Based on the results, they proposed a new mechanism termed kinematically restrained dilation, meaning that the effective mean stress increases causing the radial stress increase under kinematic restraint condition around the pile.

Jardine et al. (2006) examined the effects of time on the capacity of piles using the tension tests on steel pipe piles performed in dense sand. They retested the dense sand and reassess the database assembled by Chow. The tension tests demonstrated: (i) there were more drastic increases in the shaft capacity than those in previously failed piles, and (ii) distinct brittle load-displacement curves were observed. This inconsistency may be due to failure both degraded capacity and modified aging process, resulting in non-monotonic shaft capacity–time plots. The shaft resistance increased more than double in eight months whereas no base resistance increase was found during that time.

A laboratory experimental study in this area is the work of Zhang and Wang (2014). They performed model pile test in a pressurized chamber filled with dry sand. They measured lateral and hoop stresses in deposit during driving and setup of piles. Although the tests does not capture the hoop stress breakdown leading to increase in shaft resistance, the clear growth in capacity after 80 hours of aging with 75 kPa of pressure was measured as plotted in Fig. 2.13. The authors suggested that the homogenized contact normal forces between soil particles also play an important role in the setup period.

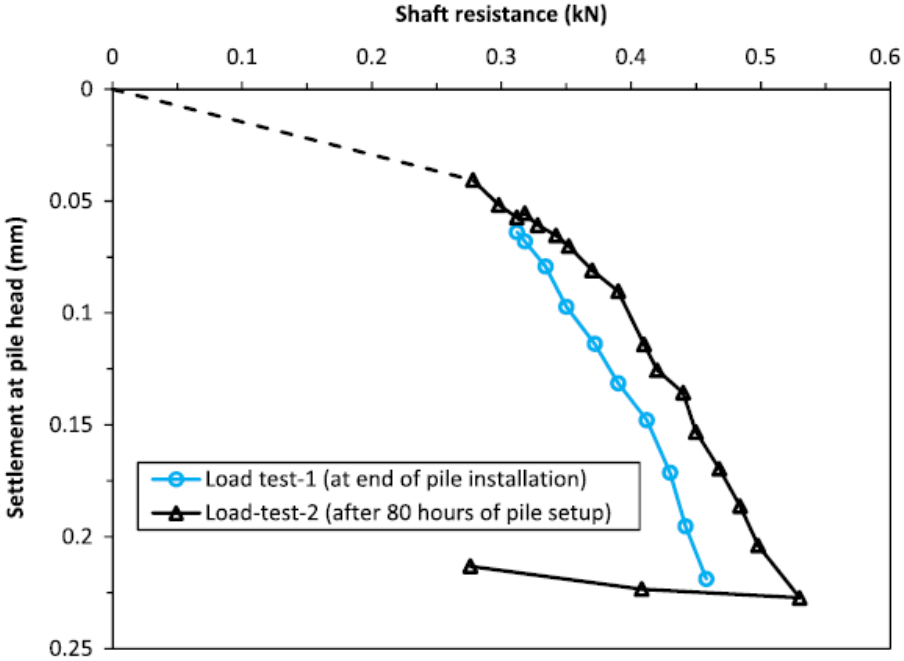

Figure 2.13. Increased shaft resistance after 80 hours of pile setup (Zhang and Wang, 2014).

2.2. Numerical simulations of time effects in sand

A large and growing body of literature has investigated the time-dependent behavior of sand by employing numerical simulations. Among a variety of numerical approaches implemented in the literature, discrete element methods (DEM) has been widely used as it is able to consider inter-particle behavior as well as granular contacts. The numerical study regarding the DEM simulation of the time-dependent behavior of soil was first carried out by Kuhn (1989). The author simulated

creep of clay based on the developed chemical reaction model at contact known as Rate Process Theory. It describes the inter-particle frictional coefficient as the linearly varied logarithm of relative velocity of contact sliding. The two-dimensional discrete element simulation showed the essential characteristics of creep in soil: (i) the creep rate decreases with time, (ii) creep rate increases with increase in the deviatoric stress, and (iii) the grain assembly approaches the creep rupture at the end. This model is useful for taking into account a correlation between aging rate and temperature that plays a key role in creep as observed in fields and laboratory testing.

To determine the effects of sand aging, Wang et al. (2008) compared DEM triaxial compressive test results of three sample groups as shown in Fig. 2.14. When the sample was aged with isotropic confinement until a target porosity was reached, the aged sample showed a noticeable increase in small-strain stiffness, early strength, and dilatancy. The aging process caused a small decrease in porosity of 1.7%. This explained the aging mechanism which causes time-dependent change in sand without decreasing the volume of voids. Interestingly, the sample prepared with identical porosity without aging (or no isotropic confinement) did not produce any increase in small-strain stiffness. The aged sample was different from the other two in the way that it showed uniform distribution of contact forces and stable force chains. The authors concluded that a key cause of sand aging is redistribution of force chains over time, rather than decreased void ratio.

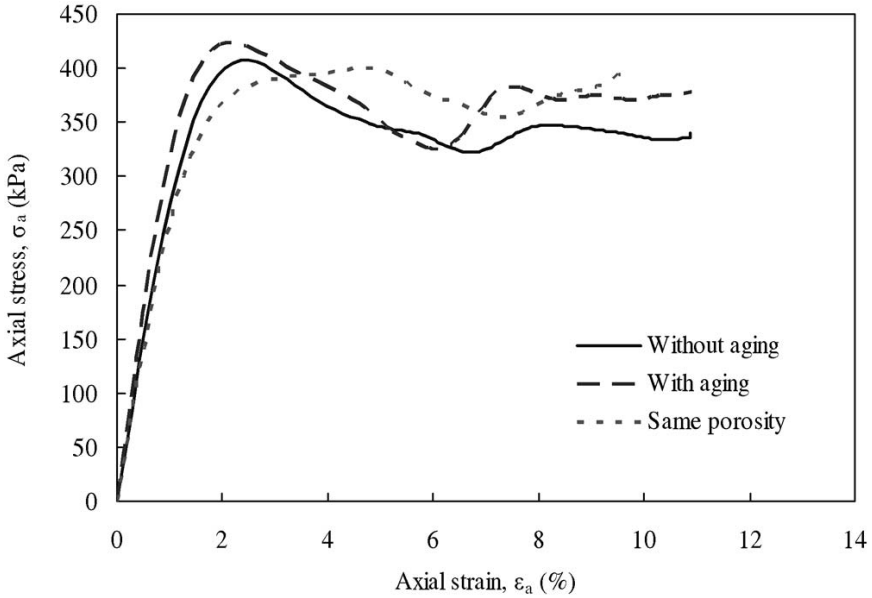

Figure 2.14. Stress-strain responses of DEM triaxial compressive tests for dense samples (Wang et al., 2008).

By adopting rate process theory suggested by Kuhn (1989), Kwok and Bolton (2010) performed DEM simulations to identify creep behavior in sand. In the DEM model, soil stiffness at contact is estimated by normal and tangential linear spring stiffness, and the coefficient of friction is calculated by the logarithm of sliding velocity. The model captured a key characteristic of soil creep that the creep rate decreases by power law over time at low shear stress. Also, both the primary and tertiary phases of creep were successfully modelled by the introduced micro-mechanism in the study. Using only one additional parameter (an increased linear rate of contact sliding coefficient with the logarithm of the sliding speed), the DEM model developed by the authors reproduced diverse time-dependent behaviors in soils; creep rate as a function of the deviatoric stress mobilization; initially linear decay of creep strain rate with time; and ultimate creep failure in triaxial simulations at high deviatoric stress ratios.

Michalowski and Nadukuru (2012) conducted 3D discrete element simulations as well as the scanning electron microscopy and energy considerations to support the static fatigue hypothesis proposed in the same paper. The DEM model including 11,000 grains with 25% clumps modelled dynamic compaction of sand showing a gradual increase in cone penetration resistance during weeks or months after the sand disturbance caused by compaction. To account for the initial liquefaction caused by dynamic compaction in the simulations, a minute reduction of particle radii was introduced, resulting in the loss of all contacts and loss of the shear resistance. When it comes to the gradual increase in the cone penetration resistance in the DEM model, the normal and shear stiffness at inter-granular contacts were increased owed to delayed fracturing of contact asperities causing convergence of grains and leading to an increased contact stiffness. This small-strain stiffness increase over time was already confirmed by earlier observations. The simulation results showed that the ratio of horizontal-to-vertical stress increased without an increase in the shear strength. The corresponding contact stiffness in the DEM model are summarized in Table 2.4. The numerical study advocated the static fatigue as the likely cause of the time-dependent effects in sands.

Table 2.4. Increase in horizontal-to-vertical stress ratio as a result of increased inter-granular contact stiffness (Michalowski and Nadukuru, 2012).

Normal contact stiffness (MN/m)	Shear contact stiffness (MN/m)	Horizontal-to-vertical stress ratio
2.0	0.8	0.339
2.2	0.88	0.365
2.4	0.96	0.378
2.6	1.04	0.391
2.8	1.12	0.399
3.0	1.2	0.413
3.2	1.28	0.424
3.4	1.36	0.433
3.6	1.44	0.442
3.8	1.52	0.451
4.0	1.6	0.459

A recent study by Zhang and Wang (2016) investigated sand aging based on the influence of microfracturing of contacts between particles. The authors assumed the frictional resistance of the contacts is reduced due to the asperity fracturing during aging. Thus, the aging process was simulated with several cycles by decreasing the mobilized frictional resistance leading to particle rearrangement. The approach satisfactorily reproduced many aspects of laboratory experiments of sand aging such as stress path – dependent deformation, stiffness and dilatancy increase during drained compression tests, shear strength and stiffness increase in undrained compression tests, and changes in void ratios and K_0 in 1D secondary compression tests over time. The simulation results of anisotropic microstructural properties showed that the stress-strain behaviors of aged samples gradually approach the original behavior of samples without aging.

2.3. Mechanism of frictional aging

Li et al. (2011) reported the main causes of frictional ageing are increased contact ‘quantity’ and ‘quality’, indicating increase in contact area attributed to asperity creep and strengthening of chemical bonding at asperity contacts, respectively. Experimental evidence in literature supports both mechanisms. First, increased true contact area due to the asperity creep is a prevailing view responsible for frictional ageing in rocks. Dieterich and Kilgore (1994) observed an increase in contact area using photomicrographs. They confirmed the strong dependence of the peak friction on the increase in contact area (Fig. 2.15). Scholz and Engelder (1976) showed that creep at the sliding surface causes a progressive increase in real area of contact with time, and this leads to an increase in friction with time of stationary contacts.

On the other hand, the formation of interfacial chemical bonds seems to be also plausible. From the *frictional force microscopy*, which is a modification of AFM, Li et al. (2011) found that the chemical bonding effects are large enough for the frictional ageing without a time-dependent creep of contact asperity. The results of single-asperity slide-hold-slide frictional experiments are shown in Fig. 2.16. Frye and Marone (2002) support the second mechanism by presenting that humidity has a significant effect on frictional healing, but not on the coefficient of sliding friction. However, it seems that the primary cause of frictional ageing is still unresolved, and further theoretical and experiment research is required to identify a mechanism that accounts for frictional ageing.

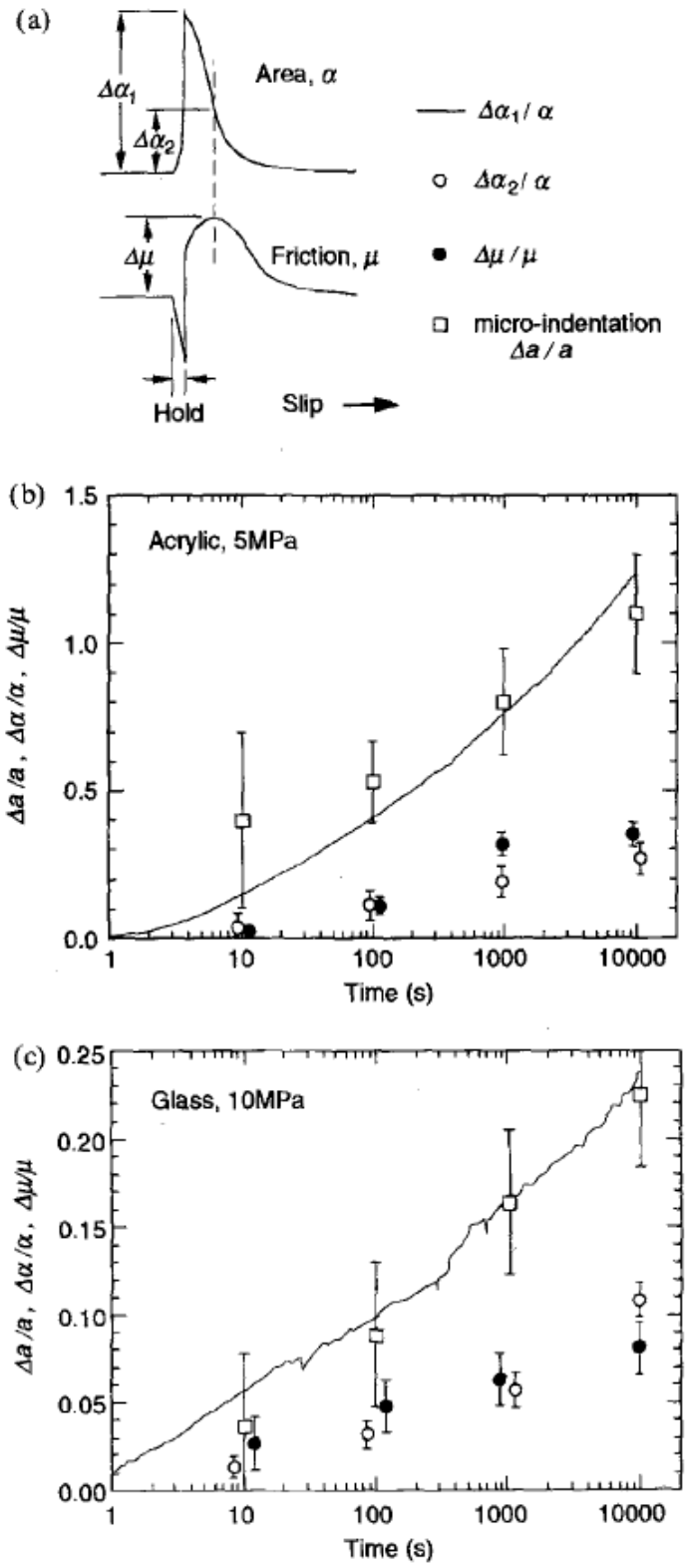

Figure 2.15. Normalized increases of micro-indentation area, contact area and peak frictional versus logarithm of time for acrylic and glass (Dieterich and Kilgore, 1994).

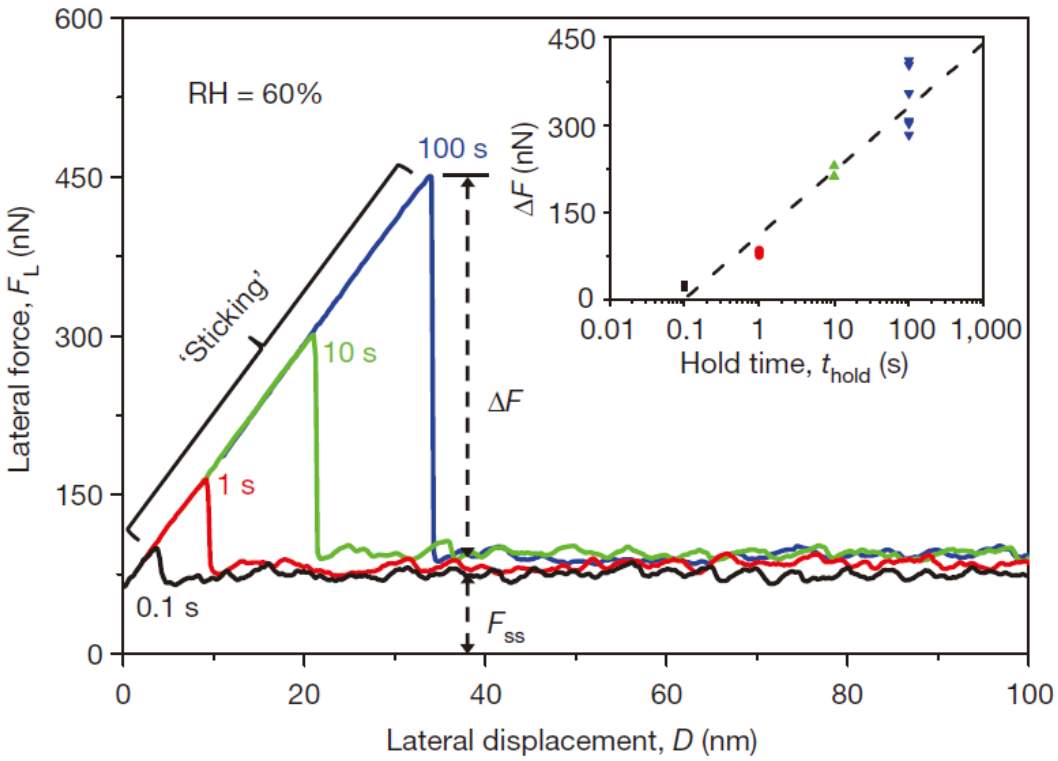

Figure 2.16. Lateral force versus nominal lateral displacement data for typical SA-SHS tests after stationary holds (Li et al., 2011).

2.4. Distinct Element Method (DEM)

Distinct element method is a numerical approach that simulates granular materials. The strength of this method is that the individual particles in a granular material and their interactions can be explicitly simulated, providing a supplemental continuum mechanics framework. The interest in the DEM has grown with recent improvements in computing power since it was first introduced by Cundall and Strack (1979) to simulate soils.

The DEM code employed in this study is the Particle Flow Code in 3 Dimensions (PFC 3D) developed by Itasca Consulting Group (Itasca Consulting Group, 2008). A single sand grain is modeled by an assembly of individual sub-particles bonded together (Wang et al., 2017, Michalowski et al., 2018b). A bonded particle model (BPM) was used to mimic micro-fracturing of sand grains in this study. This model was originally developed by Potyondy and Cundall (2004) to simulate rocks represented by a dense packing of circular or spherical sub-particles. The sub-

particles are bonded together through parallel bonds at their contact points, constituting rocks. The cracks and fractures of the rock assembly can be modelled by breaking the parallel bonds when the maximum tensile and shear stresses reach the tensile and shear strengths ($\bar{\sigma}_c$ and $\bar{\tau}_c$). The theories and formulations of BPM are well summarized in Potyondy and Cundall (2004).

Parallel-Bonded Stress Corrosion model (PSC), introduced by Potyondy (2007), is an extension of BPM to include time-dependent behaviors. In PSC, the parallel bonds between sub-particles in the DEM agglomerate are weakened by the stress-dependent corrosion rate over time, only when they are loaded above the activation stress. The weakening rate (stress corrosion rate) of parallel bonds is expressed by

$$\frac{d\overline{D}}{dt} = \begin{cases} 0, & \bar{\sigma} < \bar{\sigma}_a \\ -\beta_1 e^{\beta_2(\bar{\sigma}/\bar{\sigma}_c)}, & \bar{\sigma}_a \le \bar{\sigma} < \bar{\sigma}_c \\ -\infty, & \bar{\sigma} \ge \bar{\sigma}_c \end{cases} \tag{2.3}$$

where β_1, β_2 are model constants, the former with units of velocity and the latter dimensionless, $\bar{\sigma}_a$ is the micro-activation stress, and $\overline{D}$ is a diameter of each parallel bond. The microscopic parallel bond breakages over time give rise to the force redistribution between sub-particles, eventually leading to the macroscopic rock fracture.

2.5. Rough surface analysis and discrete asperity model (DAM)

The interpretation of scanning electron microscope (SEM) and atomic force microscope (AFM) demonstrates a myriad of asperities on the sand grain surface. When two elastic bodies interact through these multi-asperity contacts, stress concentrations are expected to occur. Many studies researched the aspects of asperities involved in contacts, developing a series of theories on rough surfaces. As a pioneering work, Archard (1957) introduced a realistic rough surface model that contact asperities are presented by a hierarchical model including small bumps on top of larger spherical bumps. The model revealed a linear relationship between the area of real contacts and the load as the bumps are added. A similar conclusion was drawn by Greenwood and Williamson (1966) who employ a Gaussian distribution for asperity heights with a constant radius of asperity.

Although the suggested models explain basic mechanics of rough surfaces in a clear manner, they have fundamental limitations in neglecting the interaction between asperities, and the theories are only valid when the area of true contact is much smaller than the nominal contact area (Persson, 2006). A local deformation at the asperity extends from itself to elsewhere through the elastic interaction in half-space. That is, the elastic coupling among small contact regions occurs, whereby the stress fields are affected. Taking into account the interaction between true asperity contacts, Discrete Asperity Method (DAM) considering a multi-asperity contact based on individual asperities can be an indispensable tool for the rough surface analysis. The concept of discrete asperity model is not originally developed here, but the model is improved by coupling normal and lateral components so that it is able to consider the critical aspect of frictional ageing.

Using DAM simulations with a different nominal contact area, Li et al. (2011) demonstrated that a frictional ageing by strengthening bonding between asperities is a scale-dependent phenomenon. Comparing to the lateral force microscopy of single asperity slide-hold-slide frictional experiments, the DAM simulation of large nominal contact (with many contact asperities) produces smaller increase in frictional strength obtained by ageing effect. This significant decrease in ageing effect for larger contacts is consistent with observations from macroscopic rocks. On the other hand, the simulation with a small nominal contact area (small number of asperities) associated with microscopic frictional ageing is similar to that measured for individual asperities in tests, indicating a much larger ageing effect at the small-length scale. Using the simplified mechanics model with lateral force and displacement only, the results explain a general phenomenon well: smaller nominal contacts generally have a much larger ageing effect than larger nominal contacts. By controlling the number of asperities in the nominal contact region, they successfully applied DAM to multi-scale simulations.

Recently, Li et al. (2018) studied a normal contact stiffness of regularly patterned multi-asperity interfaces using DAM formulated by normal force and displacement. According to their research, the elastic interaction among contacts mainly determines mechanical behaviors of rough surface. The DAM used in that paper considers asperity as a rigid pillar pushing the elastic half-space below. Indentation experiments for characterizing the contact between rigid body pillars and a flat polydimethylsiloxane (PDMS) validated the discrete asperity model, and showed remarkable consistency with test results. Despite of a simple 1-D displacement load in the model, DAM captured the essential behaviors of rough contacts very well.

Chapter 3

Research Objectives

This research investigates the time-dependent behavior of geomaterials. In sands, the *static fatigue hypothesis* is adopted to account for sand aging. This hypothesis suggests that sand aging is strongly dependent on the static fatigue process that occurs on the contacts between sand grains. Static fatigue manifests itself as delayed fracturing of micro-morphological features on grain surfaces at contacts (asperities, crystalline fragments, and mineral debris). This hypothesis was first suggested in Michalowski and Nadukuru (2012), but the substantial evidence supporting the hypothesis is yet to be collected. Based on the literature, the following research objectives have been formulated:

1. identifying visual and quantitative evidence for time dependent fracturing (or stress corrosion cracking) at sand contacts,
2. exploring the consequences of static fatigue on grain contacts and of the time-dependent stress-corrosion cracking on long-term grain split through conducting discrete numerical simulations, and
3. investigating the influence of contact maturing on the frictional contact behaviors.

Chapter 4

Observation of Contacts and the Contact Maturing Process

4.1. Introduction

Surfaces of sand grains are characterized by considerable roughness at the microscopic scale. Such surfaces do not make contact everywhere when two grains are squeezed together; instead, the peaks (asperities) on the two surfaces come into contact. As a result, a true contact area is small compared to the nominal contact area, causing a stress concentration followed by the fracturing of contact asperities. Therefore, accounting for the roughness is of utmost importance to the description of contact behavior in sand.

When it comes to the contact area, Hertz's elastic contact theory (Hertz, 1882) suggests that the contact area between smooth surfaces increases with the squeezing force to the two-third power, *i.e.*, $P^{2/3}$. The experiment of rough surface, however, shows an inconsistency of contact area being proportional to P. Archard's simple mechanical model (Archard, 1957) of asperities is described by a hierarchical model including small bumps on top of larger spherical bumps, and it assures the true contact area to be proportional to the normal load P. This is consistent with the

Coulomb's friction law based on the linear relationship between frictional force and normal load (Persson, 2013).

The surface roughness of sand plays an important role in the time-dependent behavior as presented by Michalowski et al. (2018a). They stated that, from the static fatigue hypothesis, the number of contact points on the nominal contact area increases over time under sustained loading, leading to stiffer and firmer grain contacts. In the experimental study, a grain deflection over time, referred to as *convergence*, is heavily dependent on the initial roughness of sand grains. The more rough the grain surface, the larger the convergence over time. The authors stated that the time-dependent fracturing of contact asperities is more intense in the rough surface due to high stress concentration, causing a large amount of contact maturing.

This chapter addresses characterization of roughness of sand grain surfaces and the influence of roughness parameters on the contact maturing process in sand. In the following section, a brief description of the Power Spectral Density (PSD) is given, which will be used to analyze surface roughness. A rich texture of sand grain surfaces is confirmed by observations using Atomic Force Microscope (AFM). The typical surface roughness parameters are examined and statistical analyses are performed. Three grain testing is used to quantitatively characterize changes of surface morphological features before and after contact maturing. Finally, the results of the grain-scale laboratory experiment are presented to test time-dependent behavior of sands subjected to sustained loading.

4.2. Power Spectral Density

Many physical properties such as stiffness, contact area, adhesion, friction, electrical, and thermal conductivity are dependent on the true contact area that is strongly dependent on surface roughness. The Power Spectral Density, easily calculated from the surface elevation profiles obtained from AFM scans or optical methods, is capable of estimating the contact area and these properties. The PSD presents the spatial surface profiles as a function of the spatial frequency from knowledge of the Fast Fourier Transform (FFT). The PSD takes the amplitudes of the FFT, multiplies its complex conjugates to get a magnitude squared, and normalizes by its frequency bin width. The normalization enables the PSD to be independent of sample size. As its name implies, the PSD

contains the power, instead of phase over a given range of wavevectors. In summary, the PSD decomposes a surface profiles into contributions of different wavelength components, and identifies spatial frequencies embedded in the surface. A short description follows.

Given that a continuous function of surface profiles, $h(x, y)$, is available over the area with lateral lengths L_x and L_y ($L_xL_y = A$), the forward and inverse Fourier transform can be found as

$$\tilde{h}_{q_x,q_y} = \int_A h(x,y)e^{-i(q_x x+q_y y)}dxdy \tag{4.1}$$

$$h(x,y) = \frac{1}{L_x L_y}\sum_{q_x,q_y} \tilde{h}_{q_x,q_y} e^{i(q_x x+q_y y)} \tag{4.2}$$

where q_x and q_y are wavevectors (spatial frequencies) running from -∞ to ∞. As function $h(x, y)$ is typically a discrete rather than continuous function, Eq. (4.1) is converted into the forward discrete Fourier transforms calculated by

$$\tilde{h}_{q_x,q_y} = l_x l_y \sum_{x,y} h_{x,y} e^{-i(q_x x+q_y y)} \tag{4.3}$$

where l_x and l_y are the grid sizes (resolution) along with x- and y-directions, and $h_{x,y}$ is the discrete height profiles on 2D surface. They are computed by $l_x = L_x / m$ and $l_y = L_y / n$ when the number of points in the x- and y-directions are m and n. In Eq. (4.3), the spatial frequencies are varied from 0 to $2\pi(m - 1)/L_x$, or $2\pi(n - 1)/L_y$ rather than -∞ to ∞. The rigorous mathematical definition of the PSD is found as (Jacobs et al., 2017, Nayak, 1971, Persson et al., 2005)

$$C^{2D}_{q_x,q_y} = A^{-1}\left|\tilde{h}_{q_x,q_y}\right|^2 \tag{4.4}$$

By virtue of Eq. (4.4), it takes only amplitude by removing all phases. While the definition of the PSD is unique, there is a mathematical variation in its calculation and interpretation. Persson et al. (2005) employed a PSD normalized by $(2\pi)^2$ as follows

$$C_{q_x,q_y}^{2D} = A^{-1}\left|\tilde{h}_{q_x,q_y}\right|^2 / 4\pi^2 \tag{4.5}$$

When a surface is considered as isotropic where any power spectrum is independent on the radial direction, an expression C_{q_x,q_y}^{2D} becomes C_q, which is a function of q with $q = \sqrt{q_x^2 + q_y^2}$. The zeroth, second, and fourth spectral moments correspond to the roughness parameters, the root-mean-square (RMS) height h_{rms} , the RMS slope h'_{rms} , and the RMS curvature h''_{rms} . They are determined by the PSD as following (Jacobs et al., 2017)

$$h_{rms}^2 = avg\left|h\right|^2 = \frac{1}{A}\int_A h^2(x,y)dxdy = \frac{1}{A^2}\sum_{q_x,q_y}\left|\tilde{h}_{q_x,q_y}\right|^2 = \frac{1}{A}\sum_{q_x,q_y} C_{q_x,q_y}^{2D} \tag{4.6}$$

$$\left(h'_{rms}\right)^2 = avg\left|\nabla h\right|^2 = \frac{1}{A}\int_A\left|\nabla h(x,y)\right|^2 dxdy = \frac{1}{A^2}\sum_{q_x,q_y}\left(q_x^2+q_y^2\right)\left|\tilde{h}_{q_x,q_y}\right|^2 = \frac{1}{A}\sum_{q_x,q_y} q^2 C_{q_x,q_y}^{2D} \tag{4.7}$$

$$\left(h''_{rms}\right)^2 = \frac{1}{4}avg\left|\nabla^2 h\right|^2 = \frac{1}{4A}\int_A\left|\nabla^2 h(x,y)\right|^2 dxdy = \frac{1}{4A^2}\sum_{q_x,q_y}\left(q_x^2+q_y^2\right)^2\left|\tilde{h}_{q_x,q_y}\right|^2 = \frac{1}{4A}\sum_{q_x,q_y} q^4 C_{q_x,q_y}^{2D} \tag{4.8}$$

It has been found that a wide range of surfaces present fractal characteristics, referred to as self-affine or self-similar. Fractal surface reveals that a realistic rough surface is covered with small bumps on top of larger bumps, through the spatial dimension (Archard, 1957). As a result, magnified surfaces with different scales in the fractal surface have the same statistical characteristics. The PSD curve of a self-affine surface shows a power function of the spatial frequency, $C = q^{-2-2H}$ where H is the Hurst exponent. A scaling factor, recovering same roughness with different scale, is defined by the Hurst exponent as λ^H; $\lambda^H h(x/\lambda, y/\lambda)$ and looks like $h(x, y)$. It varies from 0 to 1 and gives the fractional dimension D_f ($H = 3 - D_f$). Fig. 4.1 represents an idealized PSD curve of the self-affine surface; it defines the ranges between lower and upper limits of the wavevectors (q_l and q_s). For wavevectors lower than q_r, the PSD has a constant value, indicating the power becomes zero ($H = 0$ of the PSD curve of a self-affine surface). This is known as 'roll-off' wavevector, $q_l < q_r < q_s$. Thus, the idealized power spectral density function of fractal surfaces can be determined by

$$C(q) = C_0 \begin{cases} 0 & \text{if } q < q_l \\ q_r^{-2-2H} = const. & \text{if } q_l \le q < q_r \\ q^{-2-2H} & \text{if } q_r \le q < q_s \\ 0 & \text{if } q \ge q_s \end{cases} \tag{4.9}$$

where C_0 is a constant. From Parseval's theorem (Eq. (4.6)), the RMS roughness is the same as the shaded region in Fig. 4.1 of the PSD curve

$$\mathrm{RMS}^2 = \frac{1}{A}\sum_{1}^{n}\sum_{1}^{m}\left|C(q)\right| \tag{4.10}$$

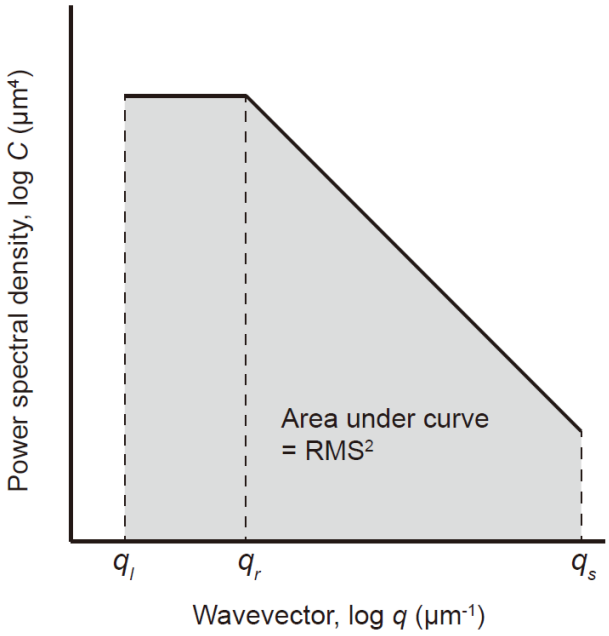

Figure 4.1. Idealized power spectral density (PSD) curve of self-affine surface.

4.3. Surface observation and roughness characterization

To characterize a rich texture of grain surfaces, elevation profiles of the surface were measured by the Atomic Force Microscopy (AFM). The AFM, a type of high-resolution scanning probe

microscopy, is designed to gather geometric information by touching (feeling) the surface with a sharp scanning probe. The instrument utilized in the study was Veeco Dimension Icon® by Bruker. Among a number of modes available in the device, contact mode was adopted. The contact mode is suitable for hard solid surfaces, as a scanning probe is in physical contact with the sample and dragged on the sample surface. More details of the device can be found in Veeco Instruments (2010).

The AFM measurements of sand grain surfaces were obtained on 60 μm × 60 μm scanning areas. The number of discrete points on the area is 512 by 512 (total 262,144 points), meaning that the resolution (grid size) is 60 / 512 = 0.117 μm. The total of 16 Ottawa 20-30 Sand grains (grain size between 0.6 – 0.84 mm) were characterized.

Fig. 4.2 illustrates images of sand grain surfaces. These images are seen as continuum surfaces with hills and valleys, yet they are actually assemblies of discrete 512 × 512 pixels. From the true surface images of sand grains in Fig. 4.2, it is apparent that sand grain surface has a rich texture. It is expected that delayed fracturing of these micro-morphological features caused the contacts to evolve over time (contact maturing). A strong relationship between surface texture and the time-dependent behavior of sand has been reported in the literature (Michalowski et al., 2018a). Characterizing the roughness is challenging, as the sand grain surfaces appear to be random (Fig. 4.2). The statistical approach is adopted to account for the surface roughness.

Before statistical analysis, a plane fitting was applied for correcting tilt and bow in the AFM measurements. The visual representation of the plane fitting is shown in Fig. 4.3. Because shapes of sand grains are generally round, the scanned area by the AFM may not be horizontally aligned. Instead, it can be tilted as plotted in Fig. 4.3(a). Statistical analyses of these height profiles obtained from the tilted scanning area produce different values from those computed by the scanned surface oriented horizontally. For example, a root mean square value, which is the arithmetic mean of the squares (see Eq. (4.14) for mathematical definition), of the tilted surface is 2016 nm (Fig. 4.3(a)), but it decreases to 28.6 nm after correcting the tilt with plane fitting function (Fig. 4.3(b)). The plane fitting on both x and y directions is recommended by the most standards, before calculating statistical values.

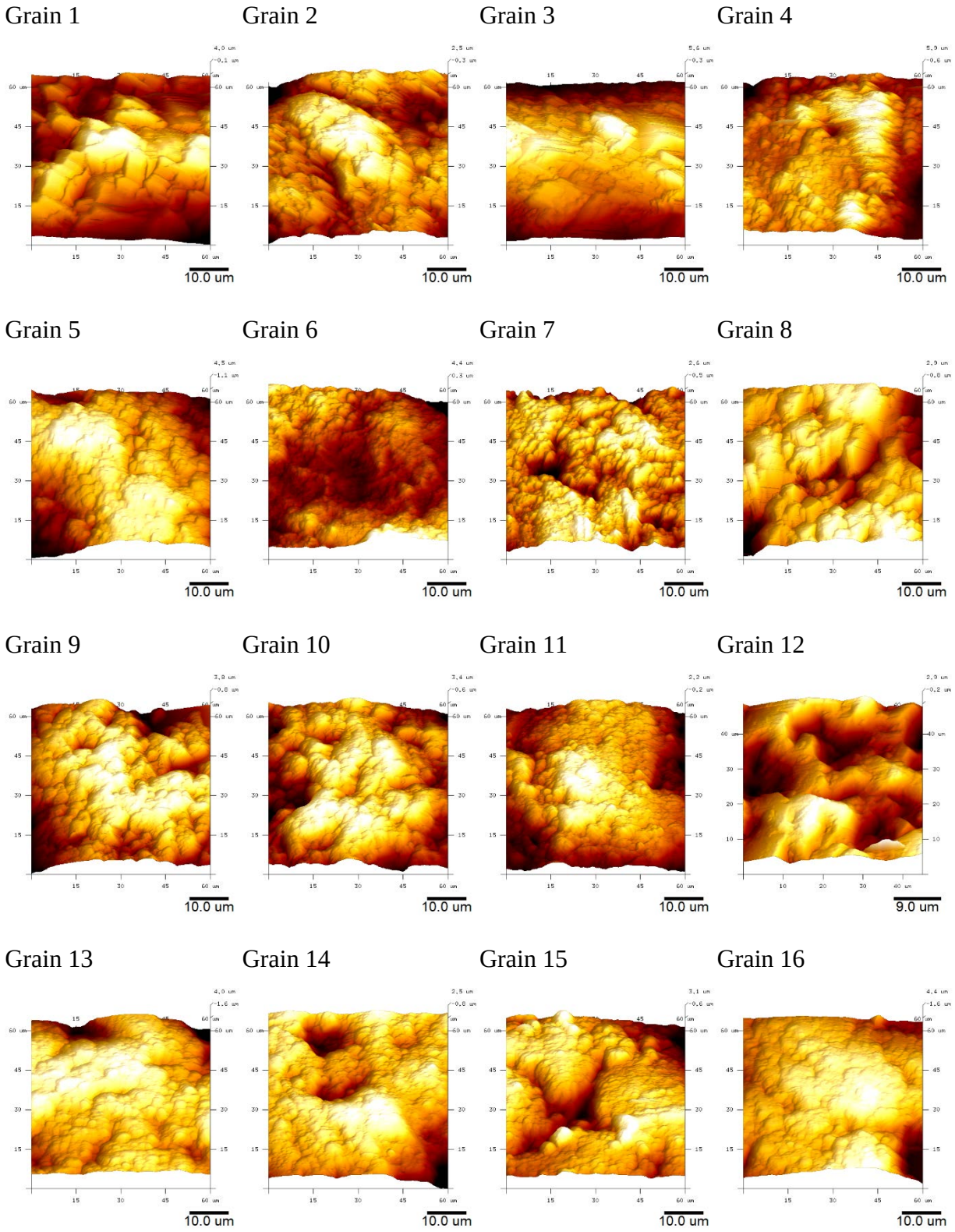

Figure 4.2. Images of sand grain surfaces by AFM measurements.

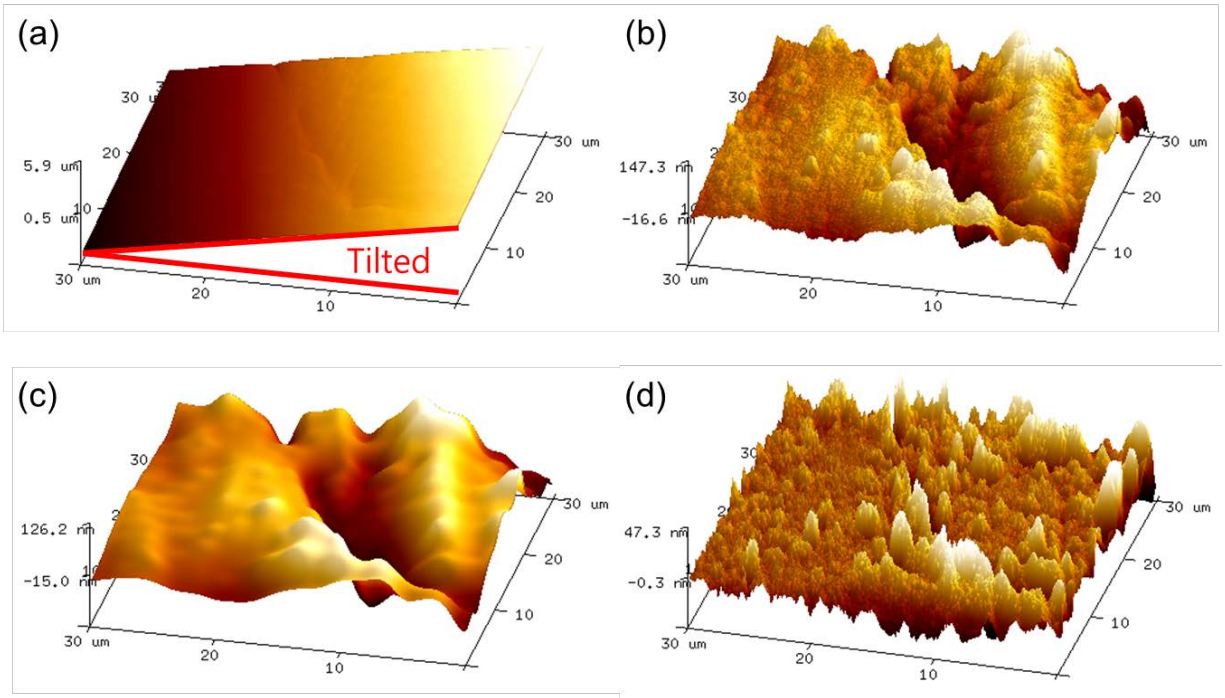

Figure 4.3. Correction of raw surface profiles: (a) tilted image, (b) plane fitted surface, (c) surface waviness, and (d) highpass filtered image of the grain surface showing microscopic roughness.

In this study, the plane fitting was carried out using a *Plane Fit* function in NanoScope Analysis 1.5 software (Veeco Instruments, 2004). The function removes tilt and bow in raw data. It fits data by a polynomial of the given order and subtracts an original image from this polynomial profile. The *x* and *y* polynomial orders can be generally set separately, i.e. the fitted polynomial is

$$z = \sum_{j=0}^{p} \sum_{k=0}^{q} a_{j,k} x^j y^k \tag{4.11}$$

where $a_{j,k}$ is a constant associated with the best plane fit for the images, p and q are the selected horizontal and vertical polynomial degrees, respectively. A first-order plane fit was adopted in the study, meaning that a fitted polynomial is $z = a_{0,0} + a_{1,0}x + a_{0,1}y + a_{1,1}xy$. The plane fitting is different from a *highpass* filter, frequently used in surface analysis. This filter deletes longer wavelength features, whereas the *lowpass* filter allows them. As a result, the highpass filter allows identification of microscopic roughness by removing waviness on surface, but the highpass-filtered surface is susceptible to noise such as spikes and fuzz. In many cases of surface analysis,

the microscopic roughness of surface is of importance, and thus longer wavelengths are filtered out by the highpass filter. Fig. 4.3(d) presents a surface subjected to the highpass filter removing longer wavelengths (waviness, Fig. 4.3(c)) from the original surface (4.3(b)). The filtered surface in Fig. 4.3(d) has only microscopic roughness, and it will behave differently from the original surface. The highpass filter operation was not applied in this study, because the waviness presented as hills and valleys plays an important role in force transmission and contact maturing processes.

Based on the AFM measurements subjected to 1st order plane fitting, statistical analyses characterizing surface roughness were performed. The histograms of the 16 grain surfaces are plotted in Fig. 4.4, by stacking all histograms whose mean values of heights were set to be zero. The height profiles are slightly skewed to the right-hand side. It shows that the elevation distributions of sand grain surfaces appear to be the Gaussian distribution. The average standard deviation of the 16 grain surfaces computed from the Gaussian distribution best-fit (red-line in the figure) is 1.256 μm.

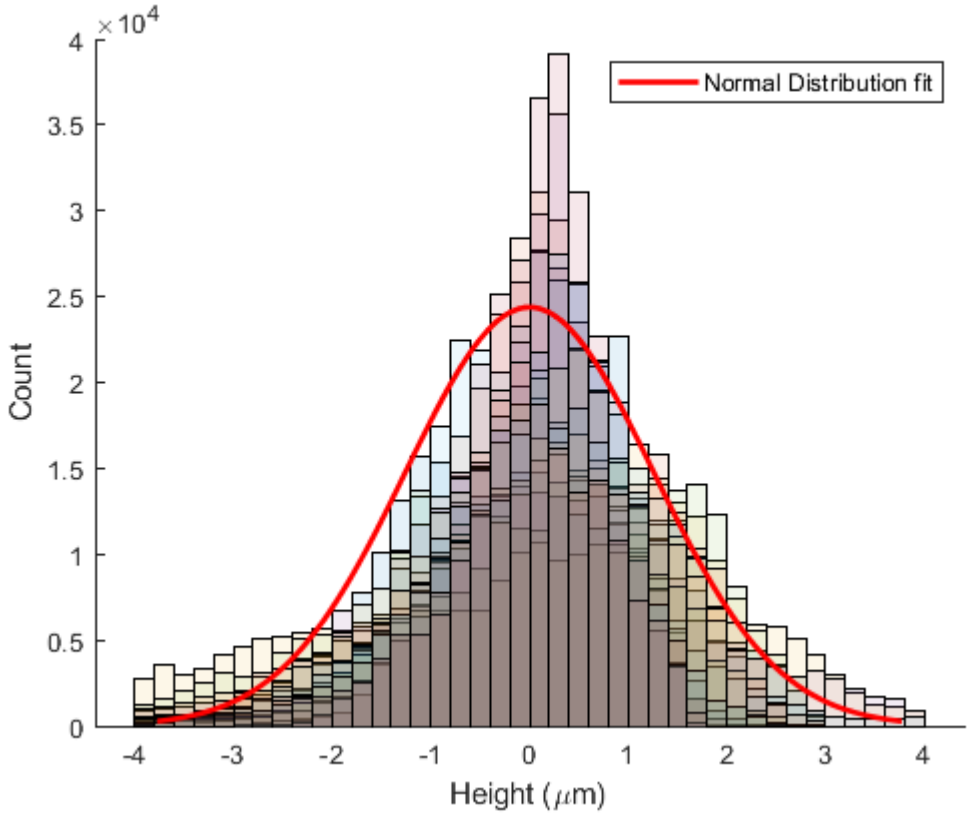

Figure 4.4. Histogram for 16 sand grain surfaces (average histogram marked by red line).

Table 4.1 summarizes the commonly used roughness parameters, calculated for the 16 grain surfaces depicted in Fig. 4.1.

Table 4.1. Summary of sand grain roughness parameters.

Sample no.	Surface area (μm^2)	Surface area / Projected area*(%)	R_q (nm)	R_a (nm)	R_{max} (nm)	Skewness, S_{sk} (nm)	Kurtosis, S_{ku} (nm)
1	3979	10.50	1228	1020	6799	0.036	2.43
2	3882	7.83	766	595	5242	-0.455	3.88
3	4060	12.80	1917	1589	9925	-0.299	2.32
4	4701	30.60	1741	1313	11769	-0.324	3.83
5	3940	9.45	1681	1337	9380	-0.804	3.35
6	3899	8.31	1083	853	8333	0.361	3.58
7	4139	15.00	814	625	6888	-0.924	5.03
8	3898	8.29	1003	747	7452	-1.200	5.42
9	4151	15.30	1401	1126	7820	-0.636	3.01
10	4075	13.20	1224	1000	7200	-0.510	2.77
11	3727	3.54	756	612	4657	-0.384	2.65
12	3928	9.12	1036	823	6689	-0.534	3.63
13	3920	8.89	1375	1027	8573	-1.270	5.66
14	3766	4.62	835	600	5545	-1.290	5.80
15	3900	8.33	974	764	7068	-0.763	3.78
16	3904	8.44	1416	1033	8763	-1.290	6.05

* Projected area: 3600 μm^2 (= 60 μm × 60 μm)

The surface roughness can be firstly characterized using the most commonly used parameter, *Average Surface Roughness* (S_a).

$$S_a = \frac{1}{mn}\sum_{i=1}^{m}\sum_{j=1}^{n}\left|z_{ij} - \mu\right| \tag{4.12}$$

where $z_{i,j}$ is the height profile at point (i, j), and μ is the mean elevation of the profiles calculated by

$$\mu = \frac{1}{mn}\sum_{i=1}^{m}\sum_{j=1}^{n} z_{ij} \tag{4.13}$$

The average surface roughness is also known as the center-line average. It is easy to define and measure, but it does not consider surface deviations. Using the S_a value alone for surface analysis leads to a significant misrepresentation, because it just indicates how far the heights are from the mean.

Root Mean Square (S_q, RMS), one of the most important parameters, is defined as the arithmetic mean of the squares.

$$S_q = \sqrt{\frac{1}{mn}\sum_{i=1}^{m}\sum_{j=1}^{n}\left(z_{ij}-\mu\right)^2} \tag{4.14}$$

The surface roughness is always characterized by the RMS value, due to convenience. The RMS is more sensitive to the surface deviations compared to the average surface roughness (S_a). The interpretation of the RMS requires caution, as different surfaces with the same Root Mean Square (S_q) and Average Surface Roughness (S_a) values can present very different surface morphology, as exemplified by Bhushan (2000), Fig. 4.5.

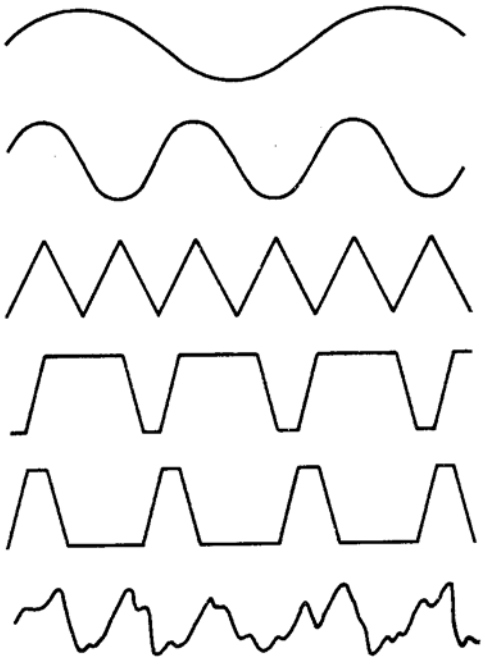

Figure 4.5. Different surface profiles with identical RMS values, redrawn from Bhushan (2000).

Surface Skewness (S_{sk}) represents the degree of symmetry of the elevation distribution function about the mean defined as

$$S_{sk} = \frac{1}{mnS_q^3} \sum_{i=1}^{m} \sum_{j=1}^{n} \left(z_{ij} - \mu \right)^3 \tag{4.15}$$

Zero skewness indicates a symmetric distribution of profiles such as the Gaussian distribution. If the skewness is positive, it is skewed to the left, smaller heights are dominant, as presented in Fig. 4.6(a). In this case, the height profile shows sharp peaks and wider valleys. The negative value of skewness suggests that the profile distribution is skewed to right, showing the deep and narrow scratches on the surface.

Surface Kurtosis (S_{ku}) describes the sharpness of the height distribution function as plotted in Fig. 4.6(b). It measures pointedness and bluntness of surface roughness, and it is determined as

$$S_{ku} = \frac{1}{mnS_q^4} \sum_{i=1}^{m} \sum_{j=1}^{n} \left(z_{ij} - \mu \right)^4 \tag{4.16}$$

When $S_{ku} > 3$, the corresponding profile distribution presents many peaks and valleys (Leptokurtic). On the other hand, the distribution with $S_{ku} < 3$ (Platykurtic) has a few peaks and valleys.

In terms of moments of the probability density function of profiles, $p(z)$, the abovementioned parameters: Average Surface Roughness, Root Mean Square, Surface Skewness and Surface Kurtosis, are related to the first, second, third, and fourth moment of the probability density function, as following

$$S_a = \int_{-\infty}^{\infty} z p(z) dz \tag{4.17}$$

$$S_q = \int_{-\infty}^{\infty} z^2 p(z) dz \tag{4.18}$$

$$S_{sk} = \frac{1}{S_q^3} \int_{-\infty}^{\infty} z^3 p(z) dz \tag{4.19}$$

$$S_{sk} = \frac{1}{S_q^4} \int_{-\infty}^{\infty} z^4 p(z) dz \tag{4.20}$$

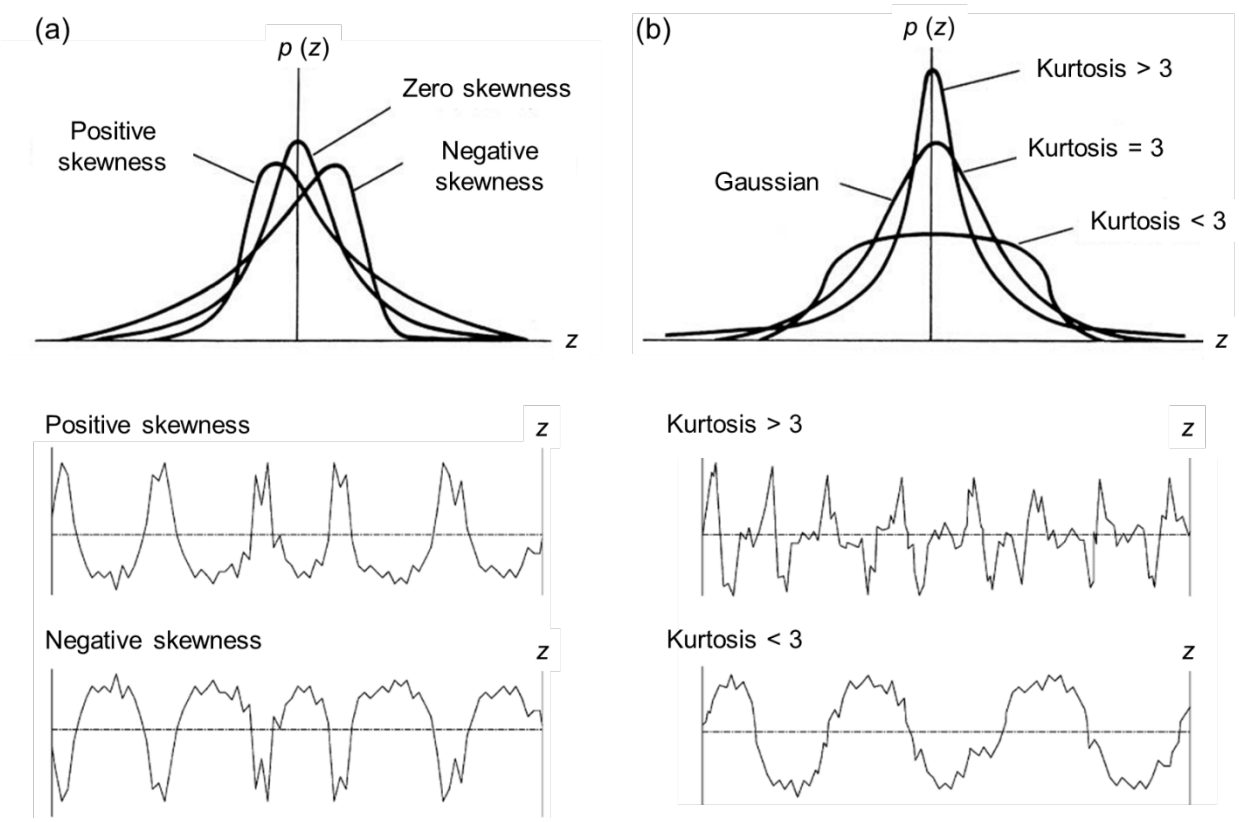

Figure 4.6. Probability density function with: (a) different skewness, and (b) zero skewness with different kurtosis, redrawn from Bhushan (2000) and Gadelmawla et al. (2002).

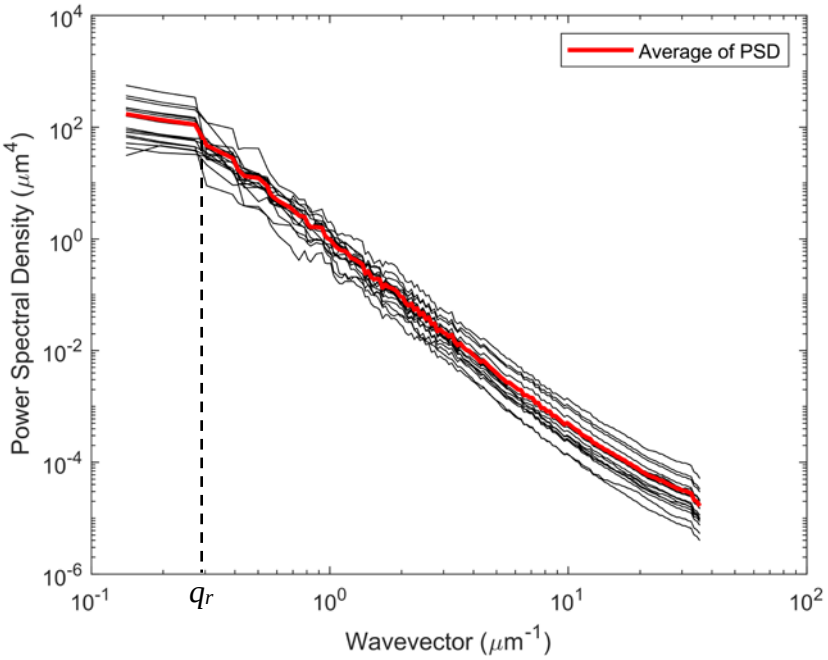

Figure 4.7. Power spectral density curves for 16 sand grain surfaces (average power spectrum marked by red line).

Fig. 4.7 presents the PSD data of 16 sand grain surfaces. The lower and upper limits of the wavevectors were determined by the largest and shortest wavelengths corresponding to the span and resolution, respectively. To validate the PSD computations, two RMS values were compared using Eqs. (4.10) and (4.14). Area under the PSD curve, which is a zeroth moment of PSD, can be related to the RMS as expressed in Eq. (4.10). The two RMS values showed a very good agreement in all cases; the relative difference between two values is less than 0.1%.

The interesting aspect of the PSD results is that every sand grain surface shows fractality as presented in the nearly perfect straight line for $\log q > 0.3\ \mu m^{-1}$. An average fractal dimension determined from the PSD results is about 2.2. Previous studies evaluating the fractal dimension of soil grain morphology are consistent with this results (Orford and Whalley, 1987, Vallejo, 1995). Bouchaud (1997) measured the fractal dimension of surfaces generated by crack propagation, and found that the crack-generated surfaces generally have a fractal dimension, $D_f = 2.2$. It was also shown that the surfaces of coarse textured rock granite and fine grain rock basalt, originated from different geologic processes, show a very similar power spectra; both of the surfaces revealed the fractal dimension $D_f = 2.2$ (Persson et al., 2005). This indicates that there might be universal characteristics of the power spectral density for surface of geo-materials with different mineralogy, scale, and origin, although this requires further investigation.

Close inspection of the PSD results gives around $0.3\ \mu m^{-1}$ of roll-off wavevector, where the power of the spectrum drops to zero. This long distance roll-off is commonly observed by the solid surface with a conglomerate of small particles (Persson et al., 2005). Similar to the fractal dimension, the roll-off wavevector of the sand grain surfaces tested is practically the same despite of the different roughness parameters shown in Table 4.1. This roll-off wavevector might correspond to the largest size of particles forming the sand grain. In the case of asphalt and concrete road pavements, the surface has a well-defined roll-off wavevector of $q_r = 2\pi / (1\ cm)$. The 1 cm of roll-off wavelength is associated with the largest stone grains in the asphalt (Persson, 2006).

Sand grain surfaces characterized here were considered as fresh surfaces, i.e., they have not experienced a noticeable long-term loading. Therefore, they are susceptible to delayed fracturing of contact asperities. It would be interesting to study contact maturing process by comparing the same surface before and after it has been subjected to constant loading. This would demonstrate the time-dependent crushing and fracturing of the textural features on the nominal

contact area. Using some of the sand grains shown in Fig. 4.1, the difference between fresh and matured surfaces will be investigated using the three-grain load testing in the next section.

4.4. Three-grain test

In order to characterize the time-dependent damage on sand grain surfaces under constant loading, three-grain testing was performed. The experimental setup is illustrated in Fig. 4.8. The sand grains characterized in the previous section were chosen for the three grain test. In each test, three grains were positioned on the SEM stub in the corners of an equilateral triangle. The three grains were firmly attached to the SEM stub with a super adhesive, so that possible translation and rotation caused by loading were restricted. The surface profiles of the contact-prone area on the grains (topmost portions of grains) were obtained from the AFM scanning before the grains were subjected to sustained loading. The term *fresh surface* is used here to refer to the surface before subjecting it to constant loading. After the roughness of the topmost surface of the grains was characterized by AFM, the three grains were covered by a glass plate, and loaded with 7.2 N of total dead weight at the centroid of the equilateral triangle. Each grain was loaded with approximately 2.4 N of vertical force for 3 days. The tests were carried out under the conditions of 25°C temperature and 60% humidity. The horizontal load on the three grains, which have been possibly induced in the process of loading, was neglected. After 72 hours of loading, the identical area scanned before testing was measured again by the AFM. A comparison of the matured surface texture after 3 days was made with the one of the fresh contact surface.

The AFM scans of both the fresh and matured surfaces were carried out over 60 μm × 60 μm area with the number of 512 scan points. In order to find the identical area on the two images where nominal contact occurred, a comparison of the AFM data before and after loading was performed, as plotted in Fig. 4.9. Based on the noticeable morphological features in both images, the two AFM scans were matched. In the figure, one can observe the similarity in the surfaces before and after constant loading (yellow and red squares indicate the textural features used for identification of the image areas). Once the corresponding general areas in the two images have been identified, the images were cropped to include identical areas. As represented in Fig. 4.10, the possible largest square cropped area was 45 μm × 45 μm with 384 by 384 (total 147,456 points)

pixels, leading to the resolution of 0.117 μm (117 nm). Fig. 4.11 presents the original and matured cropped contact surfaces, identified in Fig. 4.10. The grain used in this demonstration is grain no. 15 in Fig. 4.2. Overall surface geometry is similar to one another, yet the morphological changes on the grain surface indicate the time-dependent damage generated by the sustained loading. The following analysis will reveal that the asperities with high elevation are most vulnerable to the contact damage.

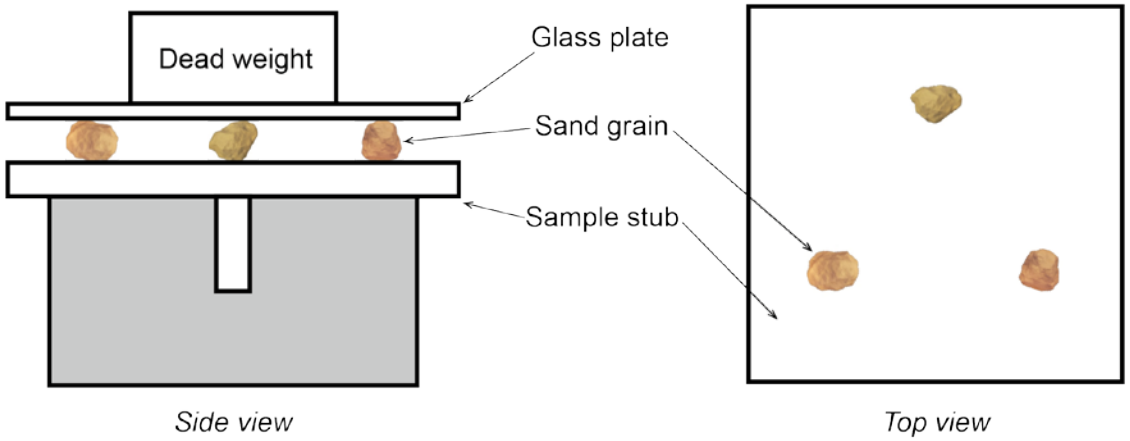

Figure 4.8. A schematic of the three grain test setup.

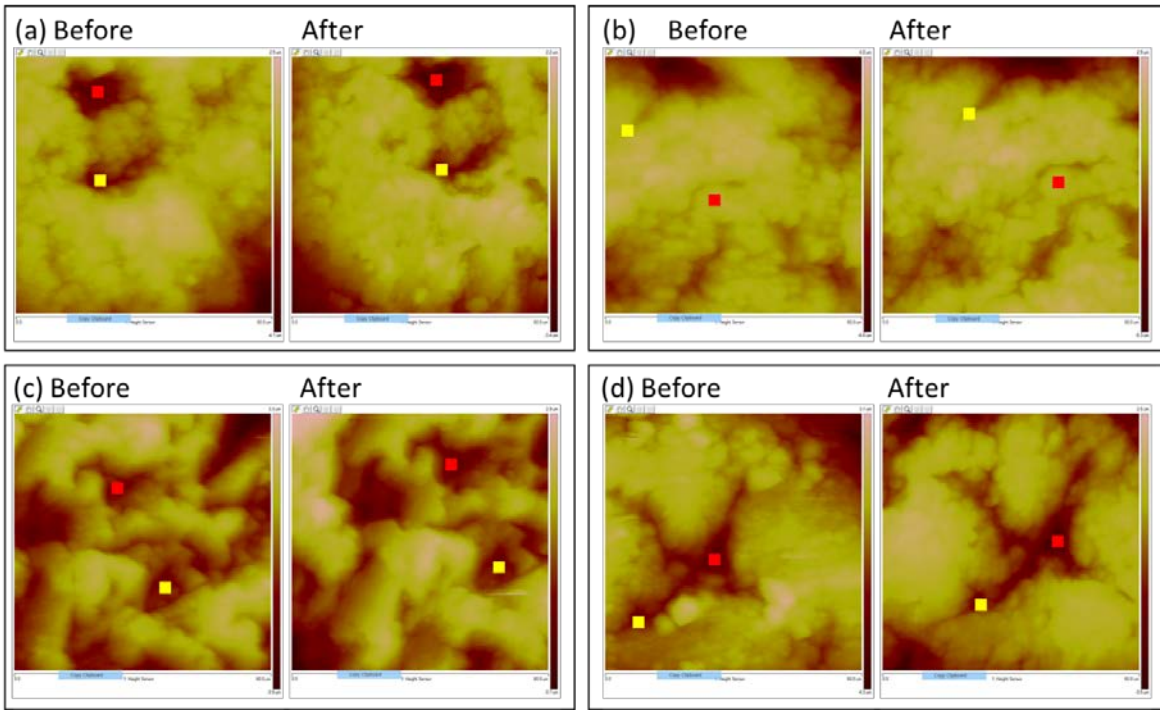

Figure 4.9. Finding contact-prone area before and after loading (red and yellow squares indicate the same major morphological features on two surfaces).

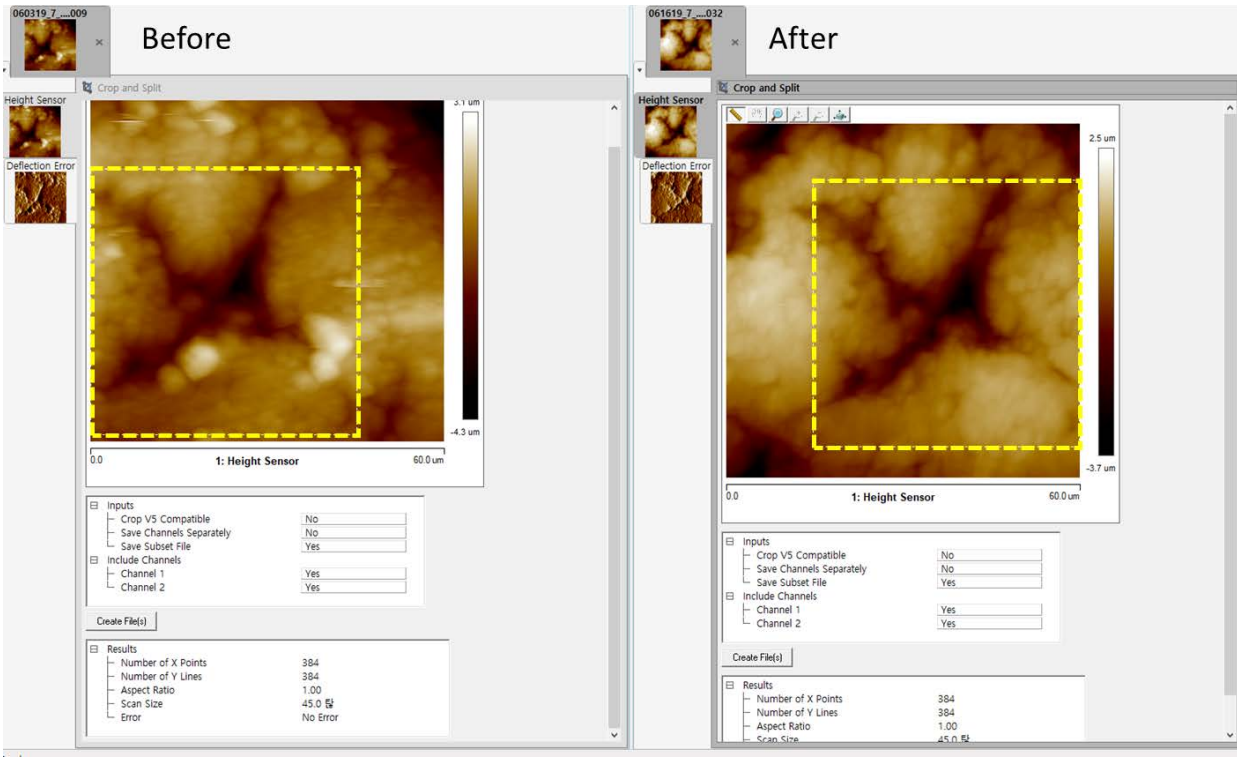

Figure 4.10. Cropping operation for the identified region (grain no. 15).

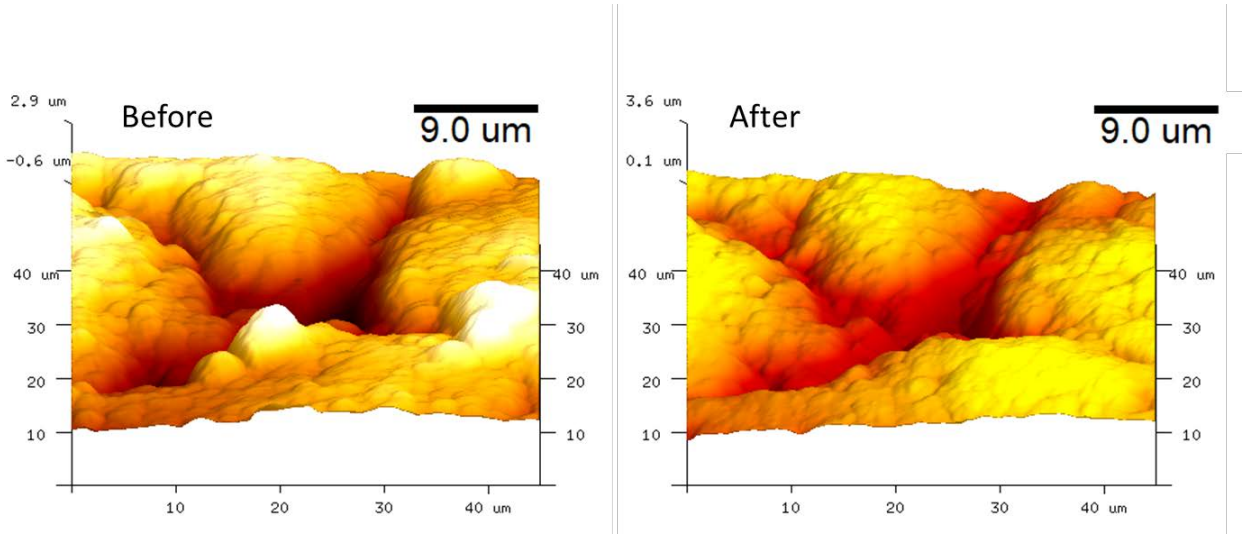

Figure 4.11. Images of grain surfaces before and after subjected constant loading (grain no. 15).

Based on the elevation information at different time in Fig. 4.11 (t = 0 and t = 3 days), the morphological change was characterized using BAC and PSD. Fig. 4.12 presents the change in height distribution of two surfaces plotted as the Bearing Area Curve (BAC) and histogram. The BAC, which is also known as the Abbott-Firestone curve, is a cumulative curve of the distribution

histogram of the profile height. Thus, a point on the plot is the probability of the heights higher than a given height. The BAC also describes the skewness by measuring probability density at different profiles. Compared to the histogram, the BAC is less susceptible to discretization of height interval, resulting in relatively smooth curve (Barber, 2018). As the topmost asperities first get into contact with the glass plate and fracture due to significant stress concentration, a decrease in the distribution of higher profiles was observed in the matured surface after 3 days. The RMS decreased from 882 nm to 786 nm. The PSD curves for the two surfaces are plotted in Fig. 4.13. The PSD of the matured surface is located lower on the graph than the one for the fresh surface for all wavevectors.

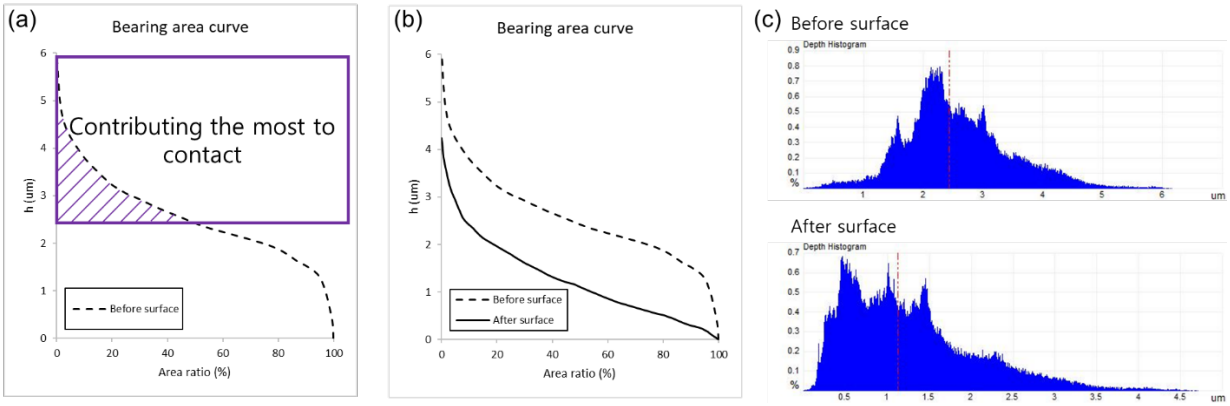

Figure 4.12. Bearing area curve and probability distribution of profiles (grain no. 15).

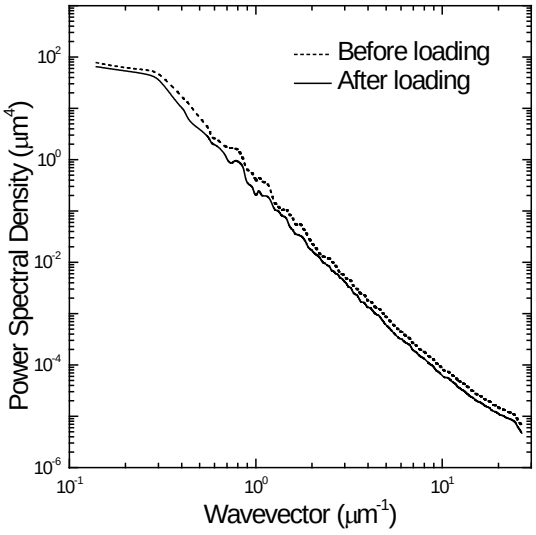

Figure 4.13. PSD of the rough surface before and after being subjected to sustained load of 2.4 N (grain no. 15).

Although the surface height distributions of the sand grains generally obey the Gaussian distribution as shown in Fig. 4.4, they are skewed to the right side. In such cases, the PSD associated with the entire surface profile is not well suited to identify geomorphological properties. Natural sand grain surfaces, which have been subjected to weathering, display a non-symmetry in the elevation range of $-h$ to h. Among the morphological features on the nominal contact area in three-grain tests, only the top portions of asperities are likely to come into contact with a glass plate. As a result, the time-dependent fracturing of contact asperities is dominant in the portions of profiles with higher elevations. It is interesting to analyze the upper profile power spectrum for characterizing morphological alteration and contact maturing process. Persson et al. (2005) first introduced a PSD calculated by the upper portion of surface profiles. The upper and lower PSD computations are straightforward; they only take into account the profiles within a given range, and profiles outside that range are considered to be zero. More details can be found in Persson et al. (2005).

Fig. 4.14 presents the PSD calculated by using only upper 50% and 20% profiles, and corresponding topologies used in the PSD computations. Different area ratio considered has a noticeable influence on PSD results. When only the profiles with higher heights are considered, the difference between the PSDs calculated for fresh and matured surfaces increases. The higher the profile portion used in the PSD computation, the larger the drop of the PSD observed. It indicates that the upper topology is more likely to be affected by the delayed fracturing of contact asperities. This leads to a conclusion that contact maturing is strongly dependent on the upper profiles of the roughness. When it comes to the PSD associated with lower profiles, it is expected that the PSDs of two data sets will show similar PSD curves, as the lower profiles are not affected by contact static fatigue (maturing). As anticipated, the PSD results of lower 20% and 50% profiles are almost identical, as shown in Fig. 4.15. It can be concluded that the lower profiles (basins or valleys) are not affected by the fracturing of surface features, because the contacts are made by asperities in the upper profiles.

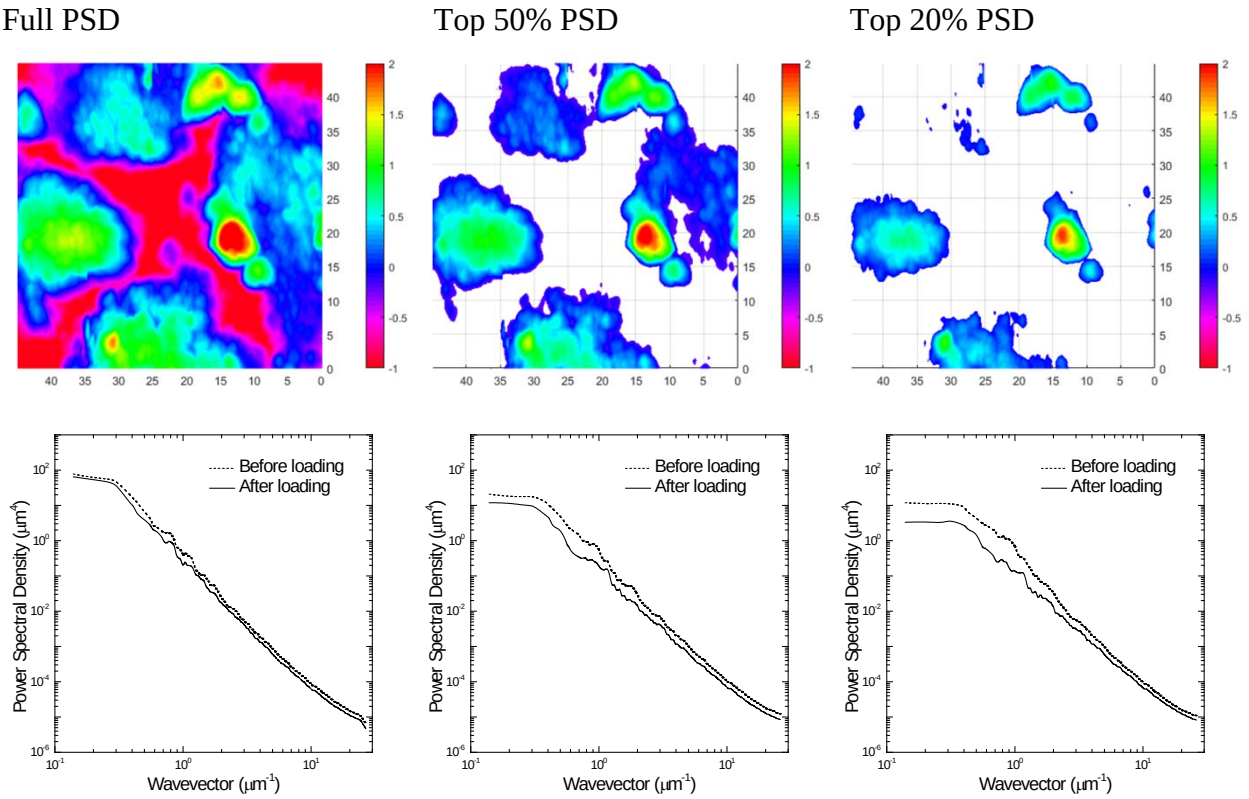

Figure 4.14. PSD curves for the full profile and for the upper portions of the surface topography (grain no. 15).

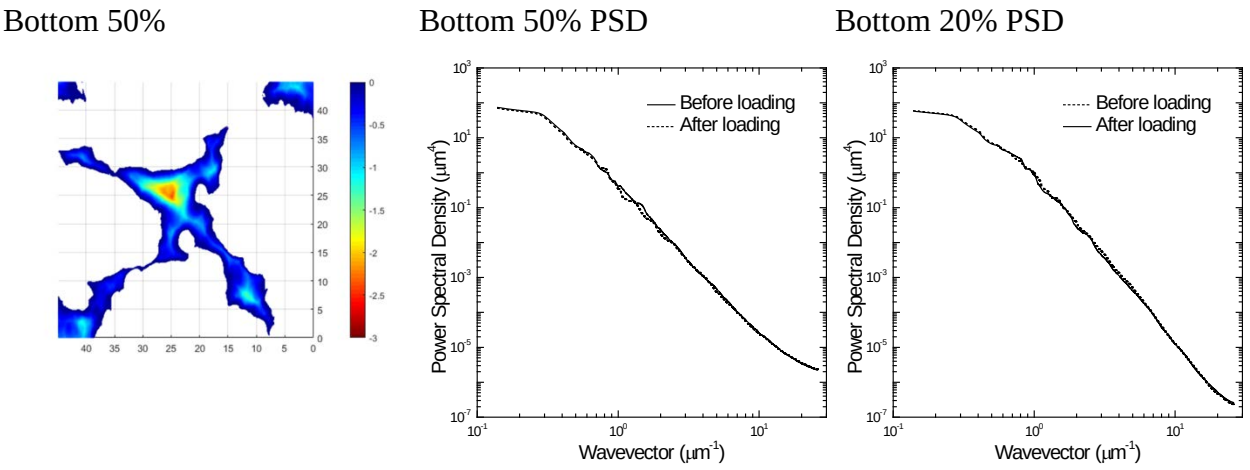

Figure 4.15. PSD curves for the lower portions of the roughness topography (grain no. 15).

Fig. 4.16 shows the cases where the surface morphological evolution over time is noticeable when comparing images of surfaces before and after the application of sustained loading. Delayed fracturing of contact asperities were captured in the AFM images. With regard to the histogram, the original height profile shifted to the left-hand side over time, indicating the time-dependent damage of contact (top) asperities. It is shown most clearly in the histogram of grain no. 10 that higher elevation topographical features (asperities) were fractured during sustained loading and removed from the profile. Originally with negative skewness, the profile distribution moved to the left after loading, bringing skewness closer to zero. The profile distributions of lower heights are almost identical, as valleys are not affected by contact squeezing. The small variation in the tail of the histogram (left side) might be due to the fact that the two images used for the analysis may be cropped with slight differences. When the surface is subjected to damage caused by maturing, the PSD curves shift down, with the clearest example for grain no. 10 in Fig. 4.16.

There were surface images constructed by the AFM data that the surface morphology subjected to constant loading for 3 days was indistinguishable from the initial surface. Fig. 4.17 illustrates such cases. It seems improbable that the surface topographies before and after loading are different. From these surface images, one may consider this region as a surface where no true contact appeared. The PSD results associated with the entire profiles are consistent with the view, as the PSDs of two surfaces obtained from different times (initial and 3 days after) are not changed.

A morphological alteration, which was not found visually in both surface images and PSD computed from the entire profiles, was captured in the PSD analysis of upper 20% profile, as illustrated in Fig. 4.17. This reveals that time-dependent damage occurs not only on major asperities and noticeable features, but also on smaller bumps, invisible in the image. Because of fracturing of these small textural features, the significant decrease in the upper 20% PSD over the range of small wavelengths (large wavevector) was observed in the cases of grain no. 8, 12, and 16. Grain no. 9, however, shows a substantial drop of the PSD in small wavevector. The reason for this rather unexpected result is not completely clear, but a possible explanation for this outcome is likely to be the major damage marked as red square at the AFM images for grain no. 9 in Fig. 4.17. Note that the major asperity corresponds to the large wavelength, indicating that removing the asperity leads to the decrease of PSD in small wavevector range. This asperity was solely loaded before fracturing, leading to the relatively less contact pressure on other area. That is probably why the PSD of small wavelengths was almost unchanged over time.

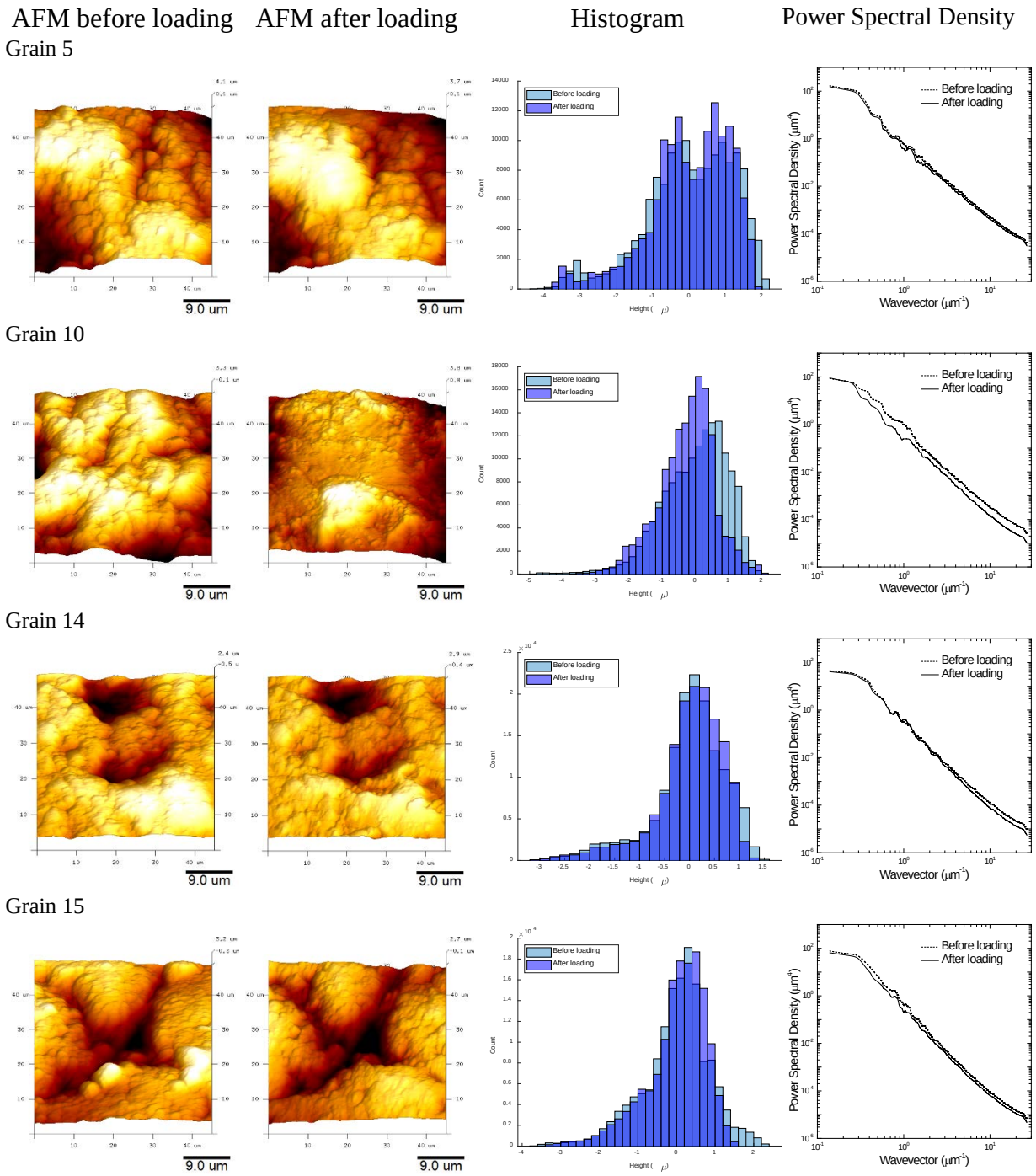

Figure 4.16. Morphology evolution on the contact region identifiable in full PSD.

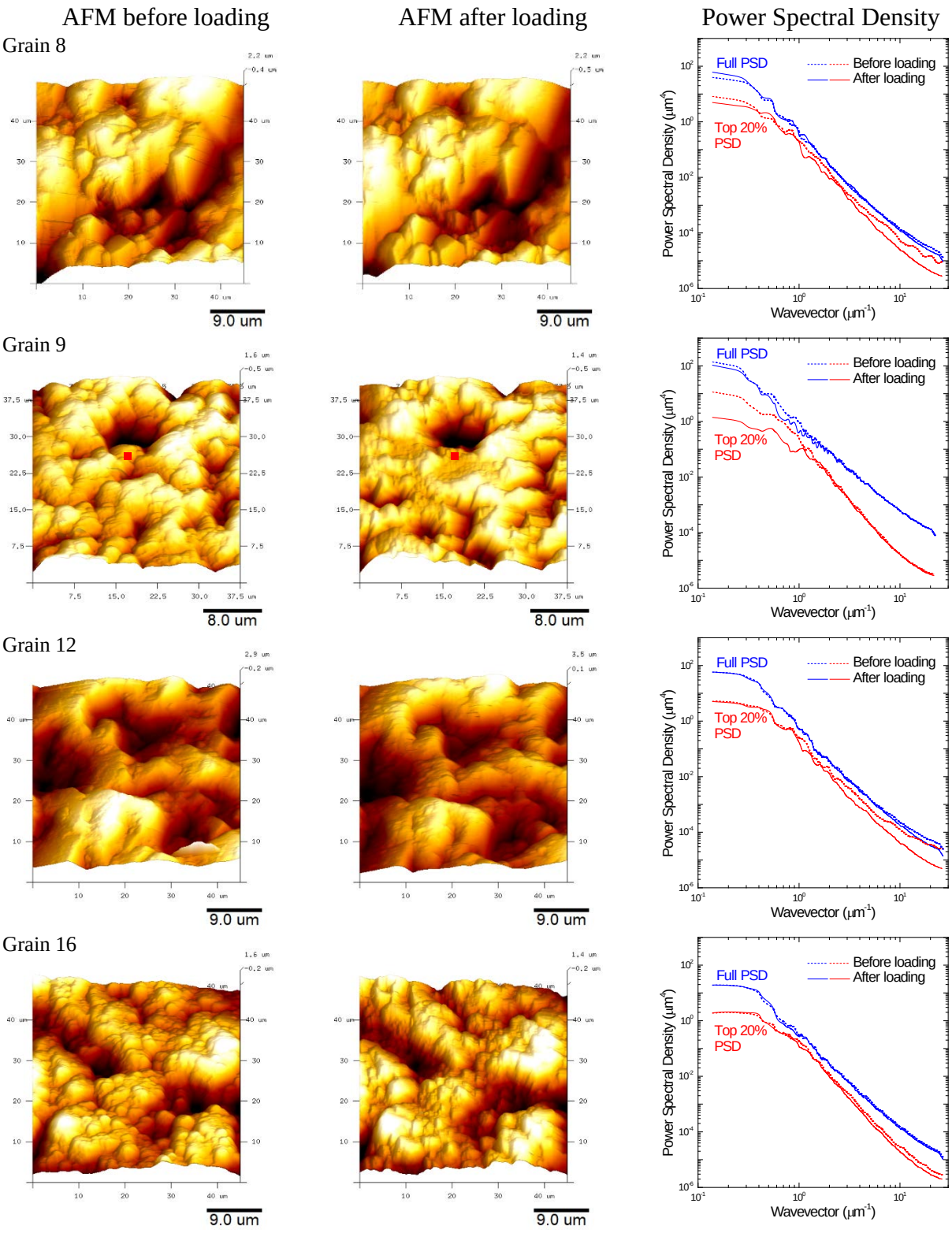

Figure 4.17. Morphological change on the contact region over time: the cases where contact maturing could be identified by upper 20% PSD.

In summary, constant loading on rough surface causes time-dependent damage in both major asperity and small bumps, illustrated in Figs. 4.16 and 4.17. Fig. 4.18 shows the average PSDs of the 8 grains investigated in Figs. 4.16 and 4.17. Overall, the PSD shifted down over time, and this decrease is more substantial when only upper 20% profiles were taken into account (Persson et al., 2005, Kanafi and Tuononen, 2017). From the results of matured contacts loaded for 3 days, one might expect that contact maturing is more intense at field, as sands there experience a sustained loading longer time, several months or years.

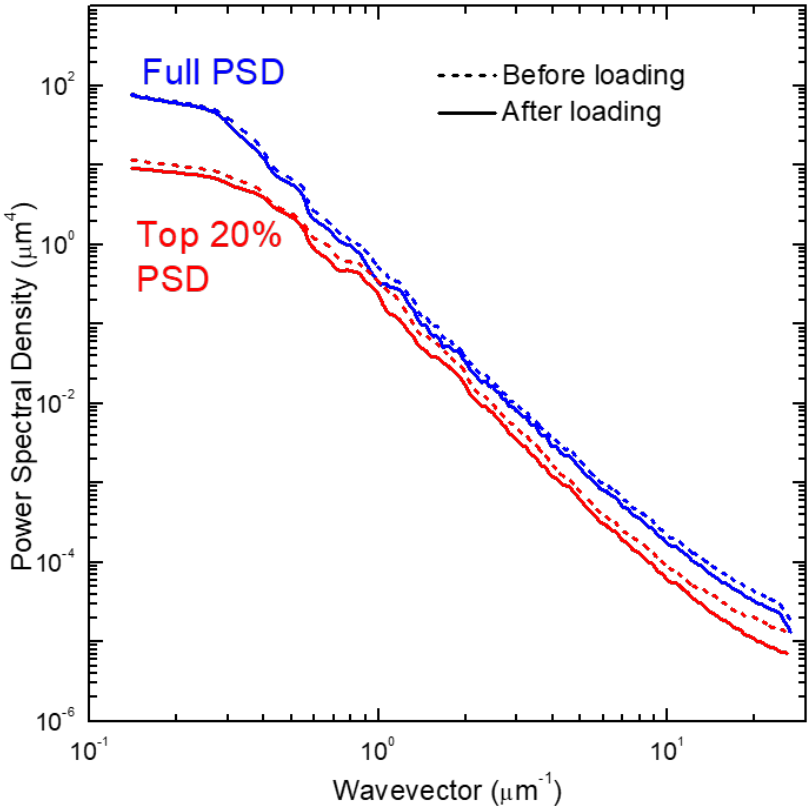

Figure 4.18. The average PSD of 8 grain surfaces in Figs. 4.16 (grain no. 5, 10, 14, and 15) and 4.17 (grain no. 8, 9, 12, and 16).

There were exceptional cases where the characterization of the surface morphological change is pointless. Fig. 4.19(a) shows a flattened surface over time. The reason for this one-side flatting is not clear, but it might be due to an eccentric loading on three grains. Fig. 4.19(b) represents a case where the large piece of the surface, marked as red square, was broken. The chip brought about a damage deep into the surface, causing difficulties of analyzing data.

(a) AFM before loading (Grain 7)

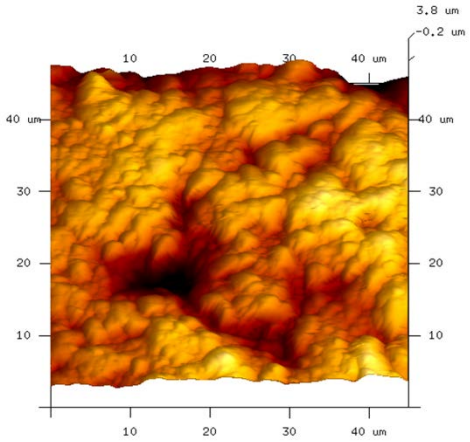

AFM after loading (Grain 7)

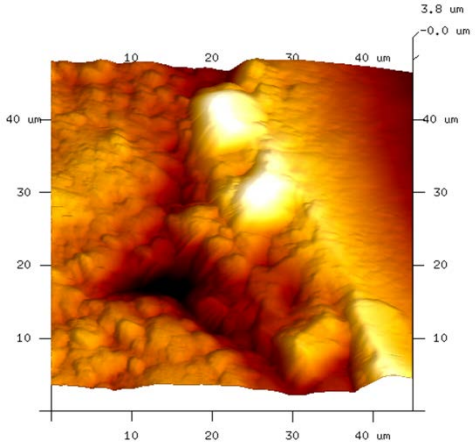

(b) AFM before loading (Grain 11)

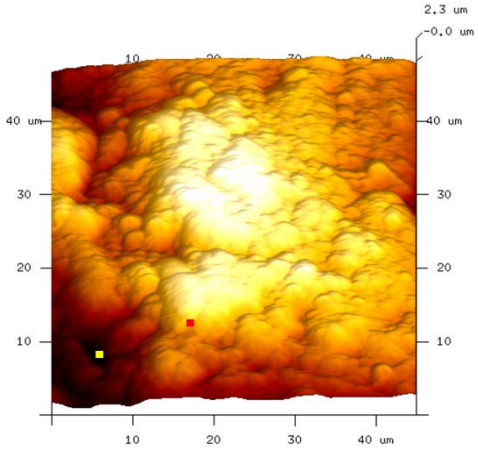

AFM after loading (Grain 11)

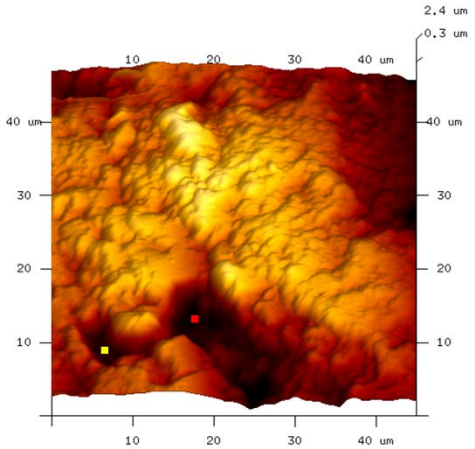

Figure 4.19. Unusual cases of morphological evolution images on the contact region: (a) one side of the surface is flattened, and (b) the major separation/indentation at the location marked by the red square.

In addition to contact maturing caused by the long-term stress concentration, surface migration associated with chemical processes can contribute to alteration of surface textural features. These effects accelerating the contact maturing process are not considered here.

4.5. Grain-scale laboratory testing

The time-dependent behavior of sand and sand grains subjected to sustained loads was a subject of other studies (Michalowski et al., 2018a, Wang, 2017). An apparatus constructed to test time-dependent behavior of individual sand grains was described by Wang and Michalowski (2018), and it is illustrated in Fig. 4.20. In the tests on individual grains, a single sand grain is placed between two steel plates, and the grain is subjected to the constant loading through two contacts. Over time, the apparatus measures a time-dependent grain deflection, also referred to as *convergence*, caused by the evolution of both contacts and a contribution of creep of the grain core material.

Fig. 4.21 presents the time-dependent relative displacements of two platens (convergence) loading a sand grain, as presented in (Michalowski et al., 2018a). Constant loads of 1.3 N and 2.4 N were applied to the four different sand grains over 25 days. The convergence was measured as the change in the distance between two loading platens over time. Table 4.1 shows numerical values of convergence obtained from the tests.

The rough grains with large RMS value produced larger convergence for both loading conditions. This strong relationship indicates that a large component of the convergence is possibly due to time-dependent fracturing of contact asperities, where high stress concentrations are more likely to occur on rough surfaces. In Fig. 4.21, the time-dependent convergence was saturated after a rapid increase in the first few days. The approximately constant rate of convergence after 20 days is likely to be caused by the creep of the grain core material, rather than contact maturing. This was confirmed with convergence tests using borosilicate glass beads (Michalowski et al., 2018a). The spherical bead with negligible surface asperities showed the low but constant rate of convergence under sustained loading, similar to the behavior of the grains with low roughness. The convergence of the grains with low roughness (tests A and B) is, therefore, expected to have a substantial creep component due to time-dependent deformation of the grain core mineral. When the applied force increases, the creep increases as well. Test B exhibits greater amount of convergence than the test with a lower force (test A). In the case of test D, however, the convergence was large despite the lower vertical load. This indicates the time-dependent asperity fracturing is a predominant process in grain deflection. Additionally, a rough grain surface with

rich textural features is susceptible to surface maturing on nominal contact areas, resulting in relatively high convergence.

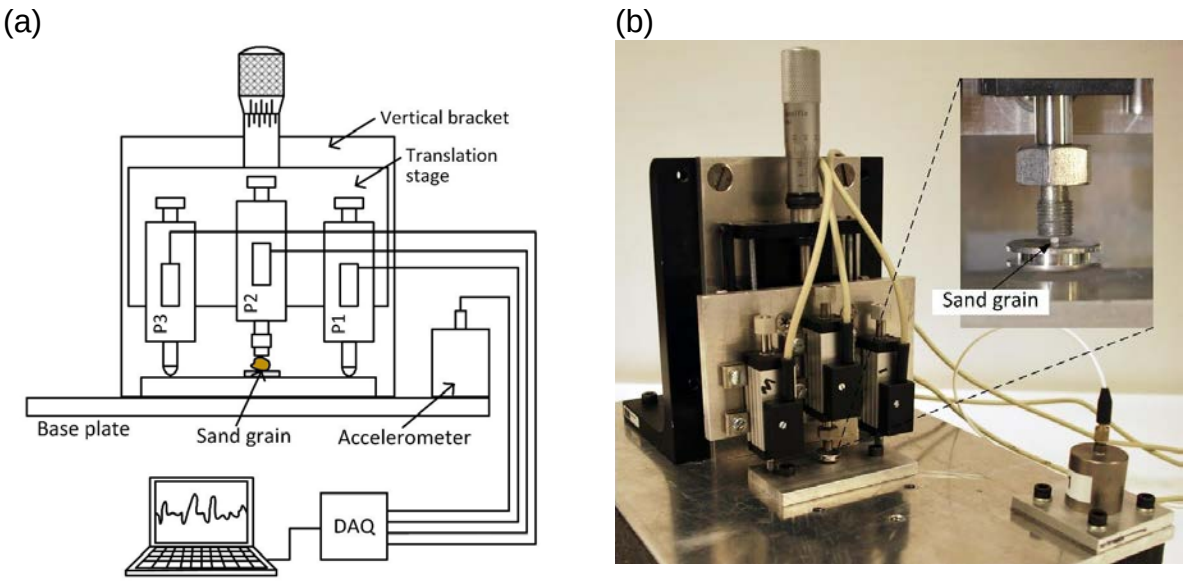

Figure 4.20. The grain-scale laboratory testing instrument: (a) a schematic, and (b) photographic view of the apparatus (Wang, 2017).

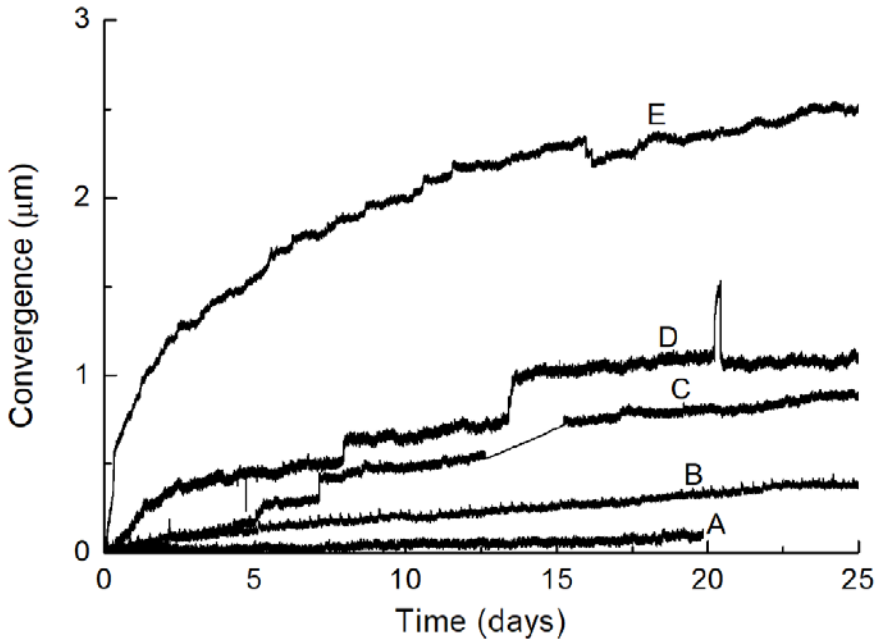

Figure 4.21. Grain-scale tests; convergence curves of sand grains with different roughness, after Michalowski et al. (2018a).

Table 4.2. Summary of grain scale tests (Michalowski et al., 2018a).

Test	RMS (nm)	Applied Force (N)	Test duration (days)	Time-dependent convergence		
				1 day (nm)	5 days (nm)	20 days (nm)
A	28.6	1.3	20	5	10	100
B	28.6	2.4	25	10	100	310
C	321	2.4	25	25	210	780
D	577	1.3	25	170	451	1090
E	621	2.4	25	845	1582	2385

4.6. Summary

Surfaces of sand grains are characterized by considerable roughness at the microscopic scale. Such surfaces do not make contact everywhere when two grains are squeezed together; instead, the peaks (asperities) on the two surfaces come into contact. As a result, a true contact area is small compared to the nominal contact area, causing the stress concentration followed by the fracturing of contact asperities.

The microscopic observations of grain surfaces using the AFM demonstrate that a rich texture and self-affine characteristic. The grain surfaces appear to be random, but the quantitative analyses presented common statistical characteristics. An average fractal dimension (D_f) and roll-off wavevector determined from the 16 PSD results were about 2.2, and 0.3 μm^{-1}, respectively. Despite different roughness parameters, the measured power spectral were surprisingly consistent, indicating the possibility of universal characterization in grain surfaces.

Three grain testing is used to quantitatively characterize changes of surface morphological features before and after contact maturing. The time-dependent surface alteration obtained from the AFM scan of the same area at different times shows that the RMS decreases and the PSD of the matured surface is located lower on the graph than the one for the fresh surface for all wavevectors. The upper 20% PSD analysis reveals that the asperity with higher elevation are susceptible to the contact maturing process. Also, it could capture invisibly small asperity fracturing, which is not captured by visual inspection.

Finally, the results of the grain-scale laboratory experiment are presented to test time-dependent behavior of sands subjected to sustained loading. The experiment presents that a rough

grain surface with rich textural features is vulnerable to surface maturing on nominal contact areas, resulting in high asperity deflection.

Chapter 5

Hybrid Model of Grain Contact Behavior

5.1. Introduction

The research in the Chapter is the development of numerical tools to capture key characteristics of static fatigue or maturing of grain contacts. Relatively few numerical models exist to aid in understanding or describing time dependent behavior of sand. Observations and laboratory testing provide indispensable physical evidence for contact maturing, but utilizing the consequences of contact maturing for the benefit of engineering practice requires predictive capabilities (mathematical models). In addition, calibrated models can provide information that might be difficult to obtain through physical testing. Therefore, complementary to experimental investigation is the numerical approach. To achieve the research objectives, a numerical model was developed in this part of research, demonstrating the behavior of the contact maturing process over time.

The static fatigue hypothesis has been suggested in Michalowski and Nadukuru (2012), but substantial evidence supporting the hypothesis is yet to be collected. Michalowski and Nadukuru (2014) observed relative displacements of grains under constant loading using the grain-to-grain contact test apparatus. Although the study gave quantitative evidence for the hypothesis, it suffered from the inaccuracy of measurements caused by the grain mounting glue. Consequently, an

advanced apparatus was constructed to measure a simultaneous response of two contacts on a single grain without a need for using adhesive (Wang and Michalowski, 2018). Using the grain-scale experiments, Michalowski et al. (2018a) demonstrated that the micro-fracturing of textural features on the surfaces leads to grain deflection under constant load. In the research, the soft oedometer testing of sand samples was also conducted to identify the time-dependent increase in radial stress, which is a result of increasing stiffness of sand owed to maturing contacts of sand grains. Their findings – delayed fracturing of contact asperities – provide experimental support for static fatigue hypothesis. This chapter focuses on the fundamental understanding of the phenomenon as well as collecting numerical supports for the hypothesis.

In terms of the grain-scale numerical simulations, many attempts have been described in the literature. Most of these efforts consider the behaviors of the entire grains and their interactions, rather than a grain surface and its evolution at the contacts (Cil and Alshibli, 2014, Cil and Alshibli, 2012, Fu et al., 2017, Sun et al., 2018, Wang et al., 2015). Because the micro-fracturing of morphological features takes place on the contact areas, a microscopic simulation accounting for rich textures on the nominal contact area is essential for reproducing static fatigue process. In general, taking into account the grain roughness is impractical with regard to meso- or macro-scale modeling, as it is computationally demanding. Instead, a number of studies have investigated the influence of grain shapes (rather than surface texture). Additionally, the existing literature rarely involves simulations of the time-dependent effects. Previous research tends to focus on short-term loading followed by grain fracturing (splitting), rather than long-term sustained loading (Robertson and Bolton, 2001, McDowell and Harireche, 2002, Cheng et al., 2003, Cil and Alshibli, 2012, Cil and Alshibli, 2014). The exceptions are (Nadukuru, 2013, Wang, 2017, Wang and Michalowski, 2015, Michalowski et al., 2018a). With regard to rocks, the numerical simulation of long-term time effects in Lac du Bonnet granite is well documented in Potyondy (2007).

Based on the preliminary research and developments, the study in this Chapter aims to collect numerical support for the working hypothesis and identify the consequences of contact maturing. The hybrid model is suggested in this study to reproduce the grain-scale laboratory tests and demonstrate contact maturing process on the nominal contact area.

5.2. Model overview

Experimental results indicate the time-dependent micro-fracturing of textural features brings about firmer and stiffer contacts. This study aims to develop numerical tools to capture key characteristics of maturing of grain contacts. To achieve this research objective, a numerical model was developed, demonstrating the behaviors of the contact maturing process over time.

As observed in the grain-scale laboratory tests, creep of the core material in silica grains is inevitable throughout the tests, because one cannot load the contacts without loading the grains. However, it is maturing at grain contacts that plays a key role in the process and is the focus of the investigation. Separating the two time-dependent effect measured in the tests is not a trivial matter. Simulating both processes simultaneously with high accuracy using a single approach is not feasible due to the extreme computation demands. A single grain model with detailed asperities everywhere requires an enormous amount of elements presenting rich textural features. Another approach for modeling the grain with rough surfaces is a nominal contact model that simulates only a small contact area where a grain contact occurs without the consideration of convergence in the grain core material. Although the simulation of the small nominal contact area, ignoring the core material, reduces the computational effort, it offsets the accuracy of the model. While most of grain convergence involves the contact maturing process limited to the contact area, the creep of the grain core material may become dominant in case of grains with low roughness.

An alternative numerical modeling involves a high resolution near contact area for taking into account microscopic surface asperities, but low resolution in the grain core for faster computations. For example, a similar attempt was made by Wang and Michalowski (2015) to simulate the time-dependent grain convergence using the Distinct Element Method (DEM). However, the model was not well suited to reproduce the gradual increase of convergence over time observed in the laboratory tests due to its limitation on the resolution of the sub-particles used to construct the grain. Instead, it showed distinct step-wise jumps in convergence. Motivated by these drawbacks regarding a single model, this study proposes a hybrid model calculating surface maturing and creep of core material separately.

The hybrid model proposed is to simulate half of the total convergence of a single grain loaded through two contacts. The developed hybrid model consists of (1) half-grain distinct element model, (2) single-grain finite element model, and (3) nominal distinct element contact

model. The basic assumption made in the model is that a total convergence (δ_{total}) of a single grain caused by sustained loading is the sum of the time-dependent deflection in the core material in one half-grains ($\delta_{\text{grain core}}$, creep) and the one associated with micro-fracturing of contact asperities (δ_{contact}, contact maturing) on one nominal contact surfaces (considered only half of the sand grain as it is symmetry) as following

$$\delta_{total} = \delta_{grain\ core} + \delta_{contact} \tag{5.1}$$

Fig. 5.1 presents a schematic of the hybrid model showing the model components. The half-grain (Fig. 5.1(a)) and nominal contact (Fig. 5.1(c)) models take into account convergence caused by creep of grain core material and asperity fracturing at contacts (contact maturing), respectively. The small nominal contact model in Fig. 5.1(c) is a part of the grain, which will be simulated separately due to different scale. The nominal distinct element contact model requires information such as the size of the contact as well as the vertical and confining stresses; this information comes from the single-grain finite element model (Fig. 5.1(b)). Because the partition of convergence among creep of the grain core and contact maturing on contacts is not known from experiments (only the total convergence can be measured in the tests), the hybrid model calibration with the laboratory tests was conducted using the total convergence.

Grain-scale laboratory tests using the grains with low roughness exhibit a convergence behavior predominantly owed to creep of the grain core material; therefore, such tests become useful in developing some knowledge of the ratio of the convergence due to grain creep and contact maturing.

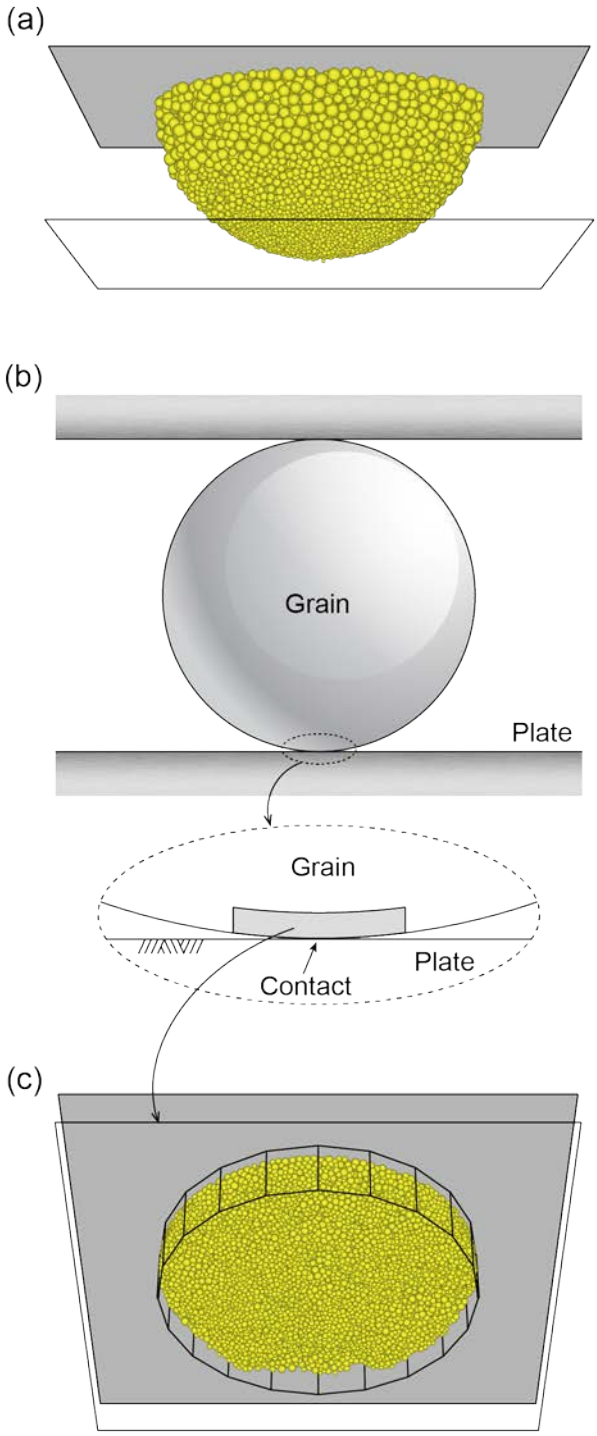

Figure 5.1. A schematic of the hybrid model and the corresponding components: (a) distinct element half-grain model, (b) elastic grain model for finding stresses at the contact region, and (c) distinct element contact model.

5.3. Half-grain contact distinct element model simulations

In the first step of the hybrid model, a half-grain DEM simulation is conducted to predict the first component of grain convergence, which is the creep of grain core material. As shown in Fig. 5.1(a), this model consists of a hemisphere assembly of sub-particles (800 μm diameter) which model the grain core material, and a steel plate, which models a part of one grain contact. The half-grain DEM assembly has three different layers with varying radius of sub-particles: r_1 = 15.27 μm (average) and N_1 = 3,573 balls with 200 μm thickness, r_2 = 9.97 μm and N_2 = 4,177 balls with 100 μm thickness, r_3 = 6.36 μm and N_3 = 5,320 balls with 100 μm thickness, from the top of the half-grain. The average radius and number of all sub-particles in the half-grain DEM are r = 9.95 μm and N_3 = 13,080, respectively. Compared to simulations of entire grains, this half-grain DEM model is efficient as the calibration of the parameters requires large computing time with many iterations. At this stage, time-dependent parameters of PSC model, β_1, β_2 and $\bar{\sigma}_a$, were calibrated with the grain-scale test where creep is dominant. Among several laboratory tests with different loads and roughness, shown in Fig. 4.21, test B was chosen to calculate creep deformation inside the grain. Since the grain used in test B had very flat surfaces (RMS = 28.6 nm), it was expected that convergence due to contact maturing would be negligible.

In literature, occasional attempts have been made with the purpose of simulating a sand grain using DEM with the Bonded Particle Model (BPM) suggested by Potyondy and Cundall (2004). Among them, the model by Cil and Alshibli (2014), calibrated with 1D compression tests on sand, seems to be well-founded. By using their suggested calibrated parameters regarding bonded agglomerates, it was possible to focus on the calibration of the time-dependent PSC model. The model parameters used in the half-grain DEM simulation are presented in Table 5.1, except for the time-dependent parameters, which are sought through the calibration with test B, and are presented in Table 5.2. Since Potyondy (2007) suggested the PSC model for analyzing time dependent stress corrosion for rocks, few studies associated with the PSC model have been conducted at grain scale.

Fig. 5.2 shows the calibration results of the half-grain DEM compared to test B, and the resulting PSC parameters are summarized in Table 5.2. The calibration of time-dependent parameters was done by matching convergence curve with test B This is because the grain surface in test B is not completely smooth, causing a small amount of surface maturing at contacts. Later,

this gap will be filled with a convergence obtained from the nominal contact DEM corresponding to static fatigue.

It is important to note that the convergence in test B (0.19 μm) is very small compared to the size of the half-grain (400 μm), and it is a little larger than the mean radius of sub-particles (0.13 μm) used to construct the model. Reproducing such small convergence with a gradually increasing trend in the half-grain DEM is elaborate. Nevertheless, the calibrated half-grain DEM captures the response of the creep inside sand grain as shown in Fig. 5.2, despite the DAM saturates more than the test result. The values of PSC model parameters in Table 5.2 will be used for the nominal contact DEM that describes the deformation caused by contact maturing.

Table 5.1. Micro-properties used in half-grain DEM simulation (After Cil and Alshibli, 2014).

Model	Properties	Value
Half-grain	Radius (mm)	0.4
Sub-particle assembly	Mass density, ρ (kg/m^3)	2650
	Young's modulus, E (GPa)	70
	Average radius, R_{avg} (μm)	9.95
	Friction coefficient	0.5
	Normal/Shear stiffness ratio, k^n / k^s	2.5
Bonds	Bond radius multiplier, λ	1
	Young's modulus, $\bar{E}_c$ (GPa)	70
	Normal/Shear stiffness, $\bar{k}^n/\bar{k}^s$	2.5
	Mean normal strength, $\bar{\sigma}_c$ (MPa)	750
	Mean shear strength, $\bar{\tau}_c$ (MPa)	750
	Standard deviation of normal and shear strength (MPa)	175

Table 5.2. Calibrated PSC model parameters by the half-grain DEM simulation and test B.

Micro-properties	Value
β_1 (m/s)	1×10^{-14}
β_2	25
Activation stress, $\bar{\sigma}_a$ (MPa)	50

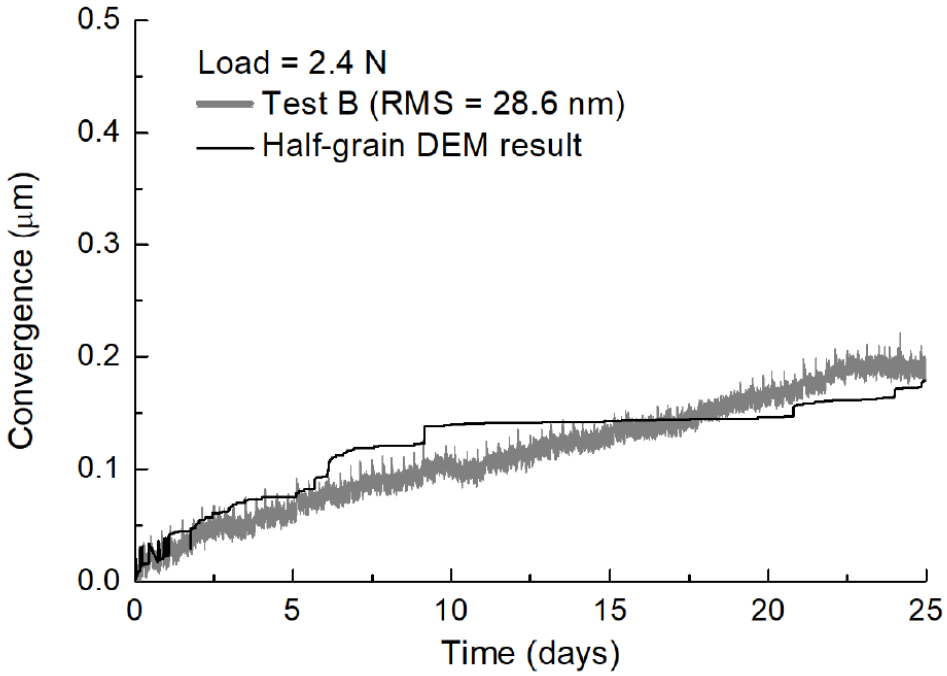

Figure 5.2. Half-grain DEM calibration (one nominal contact) with respect to test B.

5.4. Single-grain finite element model simulations

In addition to the creep of grain core material calculated from the half-grain DEM simulation, estimation of convergence due to contact maturing is needed. This contact will be modeled as a thin contact disc (Fig. 5.1(c)), but the boundary stresses on the disc will be estimated separately, and used as boundary conditions in the contact disc simulations. For that purpose, an elastic finite element model will be constructed, from which the size of the nominal contact and the confining stress will be estimated.

A continuum FE model of a grain was constructed, as shown in Fig. 5.3(a). The commercially available software package Abaqus 8.6 was used with definition of contact pairs. The FE model is purely elastic, and the increase in the contact area over time is not considered. Making use of the axisymmetric modeling with element type CAX4R, the spherical grain was modeled effectively. The numbers of elements in the half sphere cross-section and top (or bottom) plates were 1,950 and 800, and the geometry of the constructed FE model is illustrated in Fig. 5.3(a). Since the contact region where the grain gets into contact with the steel plate shows a

dramatic gradient in stress, a detailed mesh discretization was used in that area to improve numerical accuracy. The physical and mechanical properties used in the FEM simulation of the grain-scale testing are summarized in Table 5.3.

The required confining stress on the nominal contact DEM model is the radial stress in the cylindrical coordinate system. This is the stress that will be obtained from the stress analysis in the spherical grain in the proximity of the contact, and in the spherical coordinate system it is $\sigma_{\theta\theta}$ stress. The discrepancy between two stresses is insignificant, because the radius of the contact disc is small compared to the radius of the grain.

Before making further applications, comparison with an existing solution was conducted to validate the model. Hiramatsu and Oka (1966) suggested the analytical solution calculating the stress field inside a spherical body under conjugate vertical compressive forces (see the Appendix). Among the stress components calculated by using the analytical solutions, the normalized stresses of σ_{rr} and $\sigma_{\theta\theta}$ are plotted in Fig. 5.4 together with the single-grain FEM solution in this study. Both results are presented as functions of distance from center along the direction parallel to the applied force. The normalized stresses induced by the vertical compressive force in FEM show good agreement with the analytical solutions suggested by Hiramatsu and Oka (1966). The small discrepancy for larger value of r/R can be considered insignificant, and they are due to different force boundary conditions on the contact surface and model geometry. While the analytical solution was derived by assuming the uniform pressure acting on the contact area, the pressure distribution on the contact area associated with the single-grain FEM is not uniform; rather it is similar to the Hertzian pressure distribution. Also, the single-grain FEM has fixed boundary condition at the bases of the steel plate, different from the analytical solutions.

Since the developed single-grain FEM produces a reasonable outcome, the laboratory tests applying 1.3N and 2.4N to the single grain are modelled. Table 5.4 presents three outcomes of the single-grain FEM simulation results: the vertical and confining stresses, and the radius of contact area. One might expect the radius and stress components to be proportional to the applied force because of the elastic model. However, the model that takes into account deformation of sphere is geometrically nonlinear. The stress $\sigma_{\theta\theta}$ was taken at the location of the nominal contact boundary estimated as $r/R = 0.993$ and $\theta = 0.024$ rad (for F = 1.3 N) and $\theta = 0.031$ rad (for F = 2.4 N). While the $\sigma_{\theta\theta}$ and a are extracted from the single-grain FEM model, the σ_{rr} was calculated by dividing the total compressive force into the nominal contact area ($\sigma_{rr} = F / (\pi r^2)$), rather than the

FEM results. When it comes to the Hiramatsu and Oka (1966)'s analytical solutions at the point where the single-grain FEM's output was taken in, the values of $\sigma_{\theta\theta}$ are 248.86 MPa and 298.07 MPa for F = 1.3 N and 2.4 N. Both stress values estimated by the analytical solution are slightly smaller than those of FEM simulation in Table 5.4, but the difference is insignificant. The comparison of the contact area obtained from the single-grain FEM model was also made with the outcome of the linear theory of elasticity. This was done by means of Hertz (1882)'s solutions for contacts between the spherical body and elastic half-space. When the elastic half-space is indented by a sphere, the contact radius a can be defined as

$$a = \left(\frac{3PR}{4E^*} \right)^{\frac{1}{3}} \tag{5.2}$$

with the composite elastic modulus E^*

$$\frac{1}{E^*} = \frac{(1-v_1^2)}{E_1} + \frac{(1-v_2^2)}{E_2} \tag{5.3}$$

where P is the compressive load, R is the radius of a spherical body, and the superscripts ^{1} and ^{2} refer to the bodies 1 and 2 coming into contact (in this study, the bodies 1 and 2 mean the spherical sand grain and a steel plate, respectively). The radii of the contact between sphere and elastic half-space calculated by the above Hertz's elastic solution are 18.97 μm and 23.27 μm for F = 1.3 N and 2.4 N, respectively. The values of the single-grain FEM in Table 5.4 are slightly larger, but consistent with Hertz's solutions. Again, these small differences are likely because of the different load boundary conditions. Therefore, they were selected for the input values of the nominal contact DEM, which is the last step of the hybrid model. Once the size of the nominal contact and stresses on the contact disc have been estimated, the last component of the hybrid model is exercised.

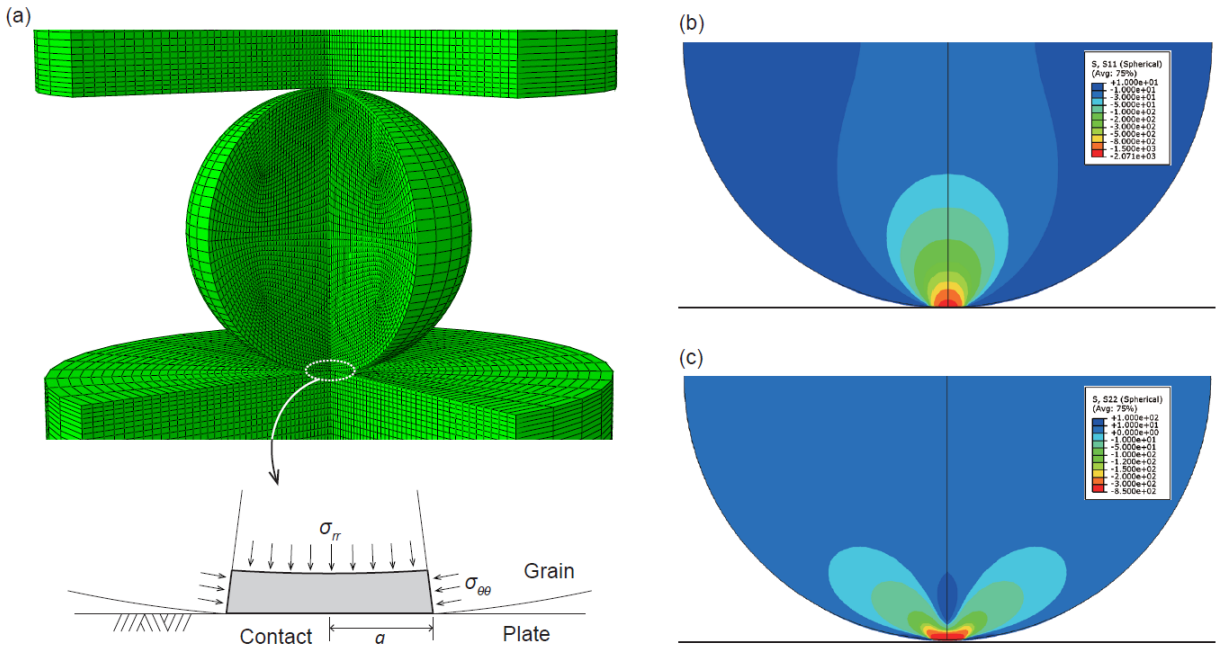

Figure 5.3. Axis-symmetric FEM modeling of a single sand grain for the grain-scale tests: (a) geometric configuration and mesh discretization of a sand grain in contact with steel plates, (b) radial stress distribution, and (c) circumferential stress distribution.

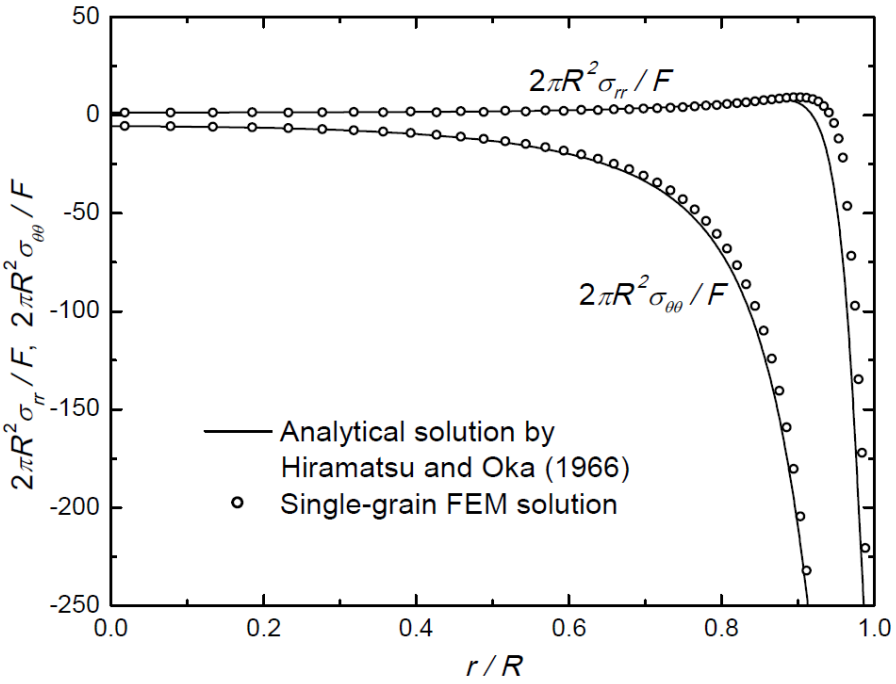

Figure 5.4. Comparison of normalized stresses $2\pi R^2\sigma_{rr}/F$ and $2\pi R^2\sigma_{\theta\theta}/F$ with solutions suggested by Hiramatsu and Oka (1966) along with the normalized radial coordinates r/R ($\theta = 0°$, $\nu = 0.17$).

Table 5.3. Physical and mechanical properties used in the FEM simulation of a grain contact.

	Sand	Plate
Elastic modulus, E (GPa)	70	200
Poisson's ratio, ν	0.17	0.3
Mass density (kg/m^3)	2650	7700
Frictional coefficient	0.5	0.5

Table 5.4. Stress components and radius of nominal contact obtained from FEM.

	F = 1.3 N	F = 2.4 N
σ_{rr} (MPa)	1,088	1,222
$\sigma_{\theta\theta}$ (MPa)	235	276
Nominal contact radius a (μm)	19.5	25.0

5.5. Nominal contact distinct element model simulations

The last component of the hybrid model is designed to simulate the region within the nominal contact of the grain with another grain or a loading platen. The outcome of this simulation is the convergence occurring on the nominal contact caused by time-dependent fracturing of asperities (contact maturing). While the convergence caused by the creep of grain core material takes place through the entire grain, contact maturing takes place within a small area where the asperities on the surfaces of two grains (or grain and a flat platen) come into contact. The nominal contact distinct element model (DEM) is developed to mimic the texture of the grain surfaces measured by AFM.

5.5.1. Generation of the representative numerical surfaces

Contact maturing process on the rough grain surfaces plays a key role in sand ageing, and taking into account the surface morphology is of utmost importance. The initial roughness of grain surface has a great influence on the time-dependent behavior of contacts, as observed in the grain-scale laboratory tests in Fig. 4.21. The aim of this subsection is to construct representative DEM rough

surfaces rich in asperities, accounting for fracturing of the textural features over time. Generating a realistic rough surface DEM assembly follows these steps:

1) Grains are scanned using Atomic Force Microscopy (AFM), Fig. 5.5(a).
2) The elevation profiles of the grain surface are characterized using the statistical techniques to obtain quantitative information.
3) A continuum rough surface is numerically generated based on the Power Spectral Density of the true sand grain surface, Fig. 5.5(b).
4) A cylindrical DEM assembly of sub-particles is generated, Fig. 5.5(c). The diameter of the cylinder is estimated from the single-grain FEM solution.
5) The DEM cylinder is subsequently carved to match the true rough target surface, Fig. 5.5(d).

Fig. 5.5(a) is the AFM scanned image of the grain used in test E, Fig. 4.21, with RMS = 621 nm, and Figs. 5.5(b) and (d) present the numerically constructed surface and a carved DEM assembly for the target surface, respectively. The DEM carved surface, the nominal contact DEM assembly, in Fig. 5.5(d) is a “representative” surface that is to mimic the true surface in Fig. 5.5(a).

To this end, surface analyses of real sand grain surfaces are performed to characterize elevation profiles. Among a variety of stochastic surface analysis techniques for surface characterization, the Power Spectral Density (PSD) was employed to describe and implement the statistical roughness properties. The PSD is a mathematical technique that transfers the spatial surface profiles into the wave vector (spatial frequency) using a discrete Fourier transform. Like the Fourier transform that expresses continuous signals as the pitches (frequencies), the profiles of rough surfaces can be decomposed into different spatial frequencies in the PSD. However, the PSD does not contain the phase but the power that is related to the fractal dimension across the wavevectors. The PSD characterizing both the asperity amplitude and spacing allows the periodic feature of the roughness to be captured and the spatial frequencies in the heights to be identified. The PSD is useful, because it is unbiased by the sampling size and resolution, and many surface properties such as stiffness, adhesion, electrical and thermal conductivity, etc. can be found from the knowledge of the PSD (Jacobs et al., 2017).

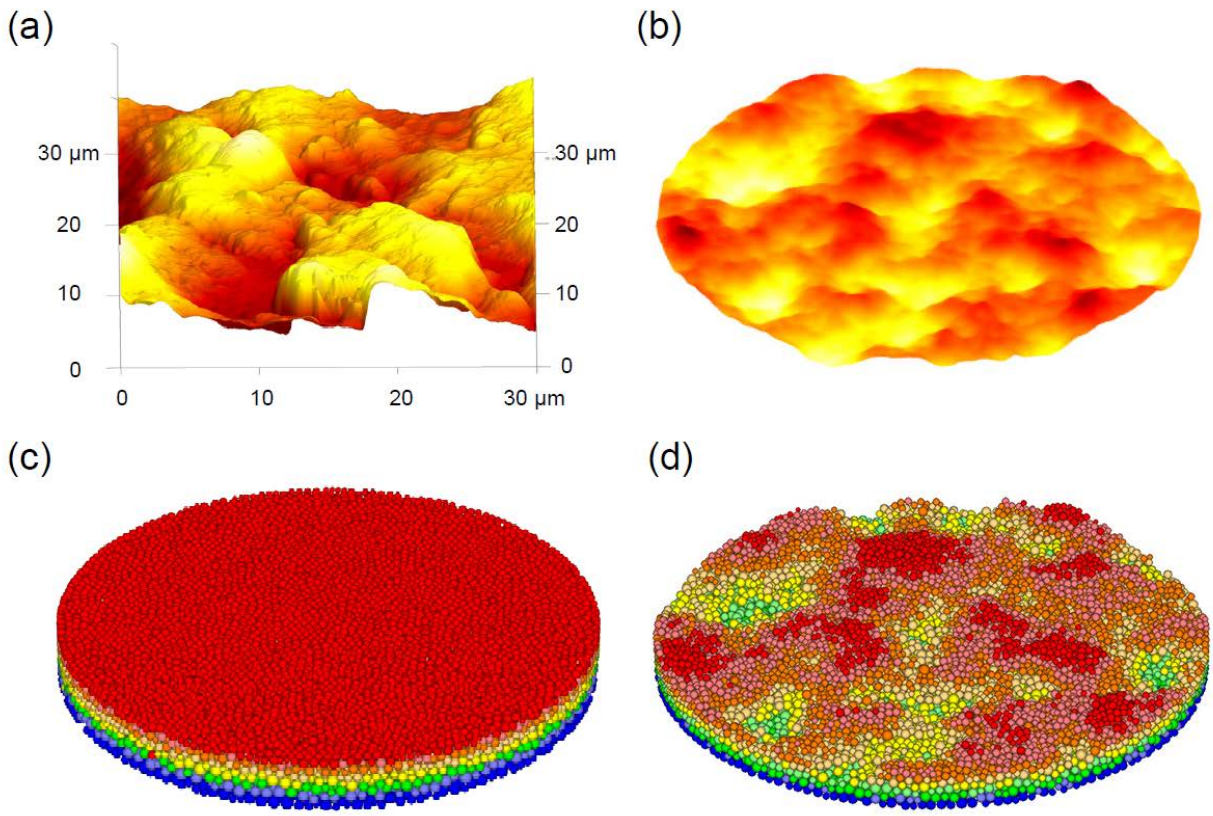

Figure 5.5. Procedures of a representative artificial DEM surface generation: (a) AFM scan of the grain surface, (b) randomly generated surface to mimic the true surface, (c) high-resolution contact disc, and (d) carved surface of the contact disc (Test E, RMS = 621 nm).

When the height profiles are given by a discrete function $h_{x,y}$ on 2D surface with lateral lengths L_x and L_y, 2D PSD is defined as the squared amplitude of the forward Fourier Transform (Jacobs et al., 2017, Nayak, 1971, Persson et al., 2005) as shown in the floowing

$$C^{2D}_{q_x,q_y} = A^{-1}\left|\tilde{h}_{q_x,q_y}\right|^2 \tag{5.4}$$

where A is in-plane surface area ($A = L_xL_y$), and $\tilde{h}_{q_x,q_y}$ is the forward discrete Fourier transform of the surface topography $h_{x,y}$ calculated by the following process

$$\tilde{h}_{q_x,q_y} = l_x l_y \sum_{x,y} h_{x,y} e^{-i(q_x x + q_y y)} \tag{5.5}$$

where q_x and q_y are wavevectors (spatial frequency), l_x and l_y are the pixel sizes of a rectangular grid along with *x*- and *y*-directions, respectively. When the number of points in the *x*- and *y*-directions are *m* and *n*, $l_x = L_x / m$ and $l_y = L_y / n$. As the wavevectors are able to span the rough surface, there will always be lower and upper limits of the wavevectors constrained by the surface; the smallest wavevector (largest wavelength) would be $2\pi / L_x$ and $2\pi / L_y$, whereas the largest wavevector is $2\pi / l_x$ and $2\pi / l_y$. The summation takes all lattice sites within these limits. If the rough surface is isotropic that is axially symmetry, the wavevectors in Cartesian coordinates (q_x, q_y) are converted to polar coordinates (0, θ), leading to the independent C_q of the direction of q.

Fig. 5.6(a) presents PSD curves of the real grains used in the grain-scale laboratory tests. Based on the PSD analysis of the real sand grain surfaces obtained from the surface elevation profiles by AFM, artificial continuum surfaces were numerically constructed using the knowledge of PSD. As the PSD of real sand grain surfaces explicitly shows characteristics of self-affine and role-off wavevector in Fig. 5.6(a), the power-spectrum of the virtual surfaces mimicking the real surfaces is assumed to be the idealized power function associated with self-affine surface in Eq. (4.9). The PSD of the real sand grain surfaces shows that the corresponding *H* and q_r are 0.8 and 0.5 μm^{-1}. These values were used to approximate PSD curves of the virtual surfaces. Then, the unknown coefficient C_0 was estimated by using the energy conservation (Parseval's theorem) that the RMS roughness is the same as the shaded region in Fig. 4.1 of the PSD curve.

$$\mathrm{RMS}^2 = \frac{1}{A}\sum_{1}^{n}\sum_{1}^{m}\left|C(q)\right| \tag{5.6}$$

The RMS for real and virtual rough surfaces come to the same by means of Eq. (5.6). Once the generation of PSD has been completed for the virtual surfaces, we can then do reverse operation of Eq. (5.4)

$$\left|\tilde{h}_{q_x,q_y}\right| = \sqrt{C^{2D}_{q_x,q_y} A} \tag{5.7}$$

Because the above equation only retains amplitude of wavevectors, the phase component was randomly chosen from the range [0 2π], thereby $\left|\tilde{h}_{q_x,q_y}\right|$ became $\tilde{h}_{q_x,q_y}$ with the phase

information. Finally, elevation profiles $h_{x,y}$ of the virtual surface can be calculated by the inverse discrete Fourier transforms in the plane.

$$h_{x,y} = \frac{1}{L_x L_y} \sum_{q_x, q_y} \tilde{h}_{q_x, q_y} e^{i(q_x x + q_y y)} \tag{5.8}$$

This random surface generation technique using PSD was previously used by Kanafi and Tuononen (2017).

To validate the generated surfaces, additional surface characterization technique, Bearing Area Curve (BAC), was considered. The comparisons of the BAC between the real sand grain surface and the one of the virtual surface are shown in Fig. 5.6(b). Overall, the comparisons of BAC results show good agreement between the real and virtual rough surfaces. As the complete characterization of the roughness properties shows satisfactory correlation, a generated surface is expected to behave like the real one.

The initial thickness of the DEM cylinder is 6 μm, and this thickness is still reduced by carving. As the nominal contact DEM assembly has a finite thickness varying from 3 to 6 μm, some creep of the cylindrical assembly might generate minute convergence, in addition to the convergence from asperity fracturing at the contact surface. This inaccuracy is minimized by making the DEM cylinder very thin. During the carving process, the cylindrical DEM assembly was carved by deleting all sub-particles outside of the target continuum surface geometry. As a result, the nominal contact DEM assembly with rich asperities can be developed as was shown in Fig. 5.5(d). One can clearly identify the similarity between Figs. 5.4(b) and (d). Although the AFM result in Fig. 5.4(a) has different appearance, it has similar quantitative characteristics. Because the radius of the nominal contact area is far smaller than the grain radius, the influence of the grain shape (curvature) on the nominal contact area is not considered in this study.

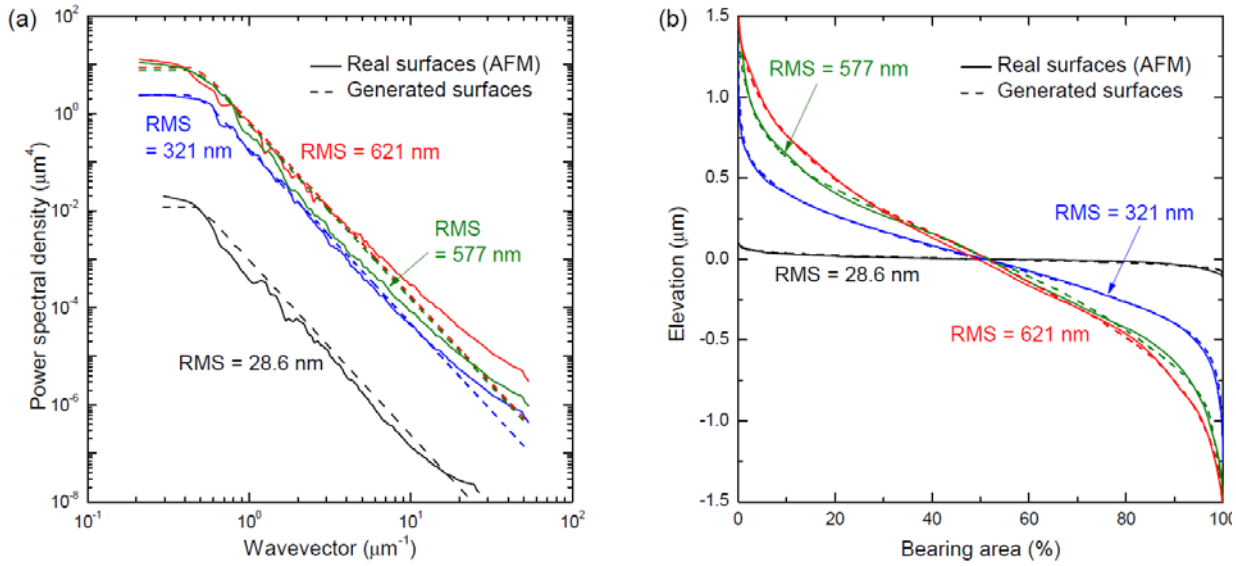

Figure 5.6. Comparison of surface analysis measures between the real sand grain surface and virtually generated surfaces; (a) power spectral density (PSD), and (b) bearing area curve (BAC).

5.5.2. Nominal contact DEM simulation and total convergence results

The nominal contact DEM accounts for the time-dependent micro-fracturing of contact asperities on the contact area, and calculates the corresponding convergence. Making use of the boundary conditions determined in the single-grain FEM, the generated nominal contact surface has the radius of a, and it is confined by the $\sigma_{\theta\theta}$. The top of the asperities on the nominal contact DEM are loaded by the steel plate with the stress σ_{rr}.

While the calibrated PSC model parameters from the half-grain DEM results were employed for long-term simulation, the tensile and shear strengths of bonds ($\bar{\sigma}_c$ and $\bar{\tau}_c$) between sub-particles were chosen such so that experimental convergence curves were matched. The inter-particle bonding strengths used in the half-grain DEM, $\bar{\sigma}_c = \bar{\tau}_c$ = 750 MPa, seem unreasonable to the nominal contact due to different length scales. When large vertical and confining stresses (σ_{rr} and $\sigma_{\theta\theta}$) estimated from the single-grain FEM were used in the nominal contact DEM assembly formed with bonding strengths identical to those of the half-grain DEM, the nominal contact DEM assembly immediately collapsed. This is because the values of tensile and shear strengths of parallel bonds in BPM are dependent on the length-scale of geo-materials. For example, the bond

strengths of the rock sample represented by a dense packing aggregates of particles are in the general range between 20 MPa and 175 MPa (Potyondy and Cundall, 2004, Potyondy, 2007, Bahaaddini et al., 2013, Bahaaddini et al., 2016, Schöpfer et al., 2009, Park and Song, 2009, Zhang and Wong, 2013, Asadi et al., 2012). In these studies, the sizes of rock samples used in the simulations are between 20 and 152 mm. On the other hand, bonding strengths between sub-particles building up a single sand grain have much higher strength than those of rocks, with a range of 450 ~ 750 MPa, even as large as 2 GPa (Cil and Alshibli, 2012, Cil and Alshibli, 2014, Fu et al., 2017, Sun et al., 2018, Wang et al., 2015, Wang and Michalowski, 2015). The size of the sand grains used in the abovementioned studies are from 0.16 to 1.6 mm. These ranges of cement strengths for rocks and sand grains are the result of calibration by correlating the fracturing behaviors in both the laboratory and field tests. There are several plausible reasons for the discrepancy. First of all, rock samples are chemical compounds of aggregate minerals and cementation between them, whereas the sand grains are typically uniform with mostly silica, resulting in the more homogeneous material. As rocks have diverse origins with different mineralogy and geological history, they typically show a wide range of strength. Because quartz, the most common constituent of sand in geotechnical engineering applications, is one of the hardest minerals, the sand is more likely to resist fracturing compared to the rocks with heterogeneous minerals. Another reason for variation in structural strength is the size effect (Bažant, 1999). In the size effect, the large rock specimens fail at lower stresses than the small specimens do. Nakata et al. (2001) reported the experimental results showing that the smaller the sand grain the greater the particle crushing strength. These are the likely reasons why the calibrated strength of sub-particle bonds forming a sand grain is larger than that for rock specimens presented in the literature. When it comes to the sub-particle bonds building up a tiny nominal contact area (a = 25 μm at 2.4 N), larger cement (bond) strength should be expected. Only very strong cement bonding between sub-particles can endure significant stress concentrations on the true asperity contacts. Given that the bonding strengths of the BPM, $\bar{\sigma}_c$ and $\bar{\tau}_c$ are scale-dependent parameters, simulating asperity fracturing involves an estimation of the appropriate bonding strengths at the small length-scale. With the calibrated PSC model parameters, which are consequences of the half-grain DEM, the bonding strengths ($\bar{\sigma}_c$ and $\bar{\tau}_c$) were calibrated in the nominal contact DEM simulation. The calibration process was conducted by trial and error in trying to match the tests with 2.4 N of sustained loading (tests B, C and E). Note that, during the calibration, a comparison

with experimental results employs the total convergence that is the sum of the half-grain and the nominal contact DEM. Due to the complex behavior of asperity fracturing on the nominal contact area, matching all convergence curves was no easy matter. After massive computations, a satisfactory agreement of convergence from simulations and laboratory tests was reached, and the strength in the hybrid model nominal contact was estimated for $\bar{\sigma}_c$ and $\bar{\tau}_c$ both being 10 GPa.

A side and a bottom views of the nominal contact DEM assembly of test E throughout the simulation are shown in Fig. 5.7. The contact geometries, before and immediately after the load of 2.4 N was applied, is depicted in Figs. 5.7(a) and (b), respectively. Varied colors in the assembly present different heights, indicating the change of surface shape. In Fig. 5.7(b), the side view shows a much smoother profile immediately after load application, because of both elastic deformation and the immediate fracturing of bonds between sub-particles (damage). However, the bottom view still has a rich texture. In the next 25 days of sustained loading (Fig. 5.7(c)), the simulated DEM contact assembly shows smoothened topology over time, owing to bond fracturing between sub-particles. The reduced thickness in the side view results in one part of convergence (δ_{contact}, contact maturing component) among the total grain deflection. The sub-particles with red color in Fig. 5.7(c) are involved in the increased number of contact points between the simulated asperities and the loading plate.

Fig. 5.8 shows the measured and computed total convergence from laboratory tests and the hybrid model, respectively, for 2.4 N of the applied load. The computed convergence from the hybrid model plotted in the figure is the sum of the grain core creep deformation and the contact area deformation by contact maturing, obtained from half-grain DEM and nominal contact DEM. For example, the total convergence of the model result for test B is 0.192 μm at t = 25 days, and this is the sum of 0.180 μm from the half-grain DEM result and 0.012 μm from the nominal contact DEM result. The hybrid model calibrated with the experiments successfully captures the behavior of convergence measured in the grain-scale laboratory tests and precisely reproduces the decaying process of convergence over time.

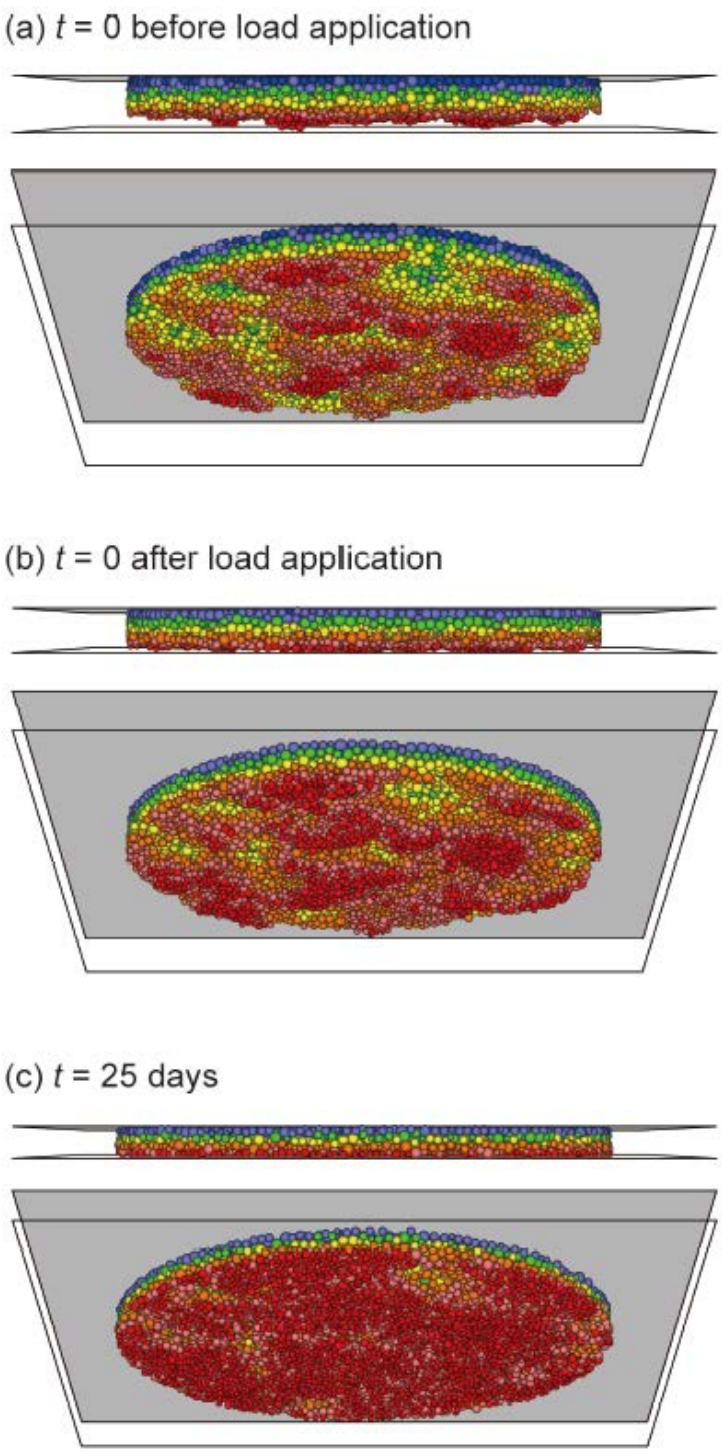

Figure 5.7. Distinct element model of the contact region simulating Test E: (a) carved surface, (b) immediately after load application, and (c) after 25-day loading with 2.4 N.

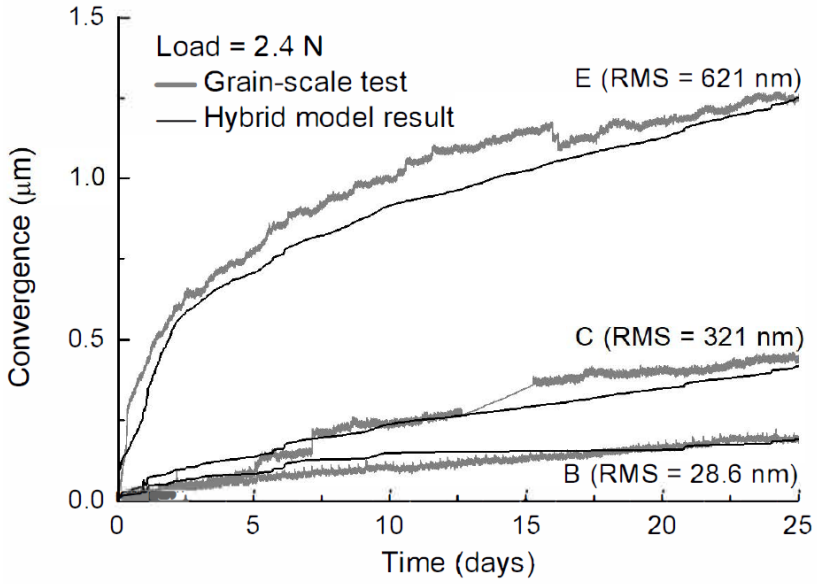

Figure 5.8. Hybrid model results and the nominal contact DEM model calibration in comparison with the grain-scale tests B, C and E (F = 2.4 N).

5.5.3. Contact maturing process on the nominal contact area

Among the three simulation results in Fig. 5.8, tests B and E were chosen to study the influence of contact maturing process in detail. Given that the grain used in test B has smooth surfaces with the low RMS, nearly the entire convergence in test B would be the result of creep in the grain core material. The convergence in test E, however, is likely to have a substantial component of contact maturing because of the relatively large roughness. Considering the major difference in the initial surface roughness of grains (RMS) in tests B and E, it is reasonable to expect that the time-dependent fracturing behaviors of the surface asperities on the contact area will be different. It is very likely that a rough surface with a rich texture is more susceptible to asperity fracturing due to stress concentrations on contact asperities, resulting in larger convergence. To justify this conjecture, contact points, force chains, and bonding breakages in simulations of tests B and E were tracked over time elapsing up to 25 days. Figs. 5.9(a) and (b) present contact points between the nominal contact surface and a steel plate for tests B and E, respectively. The outermost black circle indicates the nominal contact area and the contact points at the elapsed time t = 0 and 25 days are plotted together using bubbles. The bubble size in Fig. 5.9 is proportional to the magnitude of

the contact force at that contact point. Because the applied force is constant (2.4 N) throughout the tests, the total areas of red and blue bubbles are identical.

When the nominal contact surface coming into contact with a steel plate has a relatively smooth surface (Fig. 5.9(a)), the contact points before and after constant loading are many and uniformly distributed. As the applied force is well supported by a number of contact asperities initially, the time-dependent micro-fracturing of contact asperities is not intense. The overlaps of the contact points at $t = 0$ and 25 days indicate that the contact of a smooth surface forms a stable structure, resulting in a small number of fractures (leading to small convergence). On the other hand, the substantial force concentrations are observed initially on the contact asperities in the rough nominal contact area (Fig. 5.9(b)). Because the initial asperity contacts occur at the small areas on the nominal contact, the stresses acting on these areas asperities are large, while elsewhere the nominal contact is stress free. Over time, contact asperities fracture, leading to redistribution of contact points and forces. This intense contact maturing process gives rise to the rapid increase in convergence during the first several days. Over time, however, new contacts become involved in the force transmission process, making the surface less susceptible to asperity fracturing. That is why the rate of the convergence (slope of the convergence curve) decreases in time to reach a low and approximately constant value after a substantial time (e.g., 25 days) as illustrated in Fig. 5.8. The most important finding is that the number of contact points on the contact area increases over time under sustained loading, due to contact maturing process. This is consistent with the static fatigue hypothesis that the increased number of asperity contacts between grains brings about stiffer and firmer grain contacts, leading to macroscopic sand ageing.

Force chains and bonding breakages between sub-particles are presented in Fig. 5.10. All contact forces between sub-particles (also referred to as force chains) and bonding breakages are shown in the figure by projecting them on the nominal contact. The force chains (Fig. 5.10 (a,b,d,e)) and bonding breakages (Fig. 5.10 (c,f)) inside the assembly are projected and plotted on the plane of nominal contact. Relatively uniformly distributed force chains and a few bonding breakages are observed for the contact with a relatively smooth grain surface (RMS = 28.6 nm), Figs. 5.10 (a), (b) and (c). Even a single stress concentration near the center (Fig. 5.10(a)) disappears over time (Fig. 5.10(b)), and it is identified by the developed bonding breakages (cracks) in Fig. 5.10(c). The contact forces between the sub-particles in the contact with low roughness are smaller than those in the contact with large roughness, causing less intense fracturing.

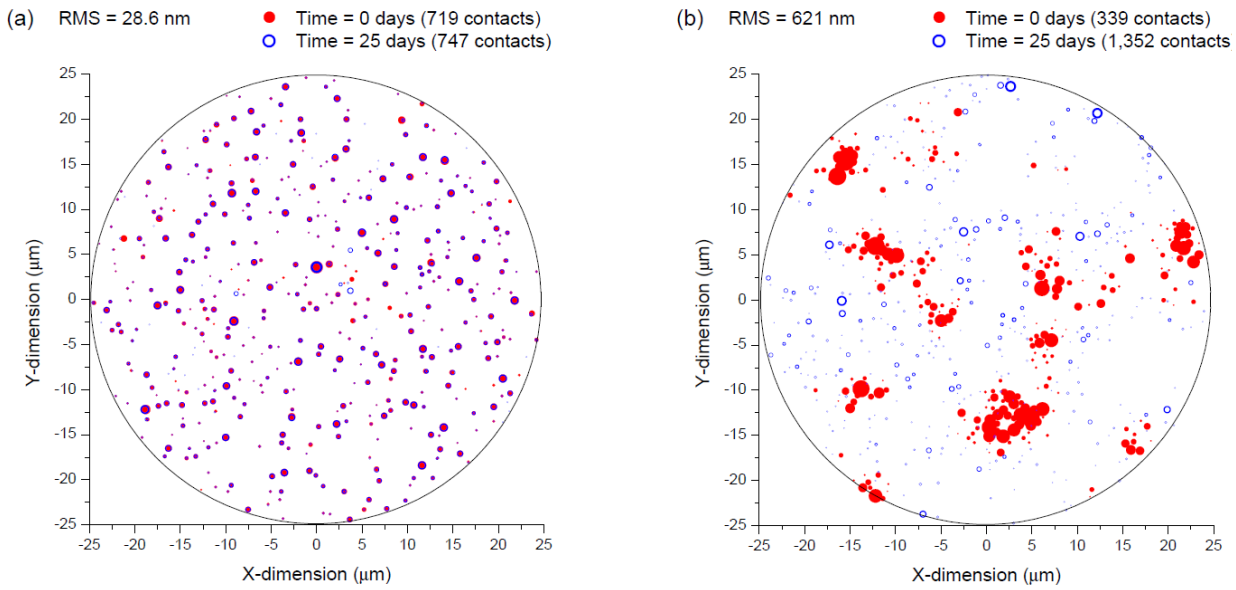

Figure 5.9. Contact points and corresponding contact forces captured in the nominal contact DEM; (a) RMS = 28.6 nm (test B) (b) RMS = 621 nm (test E).

For the rough surface in Figs. 5.10(d), (e) and (f), the force chains and micro-fractures tend to be more concentrated. Several true asperity contacts with strong force chains (Fig. 5.10(d)) at t = 0 undergo the time-dependent fracturing (Fig. 5.10(f)) so that a more uniform force chains distribution is achieved at t = 25 days (Fig. 5.10(e)). During the process, time-dependent fracturing of asperities gives rise to a large deformation of grain surface, and in turn, a large convergence. The locations of initial contact points and concentrated damage to asperities are consistent and can be clearly identified, particularly in the lower row of images in Fig. 5.10.

The number of spheres in the nominal contact DEM assemblies are all slightly different in simulations. In test E, the original cylindrical and carved DEM assemblies have 20,583 and 8,806 sub-particles, respectively, with the average radius of 0.36 µm. In order to identify the influence of the number of sub-particles in the nominal contact DEM, a sensitivity analysis was conducted with different resolutions. By keeping the size of the nominal contact assembly constant, the radius of spheres was varied, leading to a different total number of spheres. All other micro-properties in sub-particles and bonds were fixed. The DEM assembly with the numbers of particles ranging from 7,106 to 14,204 were tested. Fig. 5.11 represents the convergence of nominal contact DEM with different sub-particle numbers. Except for one extreme case, the convergence after 25 days appears to be almost independent of sub-particle size.

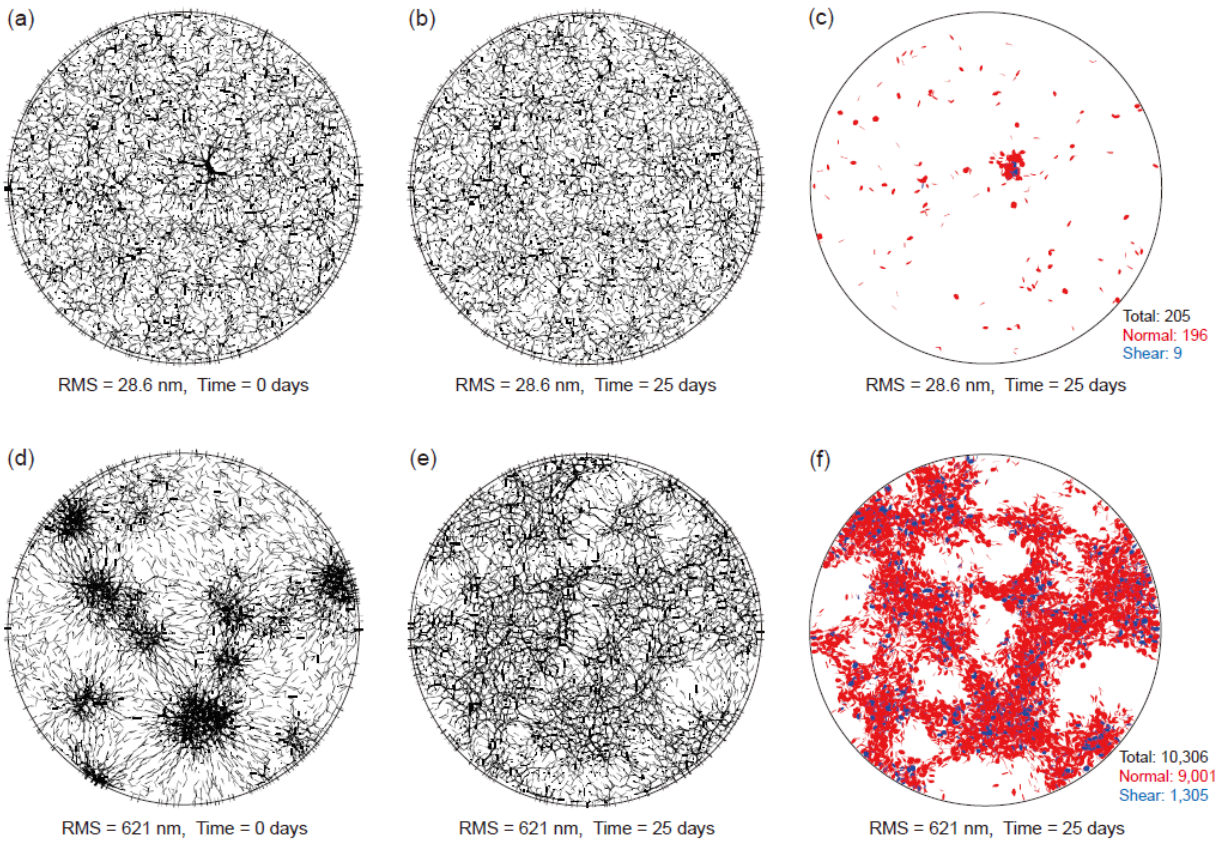

Figure 5.10. Force chains and bonding breakages between sub-particles in simulations with 2.4 N load (Total: total number of breakage, Normal: tensile breakages, Shear: shear breakages); (a) force chains at t = 0 day (RMS = 28.6 nm), (b) force chains at t = 25 days (RMS = 28.6 nm), (c) bonding breakage at t = 25 days (RMS = 28.6 nm), (d) force chains at t = 0 day (RMS = 621 nm), (e) force chains at t = 25 days (RMS = 621 nm), and (f) bonding breakage at t = 25 days (RMS = 621 nm).

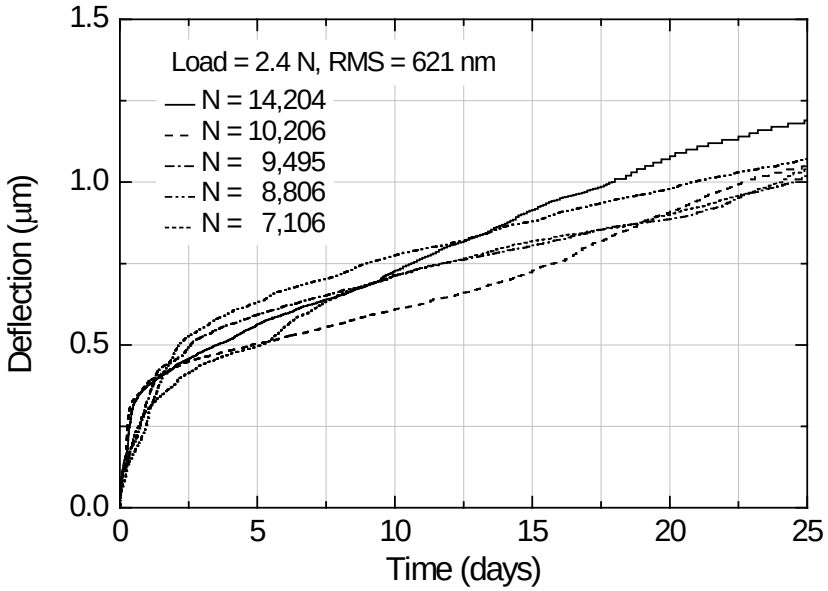

Figure 5.11. The effect of sub-particle size on convergence in the nominal contact DEM simulation.

5.6. Validation of the hybrid model

The convergence measured in the laboratory tests and calculated from the hybrid model in Fig. 5.8 match fairly well as tests B, C and E were used to calibrate the model. The model, however, needs to be applicable to grains with different roughness and loads. Therefore, the calibrated model was validated through simulations of different grain-scale laboratory tests that were not used in the calibration process. Tests A and D (load = 1.3 N) were used for the validation. Because the applied load is changed, the radius of the nominal contact area will now change, as well as the boundary conditions on the nominal contact disc (vertical and confining stresses). The boundary conditions with 1.3 N of the applied grain load are shown in Table 5.4. A new DEM assembly of the rough surface was generated for test D (RMS = 577 nm) to be used in the nominal contact simulation. For tests A and D, the surface analysis results for the measured and generated rough surfaces are presented in Fig. 5.12. The sum of the convergence obtained from the half-grain and nominal contact DEM simulations is plotted in Fig. 5.12, compared to the measured convergence from the laboratory tests. Simulations tend to overestimate the experimental outcome, but they seem to

follow the general trend well. Further validation is needed to reach a final conclusion; this was not done due to a lack of appropriate physical test results.

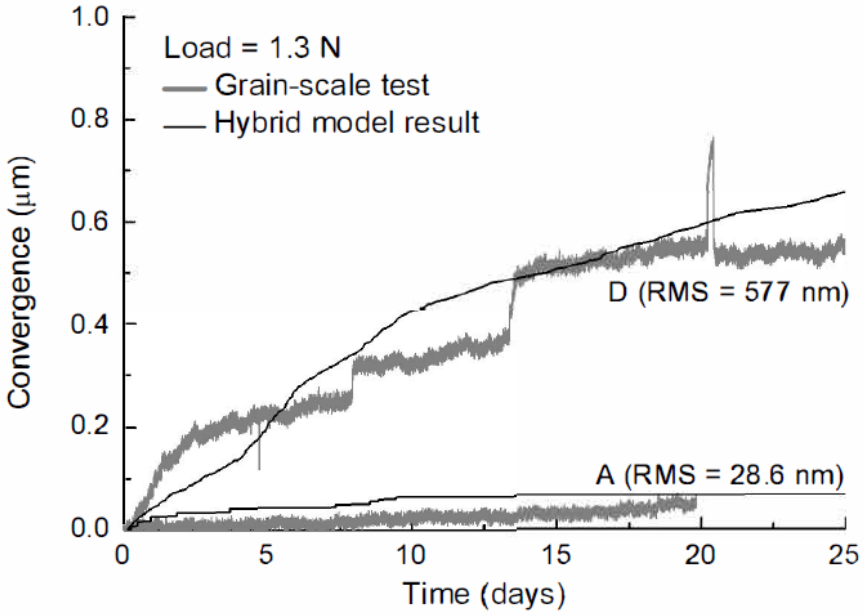

Figure 5.12. Validation of the hybrid model with the grain-scale tests A and D (F = 1.3 N).

5.7. Static fatigue behavior of a single sand grain

5.7.1. Static fatigue curve

In the nominal contact DEM, the delayed fracturing of contact asperities was modelled by the breakage of the parallel bonds in assembly of bonded sub-particles. This weakening of bonds not only cause local damage on the contact area, but also leads to the long-term split of the entire grain. In order to quantitatively characterize the time-dependent behavior of sand grain, a series of long-term numerical simulation was performed with under prolonged loading.

The spherical DEM assembly modeling a sand grain consists of 18,092 sub-particles with 13.037 μm of the mean sub-particle radius, and the radius of the entire cluster is 0.8 mm as shown in Fig. 5.13. The short-term micro-properties of BPM model and long-term PSC model parameters were taken from the calibrated hybrid model in Tables 5.1 and 5.2, respectively. Prior to

undertaking the static fatigue numerical tests, a short-term single grain crushing simulation was conducted to determine the short-term strength of the grain (σ_f). The numerical modeling for grain crushing was carried out by placing the sand grain between the top and bottom plates. For short term tests, the plates are moving at constant rate and compressing the grain between them until the sand grain completely splits. For static fatigue tests (long-term) tests, the numerical servo-mechanism, controlling velocities of the loading plates, is used to maintain constant loading.

The simulation results of short-term grain split showed that the strength of 0.8 mm diameter grain is about 140 MPa with small variation. The effects of total sub-particle number and random ball generation seed are presented in Fig. 14. As the sub-particles are randomly generated from a given radius range, considering this random ball generation seed is required in DEM simulation. The stress-strain behavior in the short-term tests indicates that the stress is initially proportional to the strain, but it suddenly drops as the grain is fractured, providing no support to the applied axial force. It was found that both the number of sub-particles and random generation seed have no substantial influence on the short-term peak strength.

The estimated short-term grain strength was compared with laboratory experiments. In the literature, Nakata et al. (2001) experimentally investigated the singe grain crushing strength with different diameters of sand grains. In the laboratory test, a single sand grain was axially loaded by moving plates at a constant velocity. A peak force associated with a major split of the sand grain was denoted as the crushing strength of the sand grain. From the tests, the relationships between the crushing strength (σ_f) and initial grain diameter (d_0) were plotted as shown in Fig. 5.15. Despite of the scatter, the crushing strength appears to be inversely proportional to the diameter on a log-log scale. The short-term crushing strength of the grain computed from the DEM simulation in this study is also plotted in the chart. It is higher than that from laboratory testing, but located in the general range reported by Nakata et al. (2001).

With the short-term grain strength, and the long-term grain split simulations were performed under prolonged loading. Then, the static fatigue curve for a single grain was generated by plotting the logarithmic time-to-failure versus the driving stress ratio (σ/σ_f) as shown in Fig. 5.16. As expected, the time-to-failure is inversely dependent on the sustained load on the grain. The larger the applied force, the shorter the time to failure. When the grain is subjected to the load equal to the characteristic particle strength σ_f (driving stress ratio = 1), the grain was fractured immediately ($t_f = 0$). On the other hand, these is a stress threshold below which no further damage

occurs, and the grain does not split. This lower limit of time-to-failure is known as static fatigue limit. In the case of d = 0.8, the static fatigue limit of sand grain is 0.14. The solid line in Fig. 5.16 is the static fatigue curve of cylindrical rock samples suggested by Potyondy (2007). In his study, the long-term simulation model of rock was calibrated with laboratory static fatigue data for Lac du Bonnet granite. In comparison with rock samples, the sand grain shows smaller driving stress ratio at least one order of magnitude. It means that, for sand grain, the static fatigue proceeds with a relatively lower stress and it takes shorter time to failure. A possible explanation for this might be that a spherical shape of sand grain is likely to have stress concentrations absent in cylindrical rock specimens. Due to the flat circular loading surfaces on top and bottom of cylindrical rock specimen, the applied force is well distributed on the area. In the case of sand grain, the highly stressed area in the vicinity of contacts is susceptible to the static fatigue. The static fatigue limit for rock sample is 0.48, which is far higher than that of sand grain.

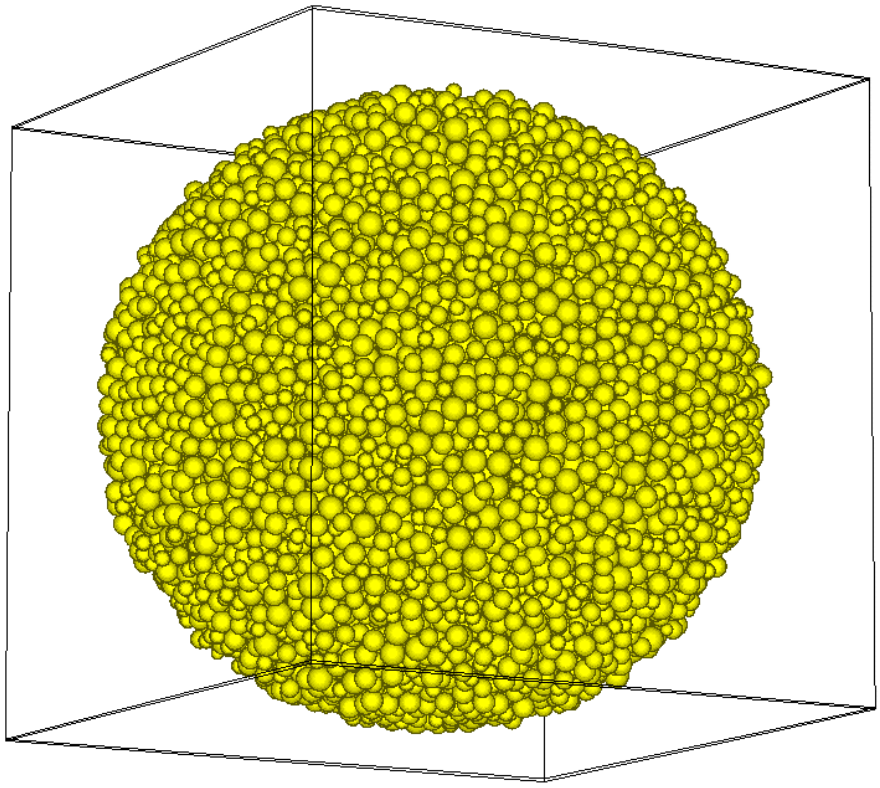

Figure 5.13. DEM model of a spherical sand grain with radius 0.8 mm, 18,092 sub-particles in total.

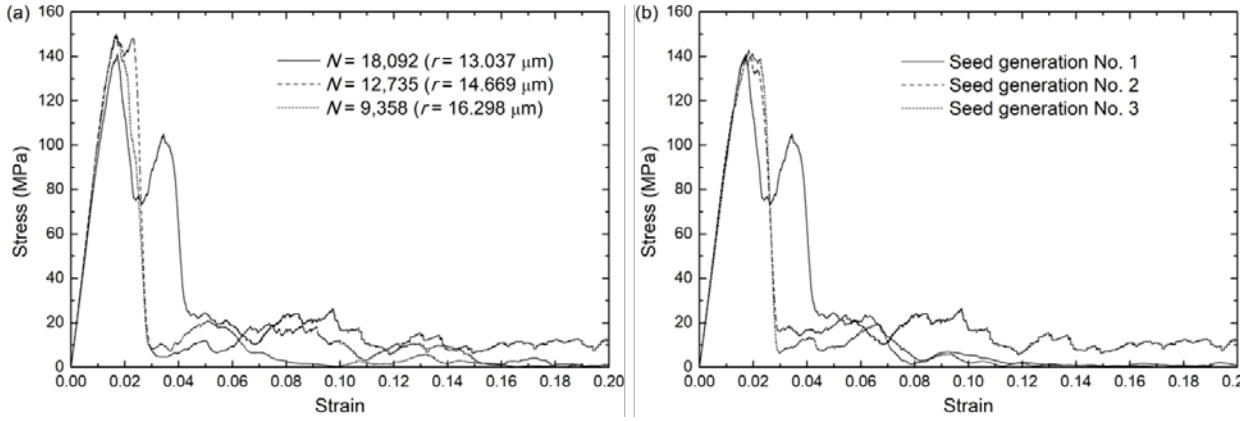

Figure 5.14. Stress-strain relationship of single grain crushing simulation: (a) effect of the number of sub-particles, and (b) effect of varying the seed of the ball generation on simulation results.

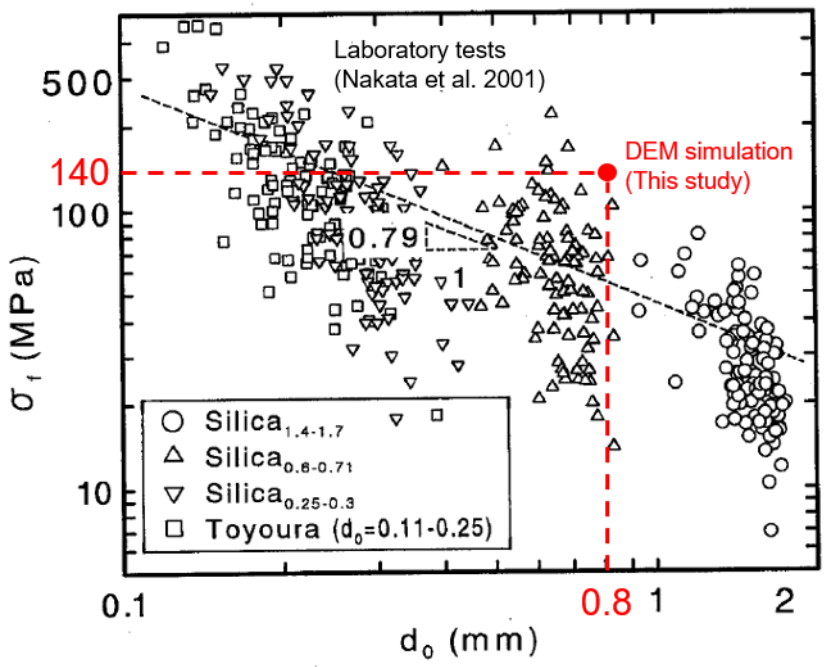

Figure 5.15. Single particle crushing strength (laboratory crushing test data from Nakata et al. 2001).

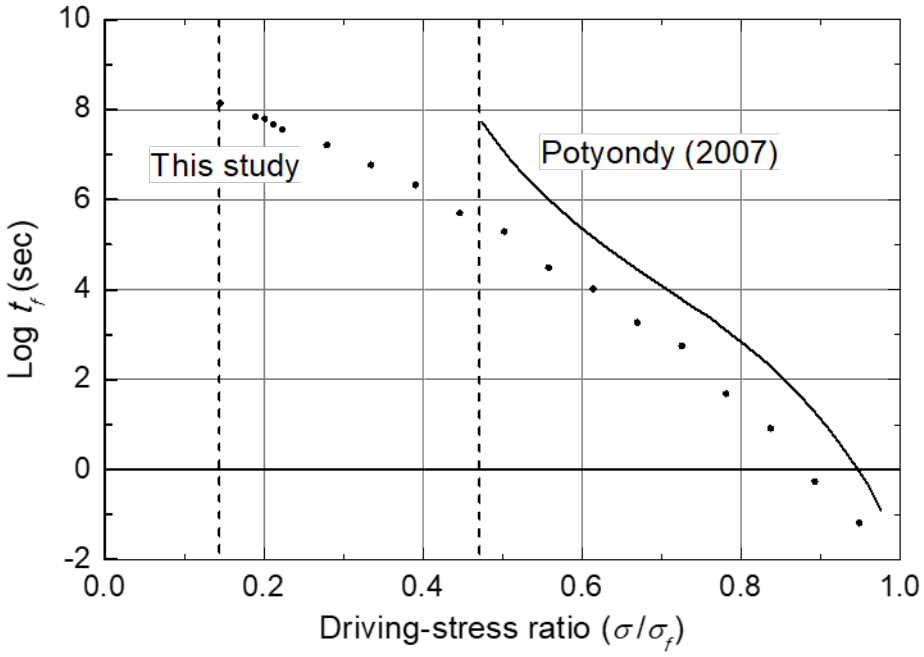

Figure 5.16. Static fatigue simulation data for spherical sand grain (this study) and rock specimen (Potyondy, 2007).

5.7.2. Grain splitting

Fig. 5.17 shows the splitting process in short-term and long-term loading. In the case of the instant grain split in Fig. 5.17(a), the grain is complete fractured immediately after the grain crushing strength. The sustained load for grain splitting caused by the static fatigue in Fig. 5.17(b) is smaller, yet it is larger than the static fatigue limit for the delayed damage. As shown in the figure, the dominant mechanism of the short-term grain split is progressive crushing and comminution near the loading areas. The tensile and shear cracks initiated in the contact region where the stress is concentrated. In this crushed zone near the contact, some fragments were generated. The top and bottom cracks soon coalesce at the center of grain, leading to the grain fracturing.

On the other hand, the failure mode of the long-term grain split indicates that the cracks are formed along with diametral fracture plane. When the vertical compressive forces are acting on the spherical body, the radial stresses σ_{rr} (in cylindrical coordinate system), perpendicular to the diametrical force direction, is tensile, causing the tensile cracks parallel to the loading direction. Because the applied stress is not large enough to cause extensive fracturing near the contact area, relatively small amount of cracks is observed in the loading sites. Instead, the time-dependent

damage is accumulated in the diametral path where the maximum tensile stress appears. After some time, the grain shows the catastrophic split along with the damaged path. The products of the grain split induced by the long-term compressive loading were generally two main parts with some fragments. The corresponding strains average strains at the complete grain spilt for short- and long-term loading are 1.8% and 5%, respectively.

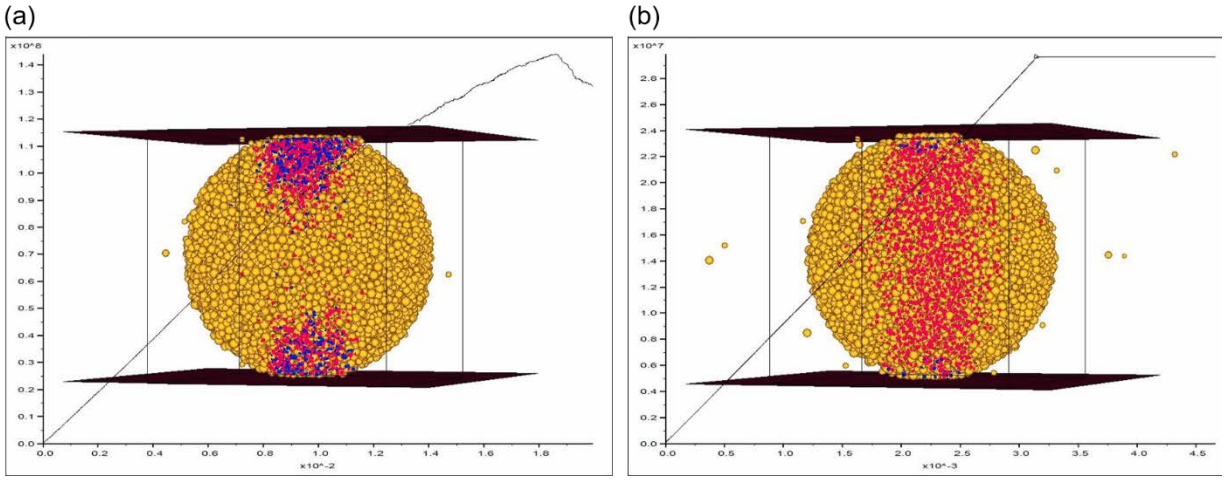

Figure 5.17. Failure mode and corresponding bonding breakages under diametral loading (red – parallel-bond tensile crack, blue – parallel-bond shear crack): (a) short-term grain split due to instant displacement loading, and (b) long-term grain split by static fatigue under sustained loading.

5.8. Summary

The results of the grain-scale laboratory experiments show a strong dependency on the initial surface roughness, indicating that contact maturing plays an important role in grain deflection. In addition, creep of the grain core material takes place simultaneously. The total convergence is the sum of the two. The hybrid model calibrated with the laboratory tests reproduces the behaviors of the time-dependent fracturing of the grain core material as well as contact asperities. The convergence results of the hybrid model show a decaying behavior consistent with the laboratory measurements, by taking into account the different sources of convergence: creep and contact maturing.

In the simulations, the time-dependent micro-fracturing of morphological features on the contact region is demonstrated under constant loading. Because of contact maturing, the number of contact points increases in time. As a result, contact forces become progressively more uniformly distributed on the entire nominal contact area. During the process, newly developed contacts participate in the force transmission, making the nominal contact area less susceptible to asperity fracturing. It is believed that the time effects in sand are initiated by contact maturing and governed by subsequent stronger and stiffer grain-to-grain contacts.

Based on the knowledge gained from the hybrid model, static fatigue curve for single sand grain was suggested. Short-term grain crushing strength is comparable to the value obtained from the laboratory testing. In terms of the grain split mechanism, different failure modes were observed in short- and long-term simulation of sand grain. While the cracks initiated in the vicinity of contacts produced fine fragments in short-term tests, long-term loading simulations indicate that the tensile cracks occur at the center first, and propagate along with the loading axis up and down.

In summary, a numerical strategy was devised to reasonably estimate the time-dependent grain convergence under sustained loading with a reasonable amount of computational effort. The simulation results confirm the contact maturing process over time, and provide additional support for static fatigue hypothesis. The hybrid model can be used in predicting very long-term behavior, which is not practical in laboratory tests. In the context of numerical modeling for contact maturing, this study is a step toward enhancing understanding of time effects in sand. Further work needs to be carried out to investigate rough intergranular contacts and bridge the gap between microscopic contact maturing and macroscopic sand ageing.

5.9. Appendix

Hiramatsu and Oka (1966) originally suggested analytical solutions for the internal stress fields under conjugate vertical compressive forces applied to an elastic sphere. As the original paper included some typos, it was corrected later. The corrected forms of σ_{rr} (Hiramatsu and Oka, 1967) and $\sigma_{\theta\theta}$ (Oka and Majima, 1970) can be found in Pejchal et al. (2017) as following

$$\sigma_{rr} = -\frac{F}{2\pi R^2}\left\{1+\frac{1}{1-\cos\alpha}\sum_{i=1}^{\infty}\frac{2(1+\nu)(1-2\nu)(4i+1)\left[\cos\alpha\cdot P_{2i}(\cos\alpha)-P_{2i-1}(\cos\alpha)\right]}{(8i^2+8i+3)2\nu+(8i^2+4i+2)(1-2\nu)}\right.$$
$$\cdot\left[\frac{(4i^2-2i-3)\nu}{(1+\nu)(1-2\nu)}\left(\frac{r}{R}\right)^{2i}+\frac{(2i+1)(2i-2)}{2(1+\nu)}\left(\frac{r}{R}\right)^{2i}-\frac{4i^2(2i+2)\nu}{(2i+1)(1+\nu)(1-2\nu)}\left(\frac{r}{R}\right)^{2i-2}\right. \quad \text{(A5.1)}$$
$$\left.\left.-\frac{2i(4i^2+4i-1)}{2(2i+1)(1+\nu)}\left(\frac{r}{R}\right)^{2i-2}\cdot P_{2i}(\cos\theta)\right]\right\}$$

$$\sigma_{\theta\theta} = -\frac{F}{2\pi R^2}\left\{1+\sum_{i=1}^{\infty}\left[\frac{-(4i+1)(i-1)+(4i+1)^2\nu}{2i(4i^2+2i+1)+2i(4i+1)\nu}\left(\frac{r}{R}\right)^{2i}\right.\right.$$
$$\left.+\frac{(4i+1)(4i^2+4i-1)+2(4i+1)\nu}{2(4i^2-1)(4i^2+2i+1)+2(4i+1)(4i^2-1)\nu}\left(\frac{r}{R}\right)^{2i-2}\right]\cdot(1+\cos\alpha)\cdot P'_{2i}(\cos\alpha)\cdot P_{2i}(\cos\theta)$$
$$+\sum_{i=1}^{\infty}\left[\frac{-(4i+1)(2i+5)+4(4i+1)\nu}{4i(2i+1)(4i^2+2i+1)+4i(2i+1)(4i+1)\nu}\left(\frac{r}{R}\right)^{2i}\right. \quad \text{(A5.2)}$$
$$\left.\left.+\frac{(4i+1)(4i^2+4i-1)+2(4i+1)\nu}{4i(4i^2-1)(4i^2+2i+1)+4i(4i+1)(4i^2-1)\nu}\left(\frac{r}{R}\right)^{2i-2}\right]\cdot(1+\cos\alpha)\cdot P'_{2i}(\cos\alpha)\cdot\frac{\partial^2 P_{2i}(\cos\theta)}{\partial\theta^2}\right\}$$

with

$$\alpha = \arcsin\left(\frac{a}{R}\right) \quad \text{(A5.3)}$$

where ν is the Poisson ratio, a is the contact area, and $P_{2i}(\cos\theta)$ is the Legendre polynomial of degree $2i$.

$$P_n(x) = \frac{1}{2^n n!}\frac{d^n}{dx^n}(x^2-1)^n \quad \text{(A5.4)}$$

Note that $P'_{2i}(\cos\alpha)$ in Eqs. (A5.1) and (A5.2) is the first partial derivative with respect to $\cos\alpha$. Because the Eqs. (A5.1) and (A5.2) have the form of an infinite series, they were truncated by 1000 summation terms.

Chapter 6

Discrete Asperity Modeling of Contacts

6.1. Introduction

The results based on the microscopic observation, laboratory tests (Chapter 4) and hybrid model (Chapter 5) suggest that the time-dependent surface maturing indicates that the major contributor of the time effect in sand is contact maturing, resulting in increasing number of contact points. However, the mechanism responsible for the time effect is not understood. In this study, the influence of contact maturing on the key contact properties, such as contact normal and shear stiffnesses, and frictional strength, is studied using a new model developed in this chapter.

A mechanical approach is formulated using elementary potential solutions in elastic half-space. The main idea is a discretization of the nominal contact surface to the individual asperity level. This approach is adopted because the real contact surfaces are complex, and understanding the mechanism of contacts is difficult. Therefore, the modeling of a contact region with rich textures and asperities needs to be discretized and idealized while maintaining the essential aspects of the real contacts. To accurately formulate complex behaviors of contacts between rough surfaces under basic physics, an atomic-scale approach may be appropriate. However, the formulations associated with constitutive laws the extremely small length scale are hindered by limited computational power. Instead, a nominal contact formed by two grains coming into contact

is broken up to small sub-contact asperities; the collection of the elastic interplays among the sub-contacts at the elementary level is analogous to the mechanism of the nominal contact. To facilitate the approach, a simple mechanics, Discrete Asperity Model (hereafter, DAM), is introduced by giving special attention to the elastic interaction between asperities and time-dependent behavior of individual asperities. The DAM basically models a nominal contact area with the inclusion of a number of asperities inside, by solving the force-displacement relationship. Once characteristics of the individual asperities are specified, the overall behavior of the nominal contact area can be found from the interaction between the asperities.

In this chapter, the formulation of the DAM and its applications to the contact maturing process are presented. This part begins by examining a fully-coupled DAM derivation of normal and shear components and quasi-static programming. Using the elastic contact solutions of rough surface, some comparisons are carried out to validate the developed model. The DAM simulation of contact of grains used in the grain-scale laboratory experiments is performed to model the time-dependent behaviors on the nominal contact area. Next, multi-asperity DAM simulations are carried out to demonstrate the possible mechanisms of frictional aging in rocks: (1) increased true contact area, (2) strengthened interfacial chemical bonds, and (3) increased number of contact points. This chapter concludes with some remarks and future research ideas.

6.2. Discrete asperity model (DAM)

When two grains come into contact, a contact area is developed between the two grains. True contacts occur only on small local areas within a nominal contact area, because a real grain surface is rough with rich texture. While the nominal contact area (or apparent contact area) indicates an area where two contact grains overlap, a true contact area consists of individual asperity contacts where force transmission occurs. On the formed nominal contact surface, many of the true contact asperities become loaded, while elsewhere the area is free of load. By considering the elastic interaction between these contact asperities, a DAM is formulated.

6.2.1. Coupled DAM with normal and shear forces

A schematic of the DAM is depicted in Fig. 6.1. The asperities are distributed on the surface of a grain with shear modulus *G* and Poisson's ratio *v*. The nominal contact area has a radius of *R* and consists of circular asperities with true contact radius *a*. The individual asperities are distributed on the nominal contact area by a hexagonal closed-packed pattern, which means the spacings between any neighboring asperity are all *d*. Assuming the total number of asperity contacts is *N* on the nominal contact, a single asperity is loaded not only by a loading on that contact itself (i^{th} asperity), but also by the remaining *N*-1 asperities (*e.g.* j^{th} asperity) elsewhere, as shown in Fig. 6.2. The total displacement vector $\overline{u}_i^{total}$ at the i^{th} asperity, caused by the external loads, can be calculated by superimposing displacements developed by its load and other loads, as shown in the following:

$$\overline{u}_i^{total} = \overline{u}_i^{self} + \overline{u}_i^{\text{int}} \quad (i = 1...N) \tag{6.1}$$

where $\overline{u}_i^{self}$ is the displacement vector (*x*, *y*, *z* directions) due to the force on the i^{th} asperity itself, and $\overline{u}_i^{\text{int}}$ is the displacement vector induced by other forces acting on the reamaining *N*-1 asperities (elastic interaction). Among all existing asperities on the nominal contact, only contact asperities where contact forces are developed, are considered for the interaction. The detailed interplays among the asperities can be estimated by the mechanical interactions as summarized in Contact Mechanics (Barber, 2018, Johnson and Johnson, 1987), and will be discussed later.

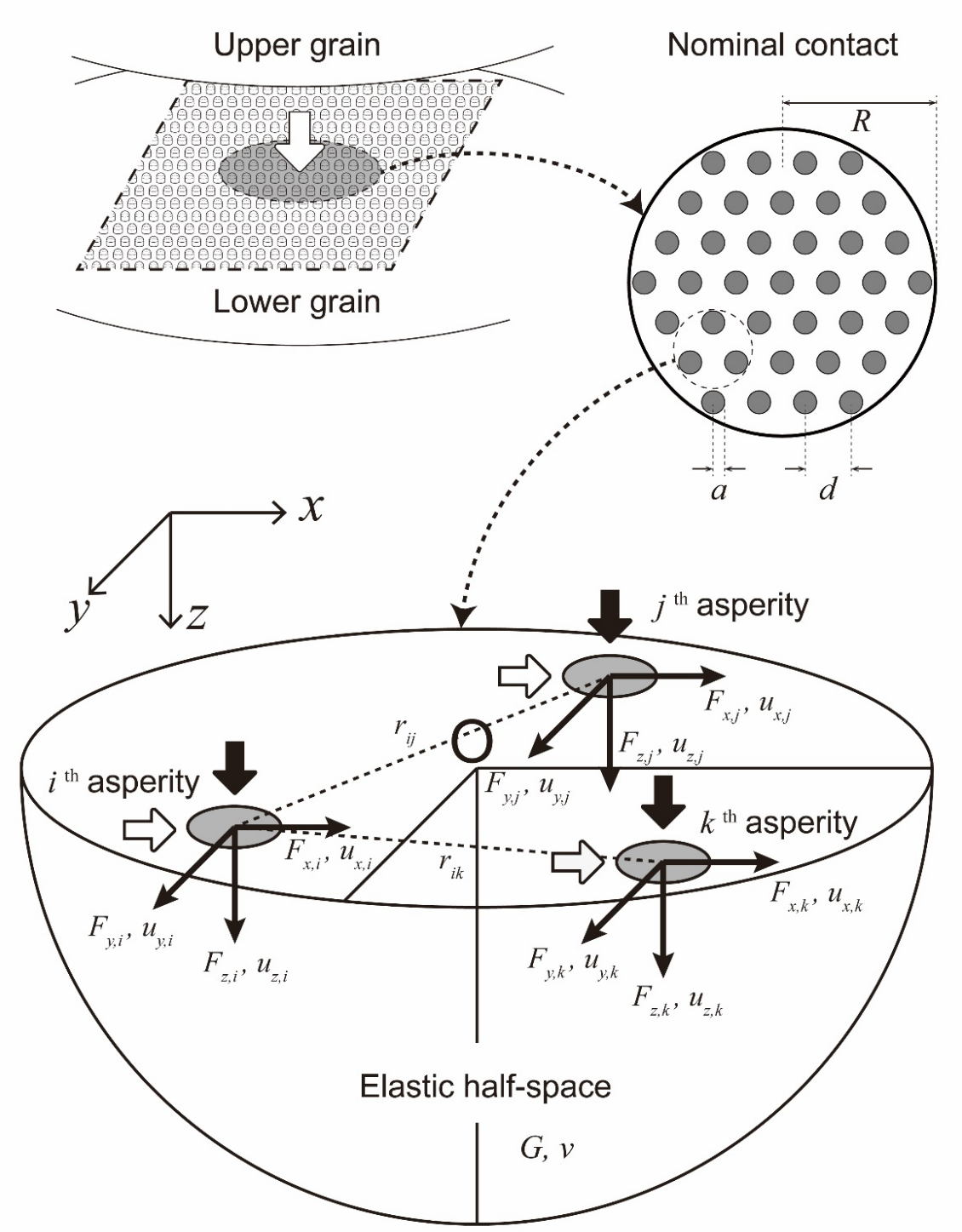

Figure 6.1. A schematic of the discrete asperity model with forces and displacements acting on the true asperity contact.

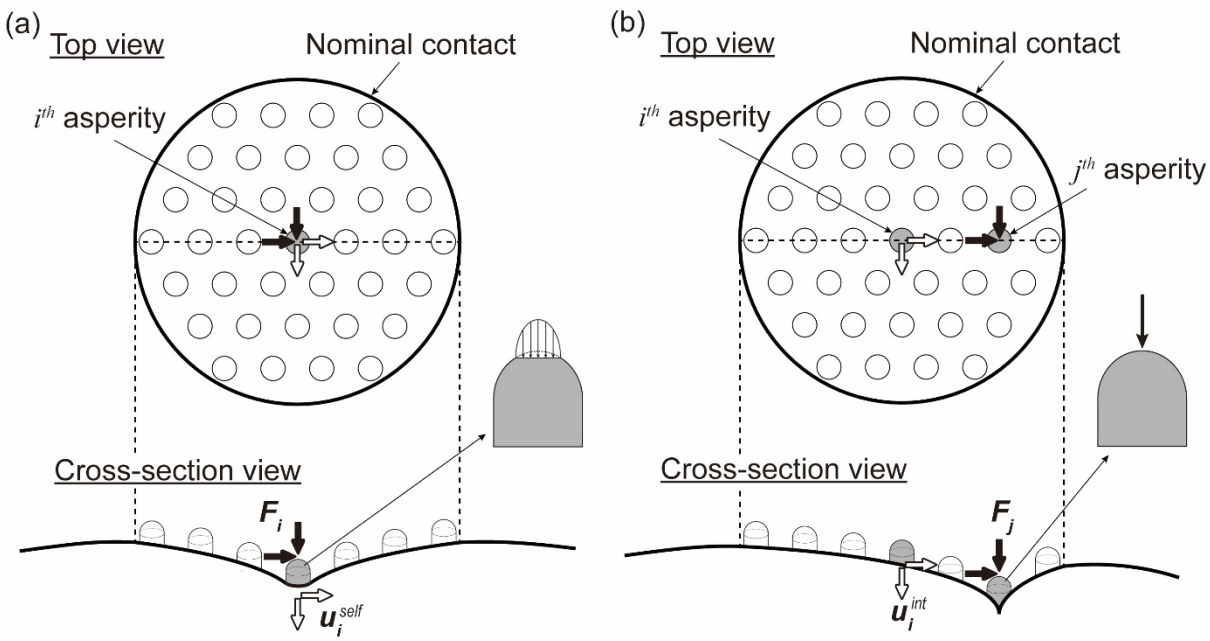

Figure 6.2. Deformed nominal contact area due to the external loads: (a) acting on the self-asperity, and (b) acting on the other (neighboring) asperity.

With regards to the loading type on a true contact asperity, a traction and a point load are applied on self-asperity and neighboring asperities, respectively. Specifically, for those on each self-asperity contact, Hertzian pressure is used assuming the spherical shape of asperity on rough surfaces. In the case of neighboring asperities, the force is considered to be a Boussinesq point loading, as this approximation is reasonable when an interacting distance between asperities is sufficiently remote. A comparison with different load types on neighboring asperities is conducted in the following section.

If a radius of self-asperity is a, a vertical displacement at the center of self-asperity u_z produced by the asperity loading F_z is (Barber, 2018)

$$u_z = \frac{3(1-\nu^2)F_z}{4Ea} \tag{6.2}$$

The displacements of x and y directions caused by horizontal forces on the self-asperity are

$$u_x = \frac{(1+\nu)(2-\nu)F_x}{4Ea}, \quad u_y = \frac{(1+\nu)(2-\nu)F_y}{4Ea} \tag{6.3}$$

The relationship between shear modulus and Young's modulus is

$$G = \frac{E}{2(1+\nu)} \tag{6.4}$$

In addition to the loads on the self-asperity itself, the asperity is also loaded by loads acting on other asperities. This asperity interaction is taken into account using the potential solutions in elastic half-space. The displacements, produced by concentrated point loads F_x, F_y, and F_z acting on the other asperities with distance r inside the nominal contact surface of the elastic half-space, can be found by Eq. (7.5) in *Contact Mechanics* (Barber, 2018).

$$\begin{aligned} u_x &= -\frac{(1-2\nu)(1+\nu)F_z x}{2\pi E r^2} + \frac{(1-\nu^2)F_x}{\pi E r} + \frac{\nu(1+\nu)x(xF_x + yF_y)}{\pi E r^3} \\ u_y &= -\frac{(1-2\nu)(1+\nu)F_z y}{2\pi E r^2} + \frac{(1-\nu^2)F_y}{\pi E r} + \frac{\nu(1+\nu)y(xF_x + yF_y)}{\pi E r^3} \\ u_z &= \frac{(1-\nu^2)F_z}{\pi E r} + \frac{(1-2\nu)(1+\nu)(xF_x + yF_y)}{\pi E r^2} \end{aligned} \tag{6.5}$$

At each asperity on the nominal contact, the total displacement can be calculated by superposing the influences over the entire nominal surface, more accurately all contact asperities. Because every force and displacement has three components (x, y, and z), the size of the compliance matrix is $3N$ by $3N$ where N is the number of contact asperities on the nominal contact area. When there are only two contact asperities (i and j asperities) on the nominal contact area, for instance, a compliance matrix can be developed with normal and tangential forces coupling as follows

$$\begin{bmatrix} A & 0 & 0 & B_{x,ij} & C_{xy,ij} & E_{x,ij} \\ 0 & A & 0 & C_{xy,ij} & B_{y,ij} & E_{y,ij} \\ 0 & 0 & D & G_{x,ij} & G_{y,ij} & H \\ B_{x,ji} & C_{xy,ji} & E_{x,ji} & A & 0 & 0 \\ C_{xy,ji} & B_{y,ji} & E_{y,ji} & 0 & A & 0 \\ G_{x,ji} & G_{y,ji} & H & 0 & 0 & D \end{bmatrix} \begin{pmatrix} F_{x,i} \\ F_{y,i} \\ F_{z,i} \\ F_{x,j} \\ F_{y,j} \\ F_{z,j} \end{pmatrix} = \begin{pmatrix} u_{x,i} \\ u_{y,i} \\ u_{z,i} \\ u_{x,j} \\ u_{y,j} \\ u_{z,j} \end{pmatrix} \tag{6.6}$$

where $r_{ij} = \sqrt{\left(x_j - x_i\right)^2 + \left(y_j - y_i\right)^2}$, $A = \dfrac{2-\nu}{8aG}$,

$B_{x,ij} = \dfrac{1}{2\pi G}\left(\dfrac{1-\nu}{r_{ij}} + \dfrac{\nu\left(x_i - x_j\right)^2}{r_{ij}^3}\right)$, $B_{y,ij} = \dfrac{1}{2\pi G}\left(\dfrac{1-\nu}{r_{ij}} + \dfrac{\nu\left(y_i - y_j\right)^2}{r_{ij}^3}\right)$, $C_{xy,ij} = \dfrac{\nu\left(x_i - x_j\right)\left(y_i - y_j\right)}{2\pi G r_{ij}^3}$,

$D = \dfrac{3(1-\nu)}{8aG}$, $E_{x,ij} = -\dfrac{(1-2\nu)\left(x_i - x_j\right)}{4\pi G r_{ij}^2}$, $E_{y,ij} = -\dfrac{(1-2\nu)\left(y_i - y_j\right)}{4\pi G r_{ij}^2}$, $G_{x,ij} = \dfrac{(1-2\nu)\left(x_i - x_j\right)}{4\pi G r_{ij}^2}$,

$G_{y,ij} = \dfrac{(1-2\nu)\left(y_i - y_j\right)}{4\pi G r_{ij}^2}$, $H = \dfrac{1-\nu}{2\pi G r_{ij}}$.

In the case of three contact asperities, it can be found by taking into account the interaction between *i*, *j*, and *k* asperities.

$$\begin{bmatrix} A & 0 & 0 & B_{x,ij} & C_{xy,ij} & E_{x,ij} & B_{x,ik} & C_{xz,ik} & E_{x,ik} \\ 0 & A & 0 & C_{xy,ij} & B_{y,ij} & E_{y,ij} & C_{xz,ik} & B_{y,ik} & E_{y,ik} \\ 0 & 0 & D & G_{x,ij} & G_{y,ij} & H_{ij} & G_{x,ik} & G_{y,ik} & H_{ik} \\ B_{x,ji} & C_{yx,ji} & E_{x,ji} & A & 0 & 0 & B_{x,jk} & C_{yz,jk} & E_{x,jk} \\ C_{yx,ji} & Bji & E_{y,ji} & 0 & A & 0 & C_{yz,jk} & B_{y,jk} & E_{y,jk} \\ G_{x,ji} & G_{y,ji} & H_{ji} & 0 & 0 & D & G_{x,jk} & G_{y,jk} & H_{jk} \\ B_{x,ki} & C_{zx,ki} & E_{x,ki} & B_{x,kj} & C_{zy,kj} & E_{x,kj} & A & 0 & 0 \\ C_{zx,ki} & B_{y,ki} & E_{y,ki} & C_{zy,kj} & B_{y,kj} & E_{y,kj} & 0 & A & 0 \\ G_{x,kj} & G_{y,ki} & H_{ki} & G_{x,kj} & G_{y,kj} & H_{kj} & 0 & 0 & D \end{bmatrix} \begin{pmatrix} F_{x,i} \\ F_{y,i} \\ F_{z,i} \\ F_{x,j} \\ F_{y,j} \\ F_{z,j} \\ F_{x,k} \\ F_{y,k} \\ F_{z,k} \end{pmatrix} = \begin{pmatrix} u_{x,i} \\ u_{y,i} \\ u_{z,i} \\ u_{x,j} \\ u_{y,j} \\ u_{z,j} \\ u_{x,k} \\ u_{y,k} \\ u_{z,k} \end{pmatrix} \tag{6.7}$$

In this way, the compliance matrix of N asperities can be easily found. When a boundary condition is given as force, displacement, or a combination of both, developed displacements and forces are calculated by solving the matrix.

6.2.2. Influence of pressure distributions applied to neighboring asperities

In the DAM simulations, all contact asperities are initially loaded by vertical force or displacement loading, and then laterally slide if necessary. To simplify the model, the external vertical loads acting on the rest of the asperities are assumed to be concentrated point loads (Boussinesq loading), whereas the one acting on the self-asperity is the Hertzian pressure. To validate the appropriateness of the assumption that the load type elsewhere is concentrated loading, a comparison with different load types applied to neighboring asperities is conducted. Compared to the point loading, the three other pressure types are considered as loads acting on neighboring asperities to identify the influence on self-asperity: 1) uniform, 2) flat punch and 3) Hertzian pressures. The basic information about the three pressure types with a concentrated force is summarized in Table 6.1. The geometric distribution of loads for the Boussinesq point loading and the three pressure types mentioned above are presented in Fig. 6.3. Note that the pressures presented as arrows apply to a single asperity having a diameter of $2a$, and the integrals (sum) of the pressures are equal to the point loading. Assuming the integrals of the pressures is a unit load for all cases ($F_{z,j} = 1$), induced displacement fields on i^{th} asperity (self-asperity) by the pressures acting on j^{th} asperity (neighboring asperity) apart from the distance r_{ij} are shown in Fig. 6.4 as a function of the normalized distance. As expected, among the three pressure distributions, the deformation at the center by the Hertz pressure gives rise to the largest value compared to the other pressures, which is consistent with Table 6.1. The point load causes an infinite displacement where the load applied. All produced displacements obtained by the different pressures are very close to the Boussinesq solution if $r/a > 3$, meaning that one can reasonably consider a load acting on other asperities as a concentrated point load. Because $d/a > 3$ for every case examined in this study, the point loading approximation for loads acting on neighboring asperities does not cause any fallacy. This idea of the point force assumption reduces a significant amount of time and effort during the derivation and computation.

Table 6.1. Summary of uniform, flat punch, and Hertz pressures.

Pressure types	Uniform pressure	Flat punch pressure	Hertz pressure
Equation	p_0	$p_0(1-\frac{r^2}{a^2})^{-\frac{1}{2}}$	$p_0(1-\frac{r^2}{a^2})^{\frac{1}{2}}$
Pressure at center (p_0)	$\frac{F_z}{\pi a^2}$	$\frac{F_z}{2\pi a^2}$	$\frac{3F_z}{2\pi a^2}$
$(u_z)_{r=0}$	$\frac{2(1-\nu^2)F_z}{\pi Ea}$	$\frac{(1-\nu^2)F_z}{2Ea}$	$\frac{3(1-\nu^2)F_z}{4Ea}$
$(u_z)_{r=a}$	$\frac{4(1-\nu^2)F_z}{\pi^2 Ea}$	$\frac{(1-\nu^2)F_z}{2Ea}$	$\frac{3(1-\nu^2)F_z}{8Ea}$

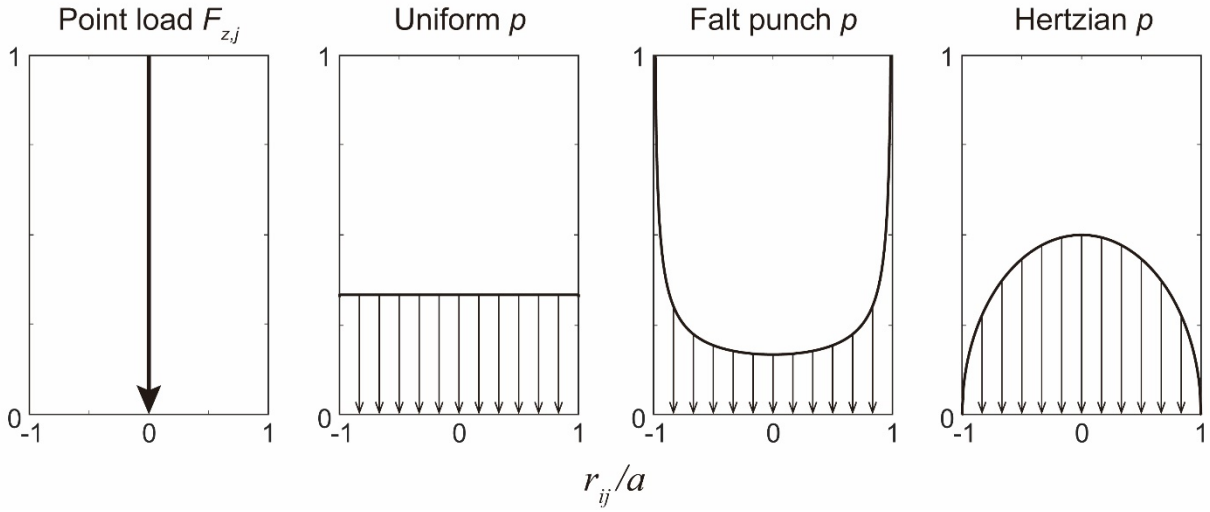

Figure 6.3. Different loading types on asperity: a concentrated point loading, uniform pressure, flat punch pressure, and Hertz pressure.

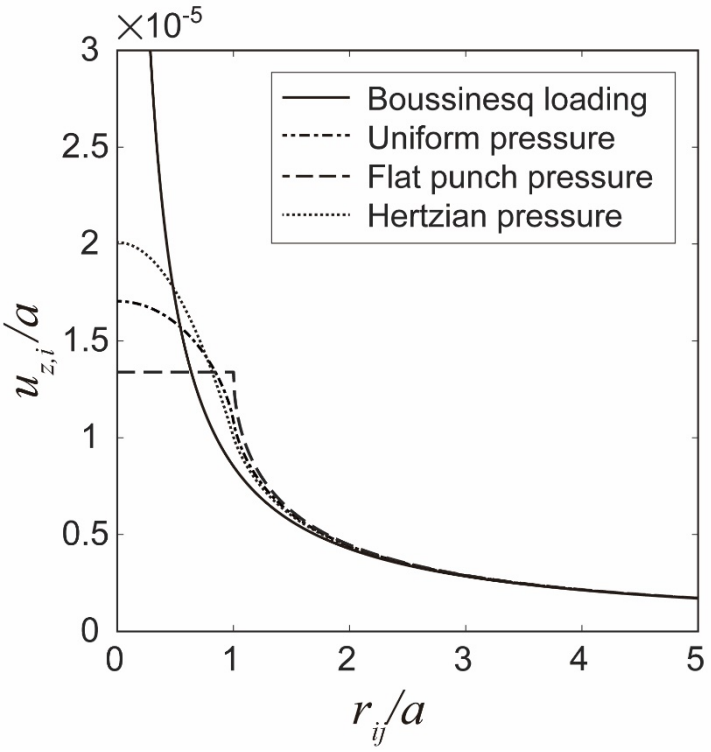

Figure 6.4. Comparison of displacements induced by the different pressure types on the self-asperity.

6.2.3. Boundary conditions and quasi-static analysis

In the DAM comprised of discrete asperities, each asperity has 3 force (F_x, F_y, F_z) and 3 displacement (u_x, u_y, u_z) components. The half of the force and displacement components should be prescribed to solve the compliance matrix. Once the forces acting on each asperity are specified, for example, developed displacements can be found by solving the compliance matrix, and vice versa.

For the frictional analysis (lateral loading), a quasi-static modeling is taken into account when dealing with the forces higher than the maximum frictional strength related to the static friction. At a single asperity contact, the frictional force-displacement relationship is illustrated in Fig. 6.5. It was found by Li et al. (2011) that the amount of ΔF is a function of hold time. Typically, F_m is higher than F_{ss}. When the asperity is stationary, the value of the frictional force on the asperity is somewhere between 0 to the maximum frictional strength F_m ($0 < F_x < F_m$). The maximum peak strength should be overcome before the asperity slides. Once a force taken by one asperity becomes

larger than its peak frictional strength, that asperity only carries the steady-state strength instead of the larger force (the asperity slips), whereby the exceeding force is diverted to the other asperities. Also, quasi-static analysis is used, meaning that the horizontal displacements are induced so slowly that inertia effects can be neglected. If one asperity takes the steady-state force beyond the peak strength, the number of unknown forces decreases (the developed horizontal force is equal to the steady-state force, and thus it is no longer unknown), in turn the size of the compliance matrix reduces. Finally, the computation will be terminated when all asperities have the same steady-state forces (sliding) by induced displacements.

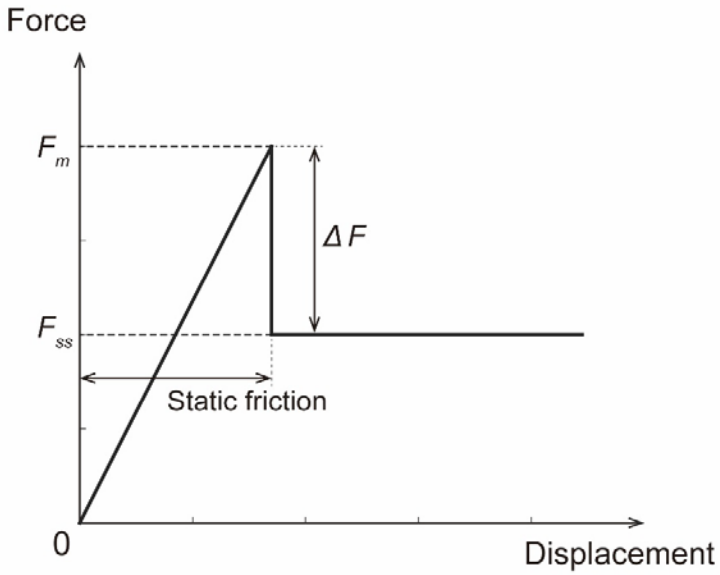

Figure 6.5. Single asperity lateral force-displacement behavior: F_m is the maximum frictional strength force and F_{ss} is the steady-state friction (kinetic friction) force, and ΔF (= F_m - F_{ss}) is the frictional drop associated with chemical strengthening of bonding.

6.3. Validation of the DAM

Before application of the DAM to the time-dependent simulation, it was compared to the solutions of rough elastic contacts in the literature. Due to the lack of long-term simulation results in the literature, two studies with instant loading condition were considered.

6.3.1. Nominal pressure

To describe a load-displacement behavior of rough surface contact, Greenwood and Williamson (1966) suggested a classical model, known as GW theory , based on statistical information of asperity height distribution. The theory basically considers contact between an elastic rough surface and a rigid plane using the probability of contact occurrence, but later it was found that the theory might also consider contact between two rough surfaces using one rough surface with all roughness of the two rough bodies contacting a plane (Greenwood and Tripp, 1970). As plotted in Fig. 6.6, the elastic rough surface consists of asperities whose shapes are perfectly spherical at the top with a asperity radius of R_a and heights are z, and the distance between the rigid plane and the mean asperity height, also referred to as separation, is d (the location of d is positioned below the mean of asperity top heights in the figure). The height distribution of the surface asperities is the Gaussian probability distribution with a standard deviation of σ. When the rigid plane gets into contact with the rough surface, a contact asperity with a height z is compressed by (z - d). As a result, from the Hertzian contact solution, a produced force at the asperity is

$$P_i = \frac{4}{3} E^* R_a^{1/2} (z-d)^{3/2} \tag{6.8}$$

Because the heights of the asperities are distributed normally, the number of contact asperities is governed by the probability of the asperity heights higher than the location of the rigid plane. By summing the produced forces of all contact asperities based on the probability, the total force on the nominal contact area induced by d is determined as

$$\sum P_i = \frac{4}{3} N_0 E^* R_a^{1/2} \sigma^{3/2} F_{3/2}\left(\frac{d}{\sigma}\right) \tag{6.9}$$

where

$$F_n(h) = \frac{1}{\sqrt{2\pi}} \int_h^\infty (s-h)^n \exp(-0.5 s^2) ds \tag{6.10}$$

Note that N_0 is not the number of contact asperities (N), but the number of total asperities on the nominal contact area. The produced nominal pressure of the nominal contact area can be found by dividing it by the nominal contact area A as shown in the following

$$p_{nom} = \frac{\sum P_i}{A} = \frac{4}{3}\eta E^* R_a^{1/2} \sigma^{3/2} F_{3/2}\left(\frac{d}{\sigma}\right) \tag{6.11}$$

where η is the density of asperity on the nominal contact area, defined by $\eta = N_0/A$. Accordingly, the non-dimensional nominal pressure becomes

$$\hat{p}_{nom} = \frac{p_{nom}}{\frac{4}{3}\eta E^* R_a^{1/2} \sigma^{3/2}} = F_{3/2}\left(\frac{d}{\sigma}\right) \tag{6.12}$$

The GW theory ignores asperity interaction with the assumption that a spacing between the contact asperities is sufficiently remote. Recently, Ciavarella et al. (2008) proposed an improved solution of the GW theory including the interaction between contact asperities as follows

$$\hat{p}_{nom} = F_{3/2}\left(\frac{d}{\sigma} + \hat{p}_{nom}\eta\sqrt{AR_a\sigma}\right) \tag{6.13}$$

In the equation, the term $\eta\sqrt{AR_a\sigma}$ is independent of the load and separation. Because the form of Eq. (6.13) is implicit, it has to be solved iteratively. In the case of 500 asperities, the solutions of Eqs. (6.12) and (6.13) are plotted in Fig. 6.7 as a function of the normalized separation d/σ. As many researchers reported that the value of $\eta R_a\sigma$ is likely to be around 0.05, the all results in the Fig. 6.7 were calculated using the value, meaning that $\eta\sqrt{AR_a\sigma} = \sqrt{N_0}\sqrt{\eta R_a\sigma} = 5$.

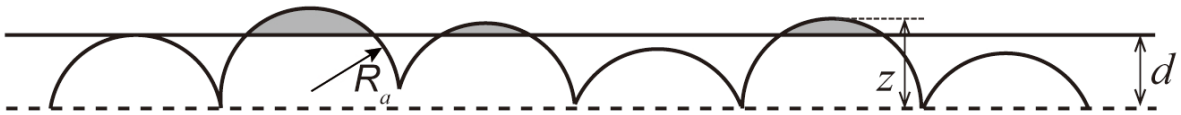

Figure 6.6. A schematic of contact between a rough surface and smooth plane. The areas with dark gray color present true asperity contacts, and the overlaps can be found as ($z - d$).

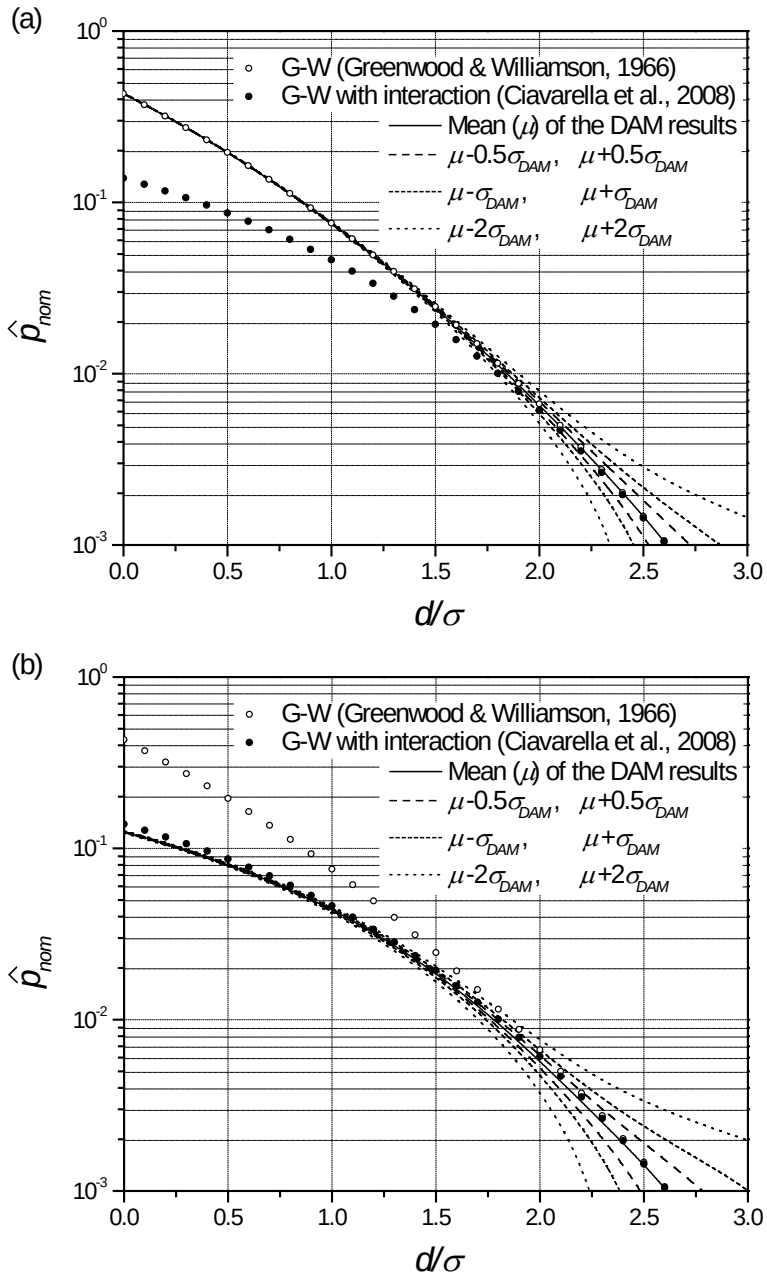

Figure 6.7. The comparisons of non-dimensional nominal pressure vs. separation curve: (a) with asperity interaction, and (b) without asperity interaction.

To validate the developed DAM, the simulations were carried out under conditions identical to those of the original and improved GW theory. On the nominal contact area of the DAM, 500 asperities were randomly generated from the Gaussian probability function with a standard deviation σ. Then, vertical displacements were increasingly applied to the rough nominal contact area, and the developed vertical forces at the individual contact asperities were measured. The sum of these contact forces is the total force on the nominal contact area. The smaller the separation (the larger the asperity deformation), the larger the total produced force. As the DAM intrinsically contains asperity interaction by its constitutive law, the results corresponds to those obtained from the improved GW theory (Eq. (6.13)). For the DAM results without asperity interaction associated with the original GW theory (Eq. (6.12)), zero was substituted for the interaction terms in the compliance matrix, B, C, E, G, H in Eqs. (6.6) and (6.7).

For each case with and without asperity interaction, 50 times of the DAM simulations were performed, and the mean and variation (standard deviation, σ_{DAM}) of the simulation results were computed. They are plotted over the scatters indicating the results of the GW theory and its improved version with asperity interaction as shown in Fig. 6.7. This many numbers of the simulations and averaging are because of a finite number of asperity in the DAM. The height profile distribution of the randomly generated asperities in the DAM is not the ideal normal distribution function. On the other hand, the GW theory employs the perfect Gaussian function for the distribution of asperity heights. This discrepancy is presented in Fig. 6.8. It is worth noting that the number of asperities in the GW theory is also a finite number (*e.g.*, $N_0 = 500$ in Fig. 6.7), but it involves the probability of contact appearance.

As can be seen in Fig. 6.7, for both with and without asperity interaction cases, the mean values of the non-dimensional nominal pressure obtained from the 50 DAM simulations reveal a good agreement with those of the corresponding GW theory solutions. The variation of DAM results is presented by the standard deviation of the results, σ_{DAM} (different from σ that is the standard deviation of asperity heights). When the separation is large (small number of asperity contacts happen), the variation of DAM results is large. This is expected acceding to the fact that the heights of the highest asperities vary a lot according to the random generation process of asperity height, as only a few asperities get into contact. When the separation is small, on the other hand, the DAM matches with the GW theory well, because the number of contact asperities increase, leading to the decrease in the uncertainty.

Fig. 6.9 shows the height and arrangement of the contact asperities, and the produced forces on the asperity contacts in one of 50 DAM results. For contact between a rigid plane and rough surface (*i.e.* displacement boundary condition), the asperities with higher heights get into contact with the plane, and they can be found by comparing the asperity heights and asperity contact forces between Figs. 6.9(a) and (b). The higher the asperity initially, the larger the asperity contact force. When $d/\sigma = 0$, 253 asperities, almost half, are involved in contact among 500 number of asperity.

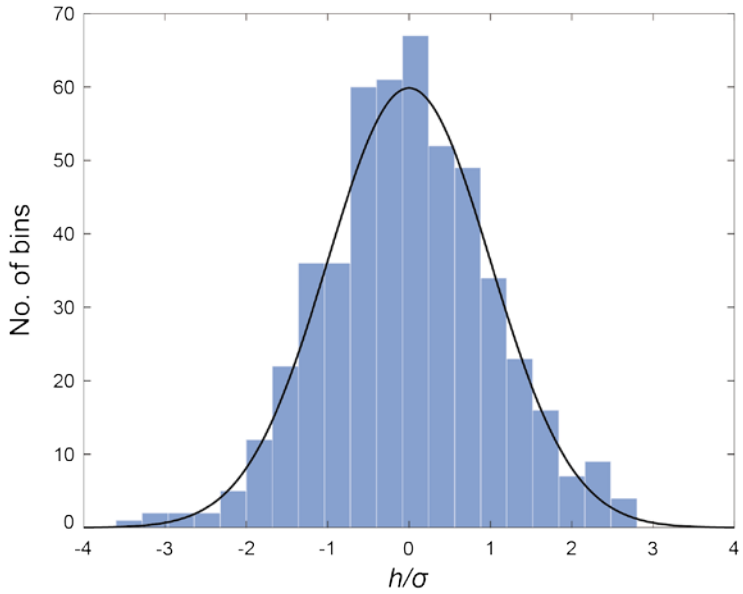

Figure 6.8. Asperity height distribution of one of the DAM result and the Gaussian function.

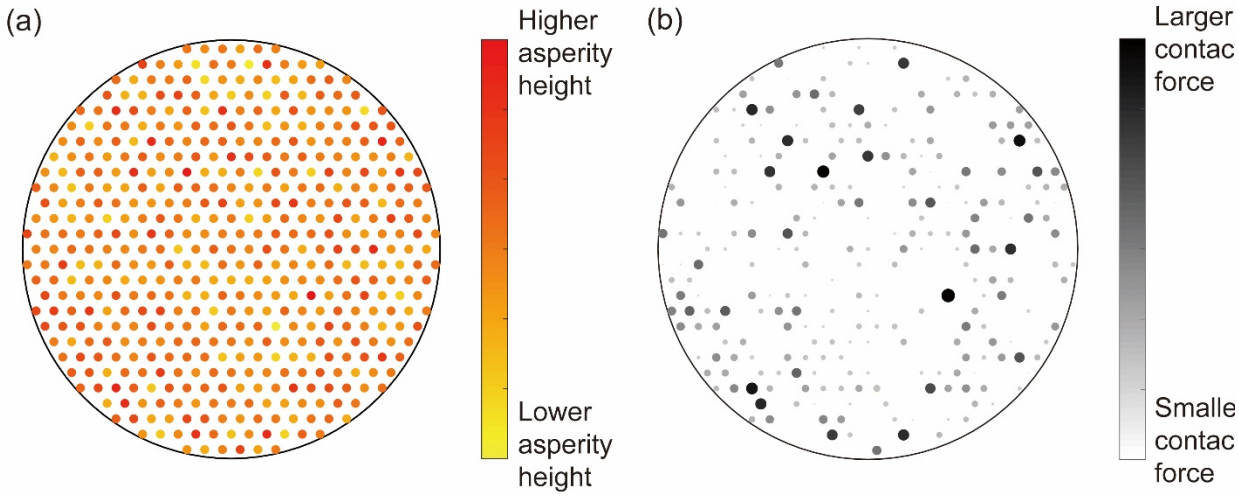

Figure 6.9. The DAM nominal contact area: (a) asperity height distribution with a temporary asperity radius, and (b) produced vertical force distribution when $d/\sigma = 0$.

6.3.2. Tangential stiffness

Here, the DAM coupling normal and shear forces is compared with frictional simulation results in the literature. The frictional stiffness as a function of the true contact area ratio was compared with the results suggested by Medina et al. (2013). Fig. 6.10 presents the comparison of the normalized tangential stiffness, defined as the ratio of the tangential stiffness with consideration of asperity interaction to one without the interaction. The tangential stiffness substantially decreases with the increase in the true contact area, meaning that the asperity interaction plays an important role in the frictional contact stiffness.

Despite the similar trend in Fig. 6.10, of a gradual increase in the normalized tangential stiffness with the decrease in the true contact area ratio, there is a discrepancy between the stiffness ratios obtained from the lateral force DAM and results of Medina et al. (2013). The possible explanation of the discrepancy is that the analytical and numerical models used in Medina et al. (2013) have different conditions: load type (force, rather than displacement), geometry (different asperity number, size, arrangement), and measurement method of the stiffness (the center asperity, rather than the nominal contact area). The details are found in the corresponding paper. Notwithstanding the short-term elastic model comparisons due to the absence of long-term results in the literature, the DAM appears to successfully capture and reproduce the response of rough surface contact. The static friction, or frictional strength, of rough surface contact was not compared, as they required plastic flow and surface energy.

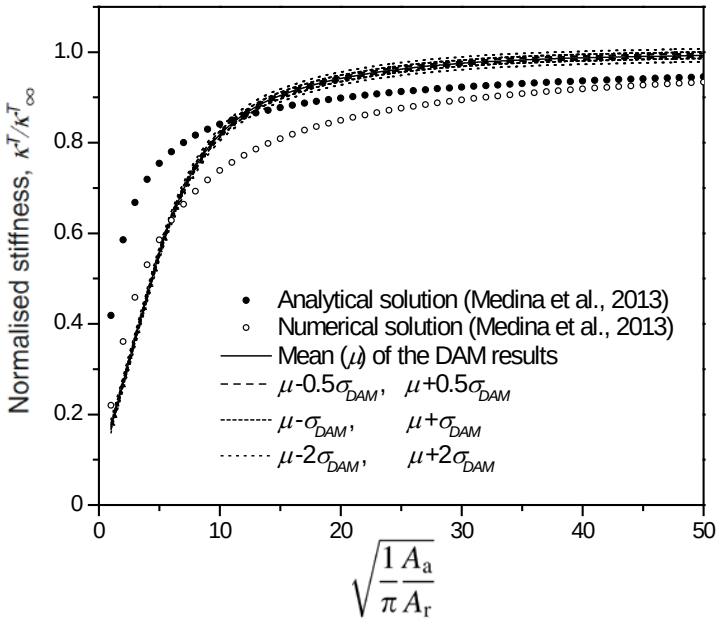

Figure 6.10. Comparison of the normalized tangential stiffness between the DAM and the analytical and numerical solutions found in Medina et al. (2013).

6.4. DAM simulation of the contact maturing process in sands

In the hybrid model simulations (Chapter 5), the consequences of the contact maturing process were re-distribution of contact force and uniform network of contact force chains on the nominal contact area. During the contact maturing process, the number of contact points gradually rises with time under prolonged loading, making the contact firmer. However, the increased number of contact points in the hybrid model must be interpreted with caution because it is directly dependent on the resolution of the DEM assembly. The hybrid model, by its nature of discrete element modeling, provides a qualitative trend of the number of contact points as a result of contact maturing, rather than quantitative features of the time-dependent rough surface contact. In addition, understanding the relationship between the increased number of contact points and firmer nominal contact is fundamental to a future prediction of the time-dependent strength and stiffness gains. In the subsection, a complete analysis of the time-dependent behavior of rough grain contact was executed using the DAM incorporating statistical asperity parameters and asperity creep model. This has enabled us to accurately estimate what happened at the grain contact over time in the grain-scale experiments.

6.4.1. Extraction of the asperity parameters

When it comes to the accurate and quantitative application of the DAM to real rough surface contact problems, asperity parameters of the rough contact, such as a asperity radius of curvature and asperity density, have to be found as inputs of the model. To model the grain-scale laboratory experiment using the suggested DAM approach in this study, the asperity parameters were estimated based on the statistical analyses of the grain surfaces used in the tests. It is well known that surface topography parameters can be found from the knowledge of the Power Spectral Density (PSD) analysis of rough surface (Longuet-Higgins, 1957a, 1957b; Bush et al., 1976). In the previous chapter, the PSD analysis of the surface profiles of the grains used in the grain-scale experiment was carried out. Taking advantage of this PSD result, the asperity parameters required to the DAM simulation were extracted.

Based on the PSD analysis of 2D rough surface, the zeroth, second, and fourth spectral moments, which can be related to the root-mean-square (RMS) height h_{rms}, the RMS slope h'_{rms}, and the RMS curvature h''_{rms}, are found as shown in the following (Jacobs et al., 2017)

$$m_0 = h_{rms}^2 = \frac{1}{A}\int_A h^2(x,y)dxdy = \frac{1}{A^2}\sum_{q_x,q_y}\left|\tilde{h}_{q_x,q_y}\right|^2 = \frac{1}{A}\sum_{q_x,q_y} C_{q_x,q_y}^{2D} \tag{6.14}$$

$$m_2 = \left(h'_{rms}\right)^2 = \frac{1}{A}\int_A \left|\nabla h(x,y)\right|^2 dxdy = \frac{1}{A^2}\sum_{q_x,q_y}\left(q_x^2+q_y^2\right)\left|\tilde{h}_{q_x,q_y}\right|^2 = \frac{1}{A}\sum_{q_x,q_y} q^2 C_{q_x,q_y}^{2D} \tag{6.15}$$

$$m_4 = \left(h''_{rms}\right)^2 = \frac{1}{4A}\int_A \left|\nabla^2 h(x,y)\right|^2 dxdy = \frac{1}{4A^2}\sum_{q_x,q_y}\left(q_x^2+q_y^2\right)^2\left|\tilde{h}_{q_x,q_y}\right|^2 = \frac{1}{4A}\sum_{q_x,q_y} q^4 C_{q_x,q_y}^{2D} \tag{6.16}$$

where

$$C_{q_x,q_y}^{2D} = \frac{1}{A}\left|\tilde{h}_{q_x,q_y}\right|^2 = \frac{1}{A}\left|l_x l_y \sum_{x,y} h_{x,y} e^{-i(q_x x+q_y y)}\right|^2 \tag{6.17}$$

The details including the descriptions of the symbols are found in Chapter 4.2. For an isotropic rough surface where any vertical cross-section of the rough surface is radially symmetric about the rotation center, the equivalent expressions for the spectral moments are

$$m_0 = \frac{1}{4\pi^2}\int C^{2D}_{q_x,q_y} d^2q = \frac{1}{2\pi}\int qC^{iso}_q dq \tag{6.18}$$

$$m_2 = \frac{1}{4\pi^2}\int q^2 C^{2D}_{q_x,q_y} d^2q = \frac{1}{2\pi}\int q^3 C^{iso}_q dq \tag{6.19}$$

$$m_4 = \frac{1}{16\pi^2}\int q^4 C^{2D}_{q_x,q_y} d^2q = \frac{1}{8\pi}\int q^5 C^{iso}_q dq \tag{6.20}$$

When a rough surface shows a self-affine characteristic (see Chapter 4.2 for the definition), the simple analytical expressions of the spectral moments are described by

$$m_0 = \frac{1}{2\pi}\int_A qC^{iso}_q dq = \frac{C_0}{4\pi H} q_l^{-2H} \tag{6.21}$$

$$m_2 = \frac{1}{2\pi}\int_A q^3 C^{iso}_q dq = \frac{1}{4\pi}\frac{C_0}{1-H} q_s^{2-2H} \tag{6.22}$$

$$m_4 = \frac{1}{8\pi}\int_A q^5 C^{iso}_q dq = \frac{1}{16\pi}\frac{C_0}{2-H} q_s^{4-2H} \tag{6.23}$$

where q_l and q_s are lower and upper limits of the wavevectors as depicted in Fig. 4.1. Using the three sets of spectral moment equations, the PSD can be calculated. Table 6.2 shows the zeroth, second, and fourth spectral moments of the grain surface used in the grain-scale laboratory experiments. They were computed from the three different methods mentioned above: (1) the full 2D PSD (C^{2D}) using Eqs. (6.14)-(6.16), (2) isotropic PSD (C^{iso}) using Eqs. (6.18)-(6.20), and (3) analytical PSD solutions of a fractal surface ($C^{fractal}$) using Eqs. (6.21)-(6.23). They present a good agreement, validating the computation and indicating isotropic characteristics of the sand grain surface. Considering the different PSD shapes (*e.g.*, an ideal curve for $C^{fractal}$ in Fig. 4.1) and assumptions used in derivation, the slightly different spectral moments are unavoidable.

Table 6.2. The zeroth, second, and fourth spectral moments of the grain surface computed from the different assumptions.

Test	m_0			m_2			m_4		
	C^{2D} Eq. (6.14)	C^{iso} Eq. (6.18)	$C^{fractal}$ Eq. (6.21)	C^{2D} Eq. (6.15)	C^{iso} Eq. (6.19)	$C^{fractal}$ Eq. (6.22)	C^{2D} Eq. (6.16)	C^{iso} Eq. (6.20)	$C^{fractal}$ Eq. (6.23)
A,B	8.17×10^{-4}	4.14×10^{-4}	8.87×10^{-4}	1.23×10^{-3}	0.96×10^{-3}	1.24×10^{-3}	0.106	0.061	0.033
C	0.103	0.098	0.106	0.545	0.490	0.546	147.520	130.148	77.886
D	0.333	0.288	0.339	1.128	0.997	1.130	320.808	272.209	127.473
E	0.386	0.322	0.390	3.546	3.204	3.549	1033.609	929.497	629.376

Longuet-Higgins (1957a, 1957b) presented that the density of surface asperity on the nominal contact per unit area can be calculated using the spectral moments of order 2 and 4 as shown in the following

$$N_s = \frac{1}{6\pi\sqrt{3}}\left(\frac{m_4}{m_2}\right) \tag{6.24}$$

The radius of asperity is given by the reciprocal of the asperity curvature κ_s. The mean curvature, suggested by Bush et al. (1976), is defined as

$$\kappa_s = \frac{1}{R_a} = \frac{8}{3}\sqrt{\frac{m_4}{\pi}} \tag{6.25}$$

Making use of Eqs. (6.24) and (6.25) along with the PSD analysis, the asperity parameters of the DAM simulations were found as presented in Table 6.3. The total number of asperities (N_0) on the nominal contact area and asperity radius (R_a) were simply calculated from the density of asperity per unit area and the mean asperity curvature, respectively. The determined asperity parameters will be used to construct discrete asperities on the nominal contact area in DEM simulation.

Table 6.3. The number of asperity and radius of asperity used in the DAM simulations of the experiments.

Test	*RMS* (nm)	*F* (N)	*R* (μm)	m_0	m_2	m_4	N_s (1/μm)	κ_s (1/μm)	N_0	R_a (nm)
A	28.6	1.3	19.5	8.17×10-4	1.23×10-3	0.106	2.623	0.489	3,133	2,046
B	28.6	2.4	25.0	8.17×10-4	1.23×10-3	0.106	2.623	0.489	5,150	2,046
C	321	2.4	25.0	0.103	0.545	147.520	8.289	18.273	16,275	54.7
D	577	1.3	19.5	0.333	1.128	320.808	8.711	26.947	10,406	37.1
E	621	2.4	25.0	0.386	3.546	1033.609	8.929	48.370	17,532	20.7

6.4.2. Asperity creep model

Contact maturing manifests itself as the time-dependent fracturing of contact asperity under sustained loading. In this regard, the grain convergence observed in the grain-scale laboratory testing can be modelled as the creep of contact asperities caused by high stress concentration in the DAM. The general mechanism of the material creep is classified as dislocation creep, climb, grain-boundary sliding, and diffusion flow (Pelleg, 2017). The general equation of the creep strain is given by

$$\frac{d\varepsilon}{dt} = \frac{C\sigma^m}{d^b} e^{-\frac{Q}{kT}} \tag{6.26}$$

where ε is the creep strain, C is the constant associated with the creep mechanism and material, σ is the stress, d is the grain size of the material, m and b are exponents dependent on the creep mechanism, Q is the activation energy, k is the Boltzmann constant, and T is the absolute temperature. Given that the delayed fracturing of contact asperity is controlled by the stress concentration, the dislocation creep mechanism is adopted as an asperity creep law in the DAM for the consideration of the time-dependent behavior of contact asperity. By substituting $b = 0$ (dislocation creep) and assuming the constant temperature and activation energy, Eq. (6.26) is simplified to

$$\frac{d\varepsilon}{dt} = B\sigma^m \tag{6.27}$$

where B is

$$B = Ce^{-\frac{Q}{kT}} \tag{6.28}$$

In Eq. (6.27), the variables are the elapse time t and stress σ acting on the asperity. The time-dependent model parameters B and m were calibrated with the experimental data. The equation does not reveal any nature of mechanism in asperity creep.

6.4.3. DAM simulation for the experiments

In the grain-scale laboratory experiments, there are two components of convergence: the time-dependent deformation of the grain core material (grain scale) and displacement due to the delayed fracturing of contact asperities (contact scale). As the former was already calculated by the half grain DEM analysis in Chapter 5.3, the latter is considered by the DAM simulation in this chapter.

To model the laboratory tests, the corresponding nominal contact areas with surface asperities whose number and radius are N_0 and R_a (Table 6.3) were generated. The heights of the surface asperities were assumed to be normally distributed with the RMS values corresponding to the real sand grain surfaces in the experiments. Like the experimental set-up of the grain-scale tests, the DAM simulates a case that a rough surface with myriad of surface asperities is compressed by the steel plate. By solving the load-displacement matrix, the DAM model calculated the produced forces at the individual contact asperities due to the induced displacements. The contact forces at the asperities lead to the asperity creep over time, resulting in the asperity deformation and global convergence. In order to mimic the sustained loading, a numerical servo-mechanism that keeps a vertical force constant was employed. When a contact force becomes smaller than the target sustained loading due to the asperity creep over time, the steel plate slightly penetrates into the rough surface to gain additional contact force for the target force. The increment of displacement of the steel plate and elapsed time were maintained small enough to ensure the constant loading condition and accurate simulation.

Given that the DAM simulation is based on sustained loading that is relatively low, it is assumed that individual asperity contacts are not merged over time in the DAM analysis. Laboratory observations of rough surface contact has shown that, as the applied load increases, the

number of contact areas increases to a maximum value due to plastic deformation of contact asperities, then decreases as a result of coalescent contact areas.

6.4.4. Results and discussions

In Fig. 6.11, the computed convergence, the sum of the grain deflections from the half-grain DEM and deformation of contact asperities from the DAM simulation, is plotted over the experimental data. The calibrated parameters of the asperity creep model (Eq. (6.27)) showing the best assessment of the experimental results are $B = 1.3\times10^{-27}$ and $m = 4$. The decaying process of convergence over time observed in the experiments was successfully captured by the DAM. As more number of asperity is involved in contact over time, an individual contact force reduced, thereby less individual asperity deformation by asperity creep. This leaded to small convergence with many number of contact points (on the matured contact). For simulation of each laboratory test, many DAM simulations with identical input parameters were performed. The DAM results were very consistent with a very small variation, despite the random generation of asperity heights. This is because of plenty of asperities on the nominal contact surface (*e.g.*, around ten thousand as shown in Table 6.3), resulting in reduction of uncertainty in random generation.

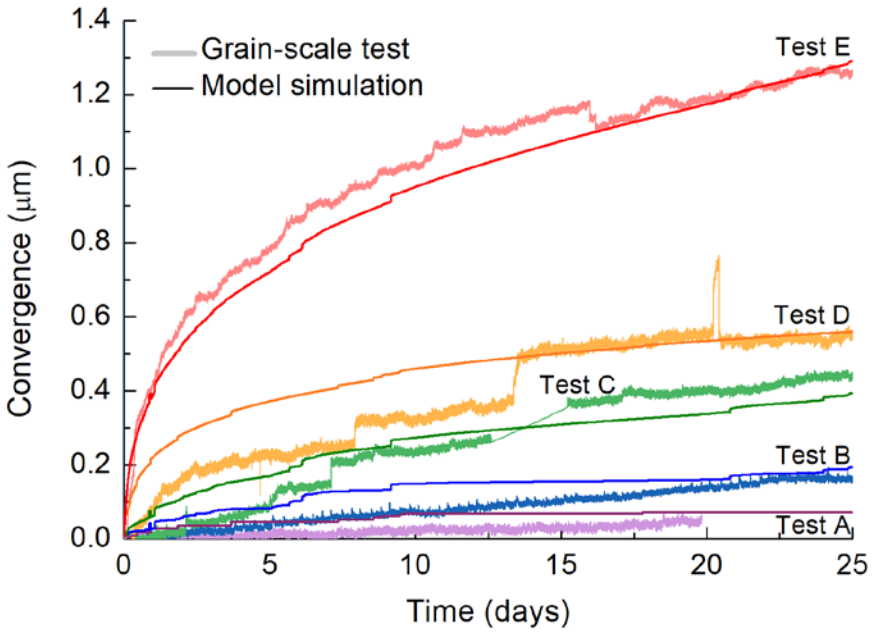

Figure 6.11. The grain-scale laboratory testing results and the sum of the half-grain DEM and nominal contact DAM model results.

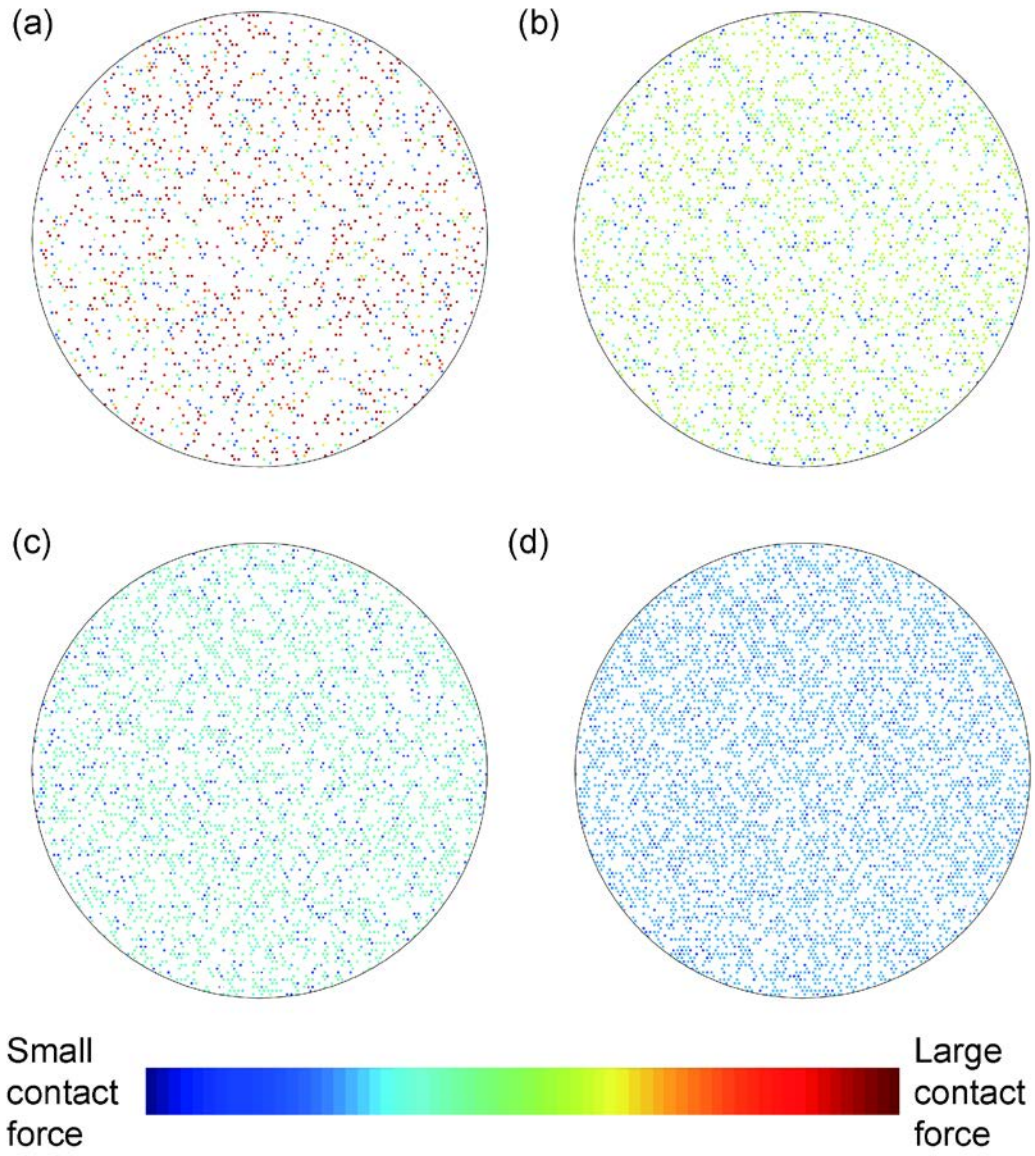

Figure 6.12. Contact points and corresponding contact forces captured in the DAM simulation of the test D: (a) t = 30 mins, (b) t = 1 day, (c) t = 5 days, and (d) t = 25 days.

Fig. 6.12 presents the change in the contact asperities and produced vertical forces on the nominal contact surface at different elapsed times. Over time, the delayed fracturing of contact asperities implemented by asperity creep model contributes to the increasing number of contact points under sustained loading. Owing to the increase in the number of contact points with the constant force on the nominal contact area, induced forces on individual asperity contact was reduced. This can be found by comparing the colors on the contact asperities, varying from red to

blue (Fig. 6.12). While these founding in the DAM are consistent to the results of the hybrid model, the DAM yields physically meaningful outcomes. Furthermore, the time-dependent frictional behaviors of the rough surface were studied using the coupled DAM with the normal and shear forces. Fig. 6.13 illustrates the number of asperity contacts, contact normal and shear stiffnesses, and frictional coefficient over time. All such factors increase over time as a consequence of contact maturing, albeit in different amounts. It reminds us of the beneficial sense in the word, contact maturing. The DAM results support not only the hybrid model results, but also previous findings in the literature. It is well founded that the static friction increases logarithmically with time in contact (Dieterich and Kilgore, 1994, Scholz and Engelder, 1976, Li et al., 2011). Kato et al. (1972) also showed that the static friction rises with time, and eventually converges a constant rate. One the time-dependent contact behavior is identified at contact nominal contact scale, the macroscopic geomaterial can be modelled with time by considering the granular contact behavior.

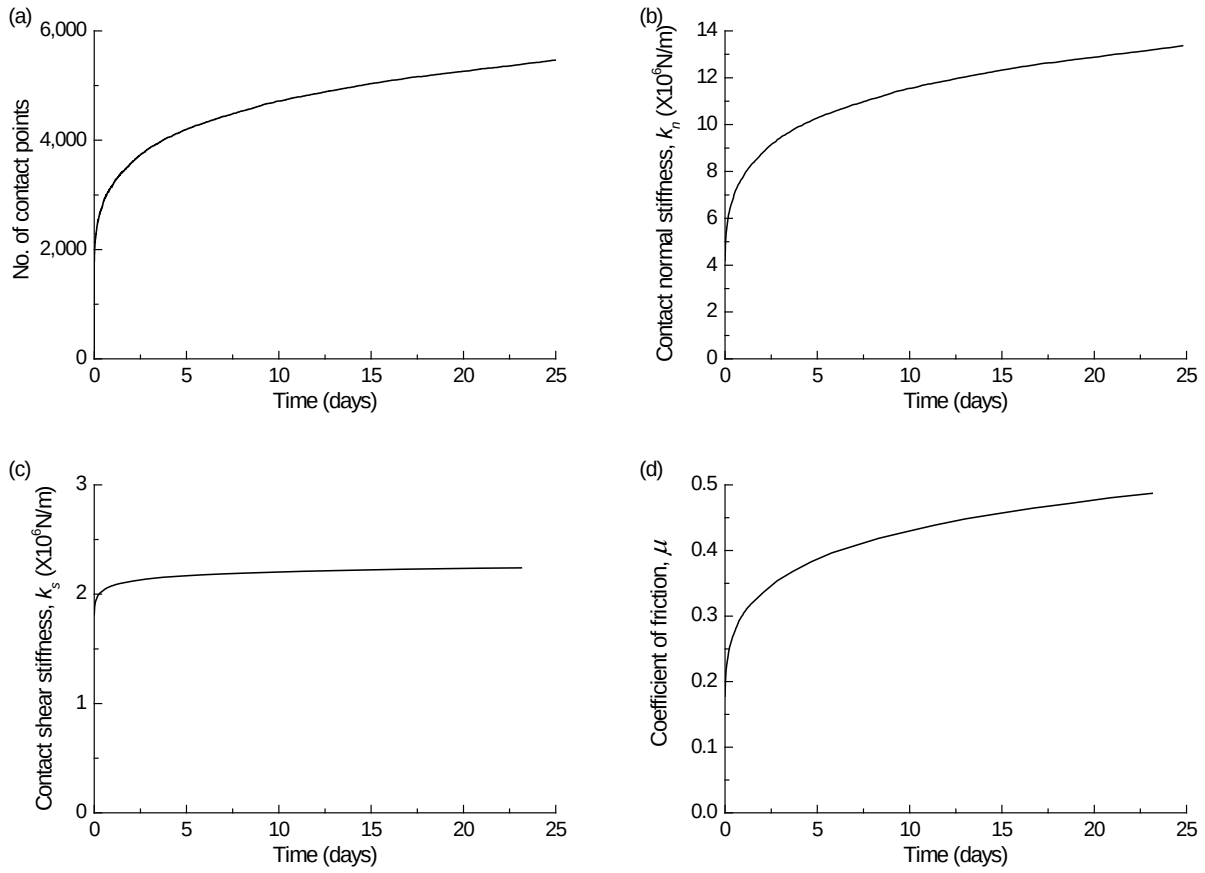

Figure 6.13. The time-dependent DAM simulation results of the test D: (a) the number of asperity contacts, (b) contact normal stiffness, (c) shear stiffness, and (d) frictional coefficient.

6.5. DAM simulation of frictional aging in rocks

Frictional aging associated with shear strength and stiffness not only occurs at granular contact, but also when rocks get into contact. The DAM model was applied to model rock frictional aging, in addition to the time-dependent sand grain contact behavior.

A number of studies have focused on frictional aging in rocks, but the outcomes seem to be different from sands. Note that here the frictional aging in sands is not the one between grain-to-grain contact, but the one related to sand assembly at macroscale (*e.g.* sand aging). In the case of sand assembly, the frictional stiffness of sands increases as observed in the triaxial tests (Daramola, 1980), but few results associated with the time-dependent shear strength increase have been reported in the literature. For rocks, on the other hand, the coefficient of static friction, which is the maximum shear strength divided by normal stress, grows with logarithm of the time that is held in stationary contact (Dieterich, 1972), in addition to the increase in the frictional stiffness. Although a key cause for this increase in the frictional strength at contact between rocks has not been understood, two processes are highly likely: 1) increase in true contact area by asperity creep, and 2) the formation and strengthening of interfacial chemical bonds. The two mechanisms of frictional aging are generally expressed as the increased contact 'quantity' and 'quality' with time. In this study, a third mechanism is proposed based on the contact maturing hypothesis: 3) increase in the number of contact points. Using the DAM, contact maturing as well as the above well-founded mechanisms are considered with an emphasis on the former. The following paragraph presents how to consider the three mechanisms using the DAM simulations.

1) Increased true contact area by asperity creep:

   For the consideration of aged surfaces, the contact areas of individual asperities are gradually raised, meaning that the contact patches are expanded. The total number of asperity contact is unchanged to exclude the influence of the third mechanism, which is the increased number of contact points. The ratio of single asperity frictional drop $\Delta F/F_{ss}$ related to chemical effects in Fig. 6.5 is constant at all contact asperities throughout the simulations with the assumption that they have the same bonding strength.

2) Strengthening of interfacial chemical bonds:

   At the single asperity level, different amounts of the static friction ratio ($\Delta F/F_{ss}$) are used to simulate different strengthening of asperity bonds over time. The individual contact area and the number of contact points in the nominal contact area are fixed.

3) Increase in the number of contact points:

   The nominal contact areas with different number of contact points are examined. The more the number of contact points, the longer the time subjected to the sustained loading. This simulation is somewhat different from the others in the way that the asperity contact area of individual asperity is not predetermined, instead it is calculated with given normal force and the number of contact asperities. Without this process, the third mechanism is actually identical to the first mechanism, as the true contact area linearly increases with the increase in the number of contact points. When the number of contact points increase due to the contact maturing process over time, the total constant force is distributed to a greater number of contacts, thereby the applied force on the individual asperity decrease. This leads to a smaller individual contact area than the one before aging (locally decrease, but the behavior of the total true contact area will be different). The frictional drop ratio at single asperity contact is constant without any asperity bonding strengthening over time.

These simulation overviews are summarized in Table 6.4. Because this modeling is to qualitatively demonstrate frictional aging of rocks based on the different mechanisms, the realistic asperity height distribution and arrangement are not included. In the DAM, all asperity on the nominal contact area are contact asperities and their heights are the same. Given that the vertical load on the nominal contact area is constant, the same normal force is applied throughout the simulations for the cases of all three mechanisms.

Table 6.4. Summary of the DAM inputs of the three mechanisms. A_i, ΔF_i, and N_i indicate the true contact area, frictional drop, and the number of contact points at the time t_i ($t_1 < t_2 < t_3$).

	True contact area	Frictional drop	Number of true contact
Mechanism 1	$A_1 < A_2 < A_3$	$\Delta F_1 = \Delta F_2 = \Delta F_3$	$N_1 = N_2 = N_3$
Mechanism 2	$A_1 = A_2 = A_3$	$\Delta F_1 < \Delta F_2 < \Delta F_3$	$N_1 = N_2 = N_3$
Mechanism 3	Has to be calculated	$\Delta F_1 = \Delta F_2 = \Delta F_3$	$N_1 < N_2 < N_3$

In the DAM simulations, the elastic properties of asperity are G = 44 GPa, ν = 0.25. The radius of nominal contact area (R) is 25 μm, $F_{ss} / (G\pi a^2) = 0.001$ where a is a radius of asperity contact area determined by the Hertz solution, a radius of spherical asperity R_a = 40 μm, total vertical force F^{tot} = 2.4 N, unless otherwise noted.

Because of the assumption that all asperities have the same height, whether a boundary condition is force or displacement has nothing to do with simulation results. Thus, the forces (F_z) are prescribed as external vertical loads involving aging on the nominal contact area. The total vertical force F^{tot} on the nominal contact area is uniformly distributed to N contact asperity, indicating that a single asperity is loaded by F^{tot}/N (= $F_{z,i}$, i = 1 … N). While the uniform vertical force compresses every contact asperity, the lateral displacements (u_x, u_y = 0) are also introduced at all asperities for frictional modeling. That is, all contact asperities move together with the identical lateral displacement, u_x. In summary, the two forces (F_x, F_y) and one displacement (u_z) are calculated from the applied vertical force (F_z) and lateral displacement boundary conditions (u_x, u_y = 0) on the asperities.

6.5.1. Mechanism 1: Increase true contact area by asperity creep

In order to simulate the increased true contact area over time, the total area of true asperity contact was increased by 10% and 20%. The total number of contact asperities in the nominal contact area is 361, and it didn't change with time. As seen in the insert in Fig. 6.14, each asperity contact is assumed to have the same ratio of the frictional drop $\Delta F/F_{ss}$ = 1 throughout the simulations with different aged time. Therefore, when an asperity reaches its peak strength and slides, it has the peak friction force $F_m = 2F_{ss}$.

Considering the different true asperity contact areas, Fig. 6.14 shows the DAM simulation results of the first frictional aging mechanism. At peak frictional strength, the ratios of the total produced lateral force (F_x^{tot}) for the contact areas $A_2 = 1.1A_1$, and $A_3 = 1.2\ A_1$ to the one for contact area A_1 (unaged) are 1.097, and 1.201, respectively (Fig. 6.14(a)). By frictional aging, the peak friction strength increases linearly with the increased true contact area. This consequence is consistent with the laboratory observation by Dieterich and Kilgore (1994). They found that the static friction is proportional to the contact area (the static friction and peak frictional strength linearly are correlated, as the constant normal force is applied the DAM), increasing

logarithmically with aging time (Fig. 2.15). One might notice that the frictional stiffness of the nominal contact is constant regardless of the increased true contact area over time, as shown in Fig. 6.14(a). It seems that the first mechanism, increase true contact area by asperity creep, does not lead to the contact stiffness increase over time.

It is also worth noting that, although the ratio of the peak lateral strength to the steady-state strength (F_m/F_{ss}) is 2 at individual asperity, the overall frictional strength ratio of the nominal contact is far less than the ratio, it is less than 1.3. This will be addressed in the simulation of the strengthening of interfacial bonding. As depicted in Fig. 6.14(b), the produced lateral forces at the contact asperities show partial slip, indicating that local slip occurs without gross slip.

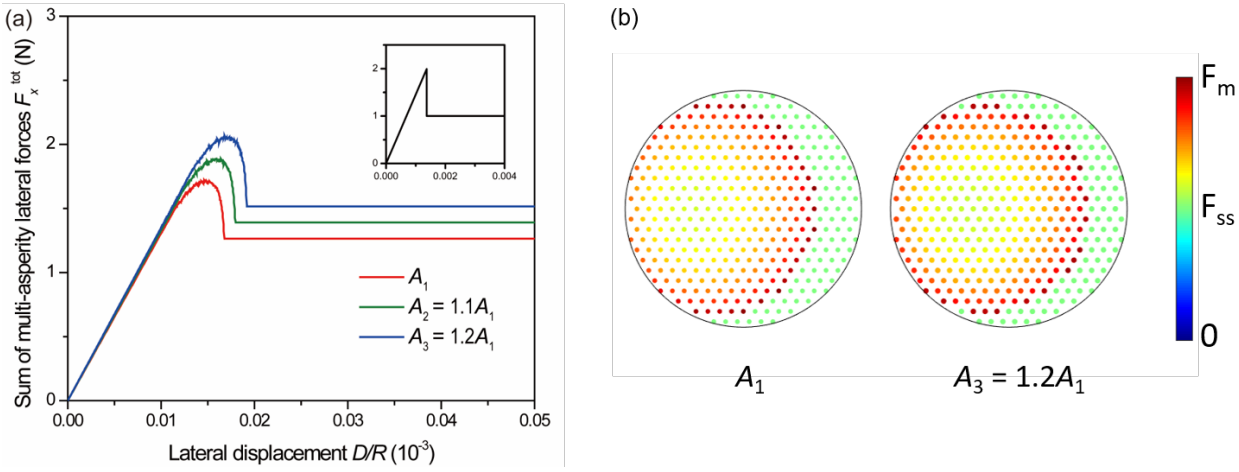

Figure 6.14. The DAM results of the mechanism 1: (a) lateral force-displacement, and (b) produced frictional forces on the contact asperities when the peak frictional force.

6.5.2. Mechanism 2: Strengthening of interfacial chemical bonds

Through the Frictional Force Microscopy (FFM) experiments, Li et al. (2011) found that frictional aging might stem from the time-dependent strengthening of chemical bonding between individual contact asperities, as illustrated in Fig. 2.16. As a result of interfacial bonding strengthening, the static friction increases over time, with constant steady-state frictional strength at the single asperity level. From the founding, one can model the nominal contact frictional behavior using asperities having different time-dependent bonding strengthes. With regards to different chemical bonding strengthes between asperities over aging time, the ratio of F_m to F_{ss} for single asperity was assumed to be 1.5, 2, 3, and 4. This force-displacement relationships of individual asperity in

Fig. 6.15(a) were employed for the multi-asperity simulation (DAM) in the nominal contact. Total 1,417 asperities were scattered on the nominal contact area to simulate the frictional modeling. The number of asperity contacts was constant for the all simulations.

Fig. 6.15(b) shows the results of DAM modeling with different asperity bonds strengthened for different times of aging. The values of the total lateral force divided by total steady-state lateral force (F_x^{tot}/F_{ss}^{tot}) for F_m/F_{ss} = 1.5, 2, 3, 4 are 1.06, 1.21, 1.61, 2.09. The results indicate that the produced shear force on the nominal contact is not equal to the sum of the peak shear strength of all asperities, instead it is much lower than the summation of individual asperity strength. This discrepancy is well explained in Li et al. (2011). Due to the elastic interaction among asperities, the shear stress is developed from the outermost circle of the nominal contact, and asperities there reach the maximum strength first (see the inserts in Fig. 6.15(b) presenting the produced shear stresses at asperity contact on the nominal contact area). On the other hand, those in center haven't sled yet providing little resistance. Once a partial slip occurs, however, asperities in the outer ring provide a much lower steady-state resistance. Because asperities on contacts experience different level of lateral forces according to the location, the corresponding peak resistance of each individual asperity cannot be achieved. In reality, the much larger frictional drop from peak to steady-state forces at small length-scale are observed in various phenomenon. For example, the frictional drop (ΔF) of aged rocks at macro-scale is less than 0.05 while the nanoscale single asperity testing of oxidized silicon wafer, which is having similar behavior of rocks, shows larger difference ranging from 0.5 to 5 (Li et al., 2011).

The strengthened asperity bonds over time result in the increased lateral strength. By strengthening the interfacial bonding, however, no increase of nominal contact stiffness is observed. In the simulation, the increase in contact shear stiffness due to aging is not likely to be caused by the chemical process.

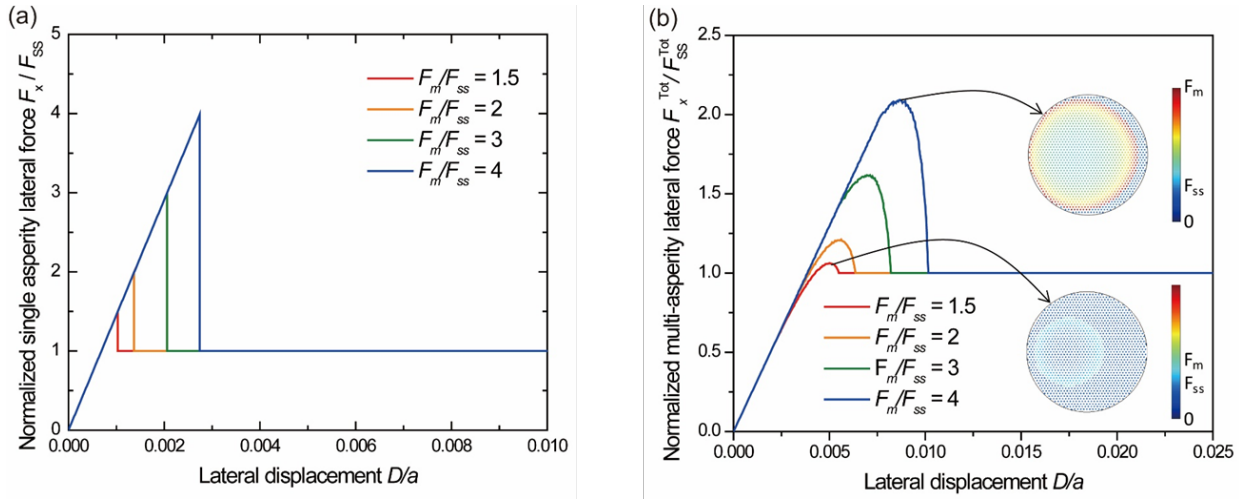

Figure 6.15. The DAM results of the mechanism 2: (a) single asperity behaviors used as input values, and (b) multi-asperity lateral force-displacement results.

6.5.3. Mechanism 3: Increase in the number of contact points

While the previous two mechanisms assume the uniform distribution of the total force to contact asperities, third mechanism considers both the uniform and Hertzian force distributions on the nominal contact area.

Uniform vertical force distribution on the nominal contact area

Given that the contact maturing process results in the increased number of contact point, the longer a nominal contact is subjected to the maturing process, the larger the number of asperities involved in the contact load transfer. By changing the number of contact asperities with different aging time in the DAM, this mechanism could be examined. Four simulations with the number of asperity contact, 163, 361, 649, 1417, were performed. The larger the number of asperity contact, the longer the time of aging. The total vertical force on the nominal contact area is identical for all cases, F^{tot} = 2.4 N, and the force acting on single asperity contact was calculated based on the divided vertical force, F^{tot}/N, for the uniform vertical force distribution simulation. Every asperity contact has the same ratio of frictional drop, $\Delta F/F_{ss}$ = 1. As the identical force is acting on all asperities in the nominal contact area, the radius of the individual asperity contact determined by the Hertz (1882)'s solution is the same.

Fig. 6.16 present the results of the case of the uniform force distribution on the nominal contact. Interestingly, the nominal contact simulation results of contact maturing mechanism show the increase in both frictional strength and stiffness. Considering that the total applied normal force on the nominal contact area is identical, a contact becomes firmer with increasing number of contacts (contact maturing) without a load increment. The aged contact with a greater number of contact points presents not only the increased peak frictional force but also increase in the steady-state strength. This is because, in the case of many asperity contacts, the total area of true contact is bigger than one with fewer contacts under constant normal loading. The large true contact provides more resistance to sliding.

The Fig. 6.16(b) represents developed frictional forces, F_x^{tot}, by the induced lateral displacements on the nominal contact surface. If a total vertical force is uniformly distributed on the nominal contact area, the smaller the number of true contact, the greater the force applied to that asperity contact. Therefore, the case of N = 163 shows bigger true contact area of individual asperity, but all contact asperities have the same area (uniform force distribution).

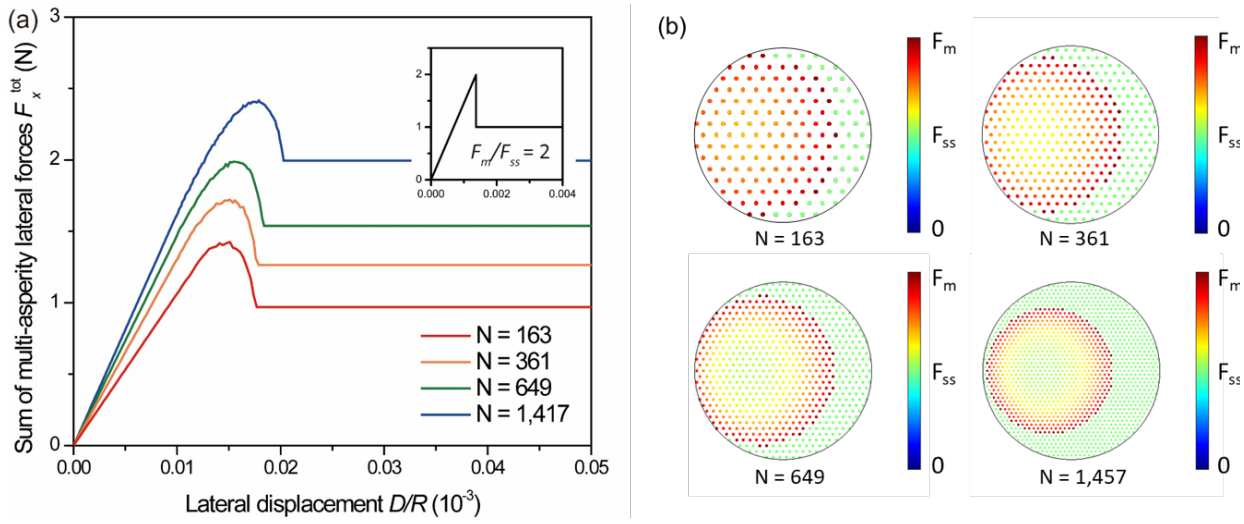

Figure 6.16. The DAM results of the mechanism 3 under the uniform force distribution: (a) lateral force-displacement, and (b) proposed frictional forces on the contact asperities over time when the peak frictional force.

Hertzian vertical force distribution on the nominal contact area

Hertz distribution of the total force was estimated based on the pressure distribution on Hertz contact. The applied force on i^{th} asperity can be calculated by

$$F_{zi} = F_0(1-\frac{r_i^2}{R^2})^{\frac{1}{2}}, \qquad F_0 = \frac{F^{tot}}{\sum_{i=1}^{N}(1-\frac{r_i^2}{R^2})^{\frac{1}{2}}} \tag{6.29}$$

When the Hertz distribution of force is considered as applied forces to nominal contact area, the results are not very different from the results with uniform loading as plotted in Fig. 6.17. Now, the asperities are loaded by different normal force according to their positions based on the Hertzian nominal contact force distribution. Because asperities with different area have different peak and steady-state strengths (with identical F_m/F_{ss} ratio, F_m/F_{ss} = 2), those who have small contact area reach the steady-state frictional force quickly. Therefore, all results show a narrow range of elastic deformation, as shown in Fig. 6.17(a) in comparison with the uniform vertical loading. In terms of the developed frictional forces, the area of steady-state contact with Hertz pressure distribution (outer annulus) is a lot bigger than that of the uniform force distribution, as plotted in Fig. 6.17(b). This is due to the different frictional strength, again. Asperities near the center of the nominal contact area are bigger, whereas those on the outermost are smaller. By the definition of the frictional strength, a small asperity provides less frictional strength, leading to the steady-state friction first. This wide variation of timing of the transition to peak and stead-state strength results in lower values of the static frictions with Hertz pressure than the one with uniform pressure.

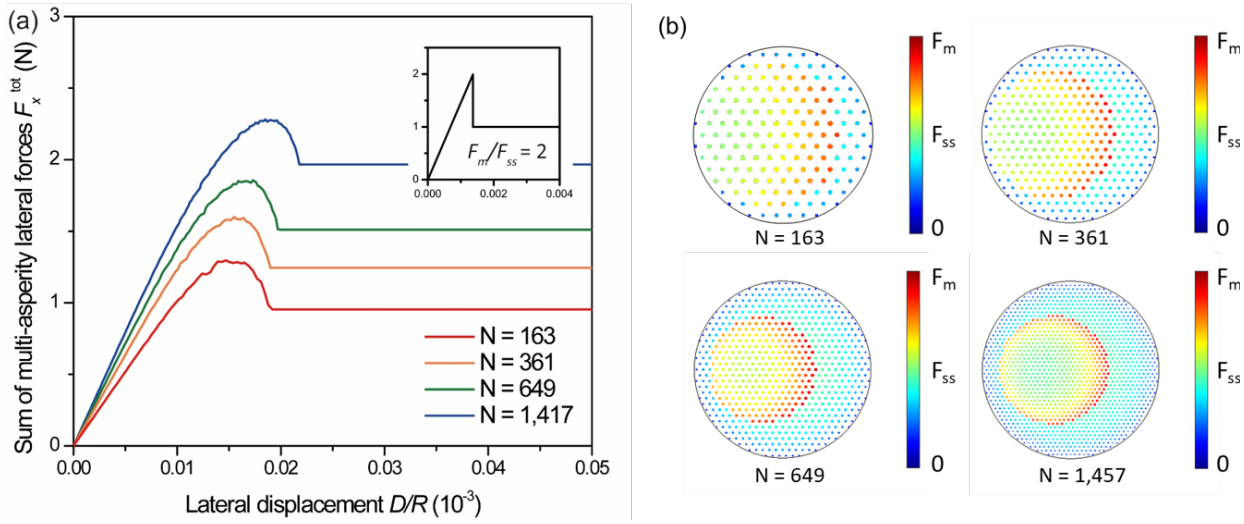

Figure 6.17. The DAM results of the mechanism 3 under the Hertzian force distribution: (a) lateral force-displacement, and (b) proposed frictional forces on the contact asperities over time when the peak frictional force.

6.5.4. Discussions

The DAM model suggested in the study successfully captured the time-dependent increase in the static friction of rocks. The simulation results of the three fictional aging mechanisms revealed that the frictional strength at the nominal contact increases with increase in the three mechanisms examined in the study: (1) the true contact area, (2) the strength of the chemical bonding, and (3) the number of contact point. It was found that the magnitude of the static friction increase became greater as theses effects are enhanced (the longer aging time). When Hertzian distribution of vertical force was applied to the nominal contact area with the assumption of grain-to-grain contact, the results are consistent with what the model of uniformly distributed force presented.

Surprisingly, the DAM simulation of the two well-known mechanisms in the literature don't explain the increase of the frictional stiffness over time. When the number of contact increased in the DAM simulation due to the contact maturing process, on the other hand, the frictional contact stiffness increased under the sustained loading. When it comes to the frictional stiffness increase over time, contact maturing is likely to be a key cause.

Based on the DAM simulations of frictional aging in rocks, a preliminary conclusion drawn here is that the time effect in rocks is attributed to the all three mechanisms considered in this subchapter, but contact maturing should be treated with utmost importance. Considering extensive experimental evidence associated with the two-well known hypotheses exist in the literature, the third one requires more attention.

Table 6.5. Summary of the results in the DAM simulations.

Cause	Scale	Increase	Frictional strength	Frictional stiffness
Mechanism 1	Single asperity	Contact area	Constant (–)	Constant (–)
	Nominal contact		Increase (↑)	Constant (–)
Mechanism 2	Single asperity	Peak strength	Increase (↑↑)	Constant (–)
	Nominal contact		Increase (↑)	Constant (–)
Mechanism 3	Single asperity	No. of contacts	Constant (–)	Constant (–)
	Nominal contact		Increase (↑)	Increase (↑)
All	Nominal contact	All three	Increase (↑)	Increase (↑)

6.6. Summary

In order to consider contact behavior of rough nominal contact, the normal and shear forces coupled DAM simulation was derived in this study. The suggested approach, then, was validated with the literature, though instant loading. The calibrated DAM simulation with the grain-scale laboratory experiments reproduced convergence using individual asperity creep, and showed the time-dependent changes in the important contact properties. Finally, frictional aging in rocks under sustained normal loading was studied. The quasi-static coupled DAM model successfully confirms that contact maturing (increase of contact points) plays an important role in increase of frictional strength and stiffness under prolonged loading. As a behavior of individual asperity can be described in the DAM, the suggested approach is a promising tool, having potential for a variety of future research.

Chapter 7

Summary and Conclusions

7.1. Summary and Conclusions

Soils and rocks age and change their engineering properties over time. Sands undergo a substantial change in small strain stiffness, penetration resistance, and liquefaction resistance with time. Previous studies found that initial stiffness of sand samples increases by approximately 50% for every log cycle of days, and the shaft capacity of the pile doubles within one year. Therefore, accounting for the time effect in sands in the development of construction sites and pile foundation systems would lead to economic benefits. For friction in rocks, a well-defined time-dependent dependence was developed: the static friction of rocks increases logarithmically with time when they are held in stationary contact. Because earthquakes are recognized as the result of a stick-slip frictional instability, understanding the frictional aging of rocks enables one to develop physically-based constitutive laws for earthquakes. To this end, an in-depth understanding of the time-dependent behavior in geo-materials has tremendous potential to contribute to economic and sustainable engineering practices. In the engineering community, however, there has been no consensus on the driving mechanisms behind these phenomena. Regarding the time-dependent property changes in sands, for example, various hypotheses were suggested in the last several decades, among them: physical process associated with changes in the fabric of grain assemblies,

chemical cementation, micro-biological processes, time-dependent fracturing of grains, and, most recently, static fatigue at the contacts between sand grains.

In this context, this PhD study investigated the physical origin of the time effects in geo-materials. In particular, the *static fatigue hypothesis* is supported, also straightforwardly referred to as *contact maturing hypothesis*, with an emphasis on the delayed fracturing of micro-morphological features on surfaces at contacts (asperities, crystalline fragments, and mineral debris). This suggests that the rich surface texture of a contact surface makes the surface asperities vulnerable to sub-critical fracturing, which is manifested as a delayed response to sustained loads. Throughout the PhD study, it was found out that contact maturing is likely to be a key cause of the time effects. Laboratory observations and physical testing showed time-dependent fracturing and crushing of asperities at contact over time. Numerical models successfully mimicked the maturing process of individual contacts and the consequences on the time-dependent behavior of granular assemblies. The conclusions are summarized below.

Observation of Contact and the Contact Maturing Process

As the contact maturing is strongly dependent on surface roughness, this study addresses quantitative characterization of roughness of sand grain surfaces, and its influence on the contact maturing process. Firstly, a rich texture of sand grain surfaces was confirmed by observations using the Atomic Force Microscope (AFM). With the surface profiles of sand grains obtained from AFM, the typical surface roughness parameters were examined, and the fractal dimension was identified from the Power Spectral Density (PSD) analysis. Three grain testing was conducted to quantitatively characterize the time-dependent changes of surface morphological features before and after contact maturing. Based on the statistical analysis of both fresh and matured surfaces, constant loading caused delayed damage on to the major contact asperities, but also to very small asperities. The latter are difficult to identify by the means used in the study, but they are identifiable through the statistical analysis. In the grain-scale laboratory experiments, the grain deflection over time was heavily dependent on the initial roughness of sand grains. The more rough the grain surface, the larger the deflection over time. This intense contact maturing in the rough surface is due to high stress concentration on contact asperities, causing a large amount of asperity fracturing and plastic deformation.

Hybrid model of grain contact behavior

Using the statistical information of surface roughness and grain deflection obtained from the surface observation and laboratory test results, a distinct element model (DEM) and a finite element model (FEM) were employed to simulate the process of contact maturing on two scales: the grain scale and the contact scale. This approach modeled the grain-scale laboratory experiment: a single grain subjected to a prolonged load applied through two steel plates. The measured deflection was considered as the sum of displacement caused by creep of the core mineral in the grain and the displacement owed to static fatigue of the rough surfaces at the contacts. The contact process that is difficult to track in physical testing appears to be captured well by the model. In the simulations, the delayed fracturing of simulated contact asperities leads to an increase in the number of contact points within the nominal contact area. Consequently, the load transferred through the contact becomes progressively more uniformly distributed over the nominal contact area as the process continues. This, in turn, produces an increase in the stiffness of the contacts, and results in an increase of the macroscopic stiffness of sand.

Discrete asperity modeling of contacts

While the distinct element model on two scales demonstrates the trends in the contact maturing process, practical application of contact maturing requires methodologies and tools associated with continuum mechanics theories. A mechanical approach formulated using elementary potential solutions was suggested. The main idea is a discretization of the nominal contact into individual asperity level, *i.e.* small 'sub-true' contact asperities. The collection of the elastic interplays among these sub-contacts at the elementary level is analogue to the mechanism of the nominal contact. Once the creep rate law of nanoscopically sharp single asperity contact is specified, the time-dependent behavior of the overall nominal contact at microscale can be found. The discrete asperity modeling results (DAM) were found to be consistent with the contact maturing hypothesis, and showed that aging is a length scale-dependent phenomenon. The model calculated the time-dependent contact-to-contact response to sustained loads, the number of contact points, contact normal and shear stiffnesses, and the frictional coefficient. These results will be employed as a building block for a granular assembly analysis including numerous granular contacts.

7.2. Recommendations for future research

Future research recommendations are listed below.

Further investigation of the contact maturing process

This topic is an extension of this PhD study – what is the origin of the time-dependent behavior of soils and rocks? The time-dependent behavior of geo-materials has been considered based on an empirical and phenomenological models without physical description of the process. For more confident engineering design, mathematical framework of the time effect has to be developed. For that purpose, a time-dependent grain-scale testing under complex but realistic loading conditions are required to investigate the nature of contact evolution. By improving the suggested discrete approaches along with the experiments, a complete numerical model can be developed, which is vital for up-scaled field analyses.

Long-term grain split under sustained loading

Subcritical fracturing of individual particles alters physical properties of the entire grain assembly, resulting in new constitutive behavior. This has long been recognized as a possible cause of the time-dependent behavior in granular soils. While considerable effort has been devoted to the short-term crushing behavior of individual sand grains in the literature, few studies focused on time-dependent grain splitting caused by subcritical crack propagation. The consequences of stress-corrosion cracking on long-term grain splitting remains unclear. The preliminary study on the subcritical grain splitting in this PhD study indicates a different failure mode and the crack development compared to abrupt grain crushing. It is recommended that studies on the delayed grain fracture be continued.

REFERENCES

AFIFI, S. & RICHART, F. 1973. Stress-history effects on shear modulus of soils. *Soils and Foundations,* 13**,** 77-95.

AFIFI, S. S. & WOODS, R. D. 1971. Long-term pressure effects on shear modulus of soils. *Journal of Soil Mechanics & Foundations Div.*

ANDERSON, D. & STOKOE, K. 1978. Shear modulus: a time-dependent soil property. *Dynamic geotechnical testing.* ASTM International.

ARANGO, I., LEWIS, M. & KRAMER, C. 2000. Updated liquefaction potential analysis eliminates foundation retrofitting of two critical structures. *Soil Dynamics and Earthquake Engineering,* 20**,** 17-25.

ARANGO, I. & MIGUES, R. E. 1996. *Investigation on the seismic liquefaction of old sand deposits,* Bechtel Corporation.

ARCHARD, J. 1957. Elastic deformation and the laws of friction. *Proceedings of the Royal Society of London. Series A. Mathematical and Physical Sciences,* 243**,** 190-205.

ASADI, M. S., RASOULI, V. & BARLA, G. 2012. A bonded particle model simulation of shear strength and asperity degradation for rough rock fractures. *Rock Mechanics and Rock Engineering,* 45**,** 649-675.

ASHFORD, S. A., ROLLINS, K. M. & LANE, J. D. 2004. Blast-induced liquefaction for full-scale foundation testing. *Journal of Geotechnical and Geoenvironmental Engineering,* 130**,** 798-806.

AXELSSON, G. 2000. Long-term set-up of driven piles in sand. PhD thesis. *Royal Institute of Technology, Stockholm, Sweden.*

BAHAADDINI, M., HAGAN, P., MITRA, R. & KHOSRAVI, M. 2016. Experimental and numerical study of asperity degradation in the direct shear test. *Engineering geology,* 204**,** 41-52.

BAHAADDINI, M., SHARROCK, G. & HEBBLEWHITE, B. 2013. Numerical direct shear tests to model the shear behaviour of rock joints. *Computers and Geotechnics,* 51**,** 101-115.

BARBER, J. R. 2018. *Contact mechanics,* Springer.

BAXTER, C. D. & MITCHELL, J. K. 2004. Experimental study on the aging of sands. *Journal of Geotechnical and Geoenvironmental Engineering,* 130**,** 1051-1062.

BAŽANT, Z. P. 1999. Size effect on structural strength: a review. *Archive of applied Mechanics,* 69**,** 703-725.

BHUSHAN, B. 2000. *Modern tribology handbook, two volume set*, CRC press.

BOUCHAUD, E. 1997. Scaling properties of cracks. *Journal of Physics: Condensed Matter,* 9**,** 4319.

BOWMAN, E. T. & SOGA, K. 2003. Creep, ageing and microstructural change in dense granular materials. *Soils and Foundations,* 43**,** 107-117.

BOWMAN, E. T. & SOGA, K. 2005. Mechanisms of setup of displacement piles in sand: laboratory creep tests. *Canadian geotechnical journal,* 42**,** 1391-1407.

BUSH, A., GIBSON, R. & KEOGH, G. 1976. The limit of elastic deformation in the contact of rough surfaces. *Mechanics Research Communications,* 3**,** 169-174.

CHARLIE, W. A., RWEBYOGO, M. F. & DOEHRING, D. O. 1992. Time-dependent cone penetration resistance due to blasting. *Journal of Geotechnical Engineering,* 118**,** 1200-1215.

CHENG, Y., NAKATA, Y. & BOLTON, M. 2003. Discrete element simulation of crushable soil. *Geotechnique,* 53**,** 633-641.

CHOW, F., JARDINE, R., BRUCY, F. & NAUROY, J. 1998. Effects of time on capacity of pipe piles in dense marine sand. *Journal of Geotechnical and Geoenvironmental Engineering,* 124**,** 254-264.

CIAVARELLA, M., GREENWOOD, J. & PAGGI, M. 2008. Inclusion of ″interaction″ in the Greenwood and Williamson contact theory. *Wear,* 265**,** 729-734.

CIL, M. & ALSHIBLI, K. 2012. 3D assessment of fracture of sand particles using discrete element method. *Géotechnique Letters,* 2**,** 161-166.

CIL, M. & ALSHIBLI, K. 2014. 3D evolution of sand fracture under 1D compression. *Géotechnique,* 64**,** 351.

CUNDALL, P. A. & STRACK, O. D. 1979. A discrete numerical model for granular assemblies. *geotechnique,* 29**,** 47-65.

DARAMOLA, O. 1980. Effect of consolidation age on stiffness of sand. *Geotechnique,* 30**,** 213-216.

DEJONG, J. T., FRITZGES, M. B. & NÜSSLEIN, K. 2006. Microbially induced cementation to control sand response to undrained shear. *Journal of Geotechnical and Geoenvironmental Engineering,* 132**,** 1381-1392.

DENISOV, N., DUDLERS, I., DURANTI, E. & KHAZANOV, M. Studies of changes of strength and compressibility of hydraulically filled sands in time. European Conference on Soil Mechanics and Foundation Engineering, 1963. 221-225.

DIETERICH, J. H. 1972. Time-dependent friction in rocks. *Journal of Geophysical Research,* 77**,** 3690-3697.

DIETERICH, J. H. & KILGORE, B. D. 1994. Direct observation of frictional contacts: New insights for state-dependent properties. *Pure and Applied Geophysics,* 143**,** 283-302.

DOWDING, C. H. & HRYCIW, R. D. 1986. A laboratory study of blast densification of saturated sand. *Journal of Geotechnical Engineering,* 112**,** 187-199.

DUMAS, J. C. & BEATON, N. F. 1988. Discussion of ″Practical Problems from Surprising Soil Behavior″ by James K. Mitchell (March, 1986, Vol. 112, No. 3). *Journal of Geotechnical Engineering,* 114**,** 367-368.

FRYE, K. M. & MARONE, C. 2002. Effect of humidity on granular friction at room temperature. *Journal of Geophysical Research: Solid Earth,* 107**,** ETG 11-1-ETG 11-13.

FU, R., HU, X. & ZHOU, B. 2017. Discrete element modeling of crushable sands considering realistic particle shape effect. *Computers and Geotechnics,* 91**,** 179-191.

GADELMAWLA, E., KOURA, M., MAKSOUD, T., ELEWA, I. & SOLIMAN, H. 2002. Roughness parameters. *Journal of materials processing Technology,* 123**,** 133-145.

GREENWOOD, J. & TRIPP, J. 1970. The contact of two nominally flat rough surfaces. *Proceedings of the institution of mechanical engineers,* 185**,** 625-633.

GREENWOOD, J. & WILLIAMSON, J. P. 1966. Contact of nominally flat surfaces. *Proceedings of the royal society of London. Series A. Mathematical and physical sciences,* 295**,** 300-319.

HERTZ, H. 1882. Ueber die Beruhrung fester elastischer Korper. *J reine angew Math,* 92**,** 156-171.

HIRAMATSU, Y. & OKA, Y. Determination of the tensile strength of rock by a compression test of an irregular test piece. International Journal of Rock Mechanics and Mining Sciences & Geomechanics Abstracts, 1966. Elsevier, 89-90.

HIRAMATSU, Y. & OKA, Y. 1967. Determination of the Tensile Strength of Rock by a Compression test of an irregular test piece: Authors' reply to discussion *International Journal of Rock Mechanics and Mining Sciences & Geomechanics Abstracts,* 4**,** 363-365.

HOWIE, J., SHOZEN, T. & VAID, Y. 2002. Effect of ageing on stiffness of very loose sand. *Canadian geotechnical journal,* 39**,** 149-156.

ITASCA CONSULTING GROUP, I. 2008. PFC2D (Particle Flow Code in 2 Dimensions) User′s Guide, Version 4.0. *Minneapolis, MN*.

JACOBS, T. D., JUNGE, T. & PASTEWKA, L. 2017. Quantitative characterization of surface topography using spectral analysis. *Surface Topography: Metrology and Properties,* 5**,** 013001.

JAMIOLKOWSKI, M., LOPRESTI, D. & PALLARA, O. 1995. Role of in-situ testing in geotechnical earthquake engineering.

JARDINE, R. J., STANDING, J. R. & CHOW, F. C. 2006. Some observations of the effects of time on the capacity of piles driven in sand. *Géotechnique,* 56**,** 227-244.

JOHNSON, K. L. & JOHNSON, K. L. 1987. *Contact mechanics*, Cambridge university press.

JOSHI, R., ACHARI, G., KANIRAJ, S. R. & WIJEWEERA, H. 1995. Effect of aging on the penetration resistance of sands. *Canadian Geotechnical Journal,* 32**,** 767-782.

KANAFI, M. M. & TUONONEN, A. J. 2017. Top topography surface roughness power spectrum for pavement friction evaluation. *Tribology International,* 107**,** 240-249.

KATO, S., SATO, N. & MATSUBAYASHI, T. 1972. Some considerations on characteristics of static friction of machine tool slideway.

KROLL, R. 1990. Alkalophiles. *Microbiology of Extreme Environments. McGraw-Hill, New York, NY***,** 55-92.

KUHN, M. R. 1989. Micromechanical aspects of soil creep.

KULHAWY, F. H. & MAYNE, P. W. 1990. Manual on estimating soil properties for foundation design. Electric Power Research Inst., Palo Alto, CA (USA); Cornell Univ., Ithaca ....

KWOK, C.-Y. & BOLTON, M. 2010. DEM simulations of thermally activated creep in soils. *Géotechnique,* 60**,** 425-433.

LADE, P. V. & KARIMPOUR, H. 2010. Static fatigue controls particle crushing and time effects in granular materials. *Soils and Foundations,* 50**,** 573-583.

LEON, E., GASSMAN, S. L. & TALWANI, P. 2006. Accounting for soil aging when assessing liquefaction potential. *Journal of Geotechnical and Geoenvironmental Engineering,* 132**,** 363-377.

LEWIS, M., ARANGO, I., KIMBALL, J. & ROSS, T. Liquefaction resistance of old sand deposits. Proc., 11th Panamerican Conf. on Soil Mechanics and Geotechnical Engineering, 1999. ABMS San Paulo, Brazil, 821-829.

LI, Q., TULLIS, T. E., GOLDSBY, D. & CARPICK, R. W. 2011. Frictional ageing from interfacial bonding and the origins of rate and state friction. *Nature,* 480**,** 233.

LI, S., YAO, Q., LI, Q., FENG, X.-Q. & GAO, H. 2018. Contact stiffness of regularly patterned multi-asperity interfaces. *Journal of the Mechanics and Physics of Solids,* 111**,** 277-289.

MCDOWELL, G. & HARIRECHE, O. 2002. Discrete element modelling of soil particle fracture. *Géotechnique,* 52**,** 131-135.

MEDINA, S., NOWELL, D. & DINI, D. 2013. Analytical and numerical models for tangential stiffness of rough elastic contacts. *Tribology Letters,* 49**,** 103-115.

MESRI, G., FENG, T. & BENAK, J. 1990. Postdensification penetration resistance of clean sands. *Journal of Geotechnical Engineering,* 116**,** 1095-1115.

MICHALOWSKI, R. & NADUKURU, S. Contact fatigue: a key mechanism of time effects in silica sand. International Symposium on Geomechanics from Micro to Macro, IS-Cambridge, 2014.

MICHALOWSKI, R. L. & NADUKURU, S. S. 2012. Static fatigue, time effects, and delayed increase in penetration resistance after dynamic compaction of sands. *Journal of Geotechnical and Geoenvironmental Engineering,* 138**,** 564-574.

MICHALOWSKI, R. L., WANG, Z. & NADUKURU, S. S. 2018a. Maturing of contacts and ageing of silica sand. *Géotechnique,* 68**,** 133-145.

MICHALOWSKI, R. L., WANG, Z., PARK, D. & NADUKURU, S. S. Static fatigue or maturing of contacts in silica sand. GeoShanghai International Conference, 2018b. Springer, 911-918.

MITCHELL, J. K. & SANTAMARINA, J. C. 2005. Biological considerations in geotechnical engineering. *Journal of geotechnical and geoenvironmental engineering,* 131**,** 1222-1233.

MITCHELL, J. K. & SOLYMAR, Z. V. 1984. Time-dependent strength gain in freshly deposited or densified sand. *Journal of Geotechnical Engineering,* 110**,** 1559-1576.

NADUKURU, S. S. 2013. Static Fatigue: A Key Cause of Time Effects in Sand. *Ph.D. Dissertation, Department of Civil and Environmental Engineering, University of Michigan, Ann Arbor*.

NAKATA, Y., KATO, Y., HYODO, M., HYDE, A. F. & MURATA, H. 2001. One-dimensional compression behaviour of uniformly graded sand related to single particle crushing strength. *Soils and foundations,* 41**,** 39-51.

NARSILIO, G. A., SANTAMARINA, J. C., HEBELER, T. & BACHUS, R. 2009. Blast densification: multi-instrumented case history. *Journal of Geotechnical and Geoenvironmental Engineering,* 135**,** 723-734.

NAYAK, P. R. 1971. Random process model of rough surfaces. *Journal of Lubrication Technology,* 93**,** 398-407.

OKA, Y. & MAJIMA, H. 1970. A theory of size reduction involving fracture mechanics. *Canadian Metallurgical Quarterly,* 9**,** 429-439.

ORFORD, J. & WHALLEY, W. 1987. The quantitative description of highly irregular sedimentary particles: the use of the fractal dimension. *Clastic Particles. Van Nostrand Reinhold Company, New York,* 267-280.

PARK, J.-W. & SONG, J.-J. 2009. Numerical simulation of a direct shear test on a rock joint using a bonded-particle model. *International Journal of Rock Mechanics and Mining Sciences,* 46**,** 1315-1328.

PEJCHAL, V., ŽAGAR, G., CHARVET, R., DÉNÉRÉAZ, C. & MORTENSEN, A. 2017. Compression testing spherical particles for strength: Theory of the meridian crack test and implementation for microscopic fused quartz. *Journal of the Mechanics and Physics of Solids,* 99**,** 70-92.

PELLEG, J. 2017. Creep in ceramics. *Creep in Ceramics.* Springer.

PERSSON, B., ALBOHR, O., TARTAGLINO, U., VOLOKITIN, A. & TOSATTI, E. 2005. On the nature of surface roughness with application to contact mechanics, sealing, rubber friction and adhesion. *Journal of physics: Condensed matter,* 17**,** R1.

PERSSON, B. N. 2006. Contact mechanics for randomly rough surfaces. *Surface science reports,* 61**,** 201-227.

PERSSON, B. N. 2013. *Sliding friction: physical principles and applications,* Springer Science & Business Media.

POTYONDY, D. O. 2007. Simulating stress corrosion with a bonded-particle model for rock. *International Journal of Rock Mechanics and Mining Sciences,* 44**,** 677-691.

POTYONDY, D. O. & CUNDALL, P. 2004. A bonded-particle model for rock. *International journal of rock mechanics and mining sciences,* 41**,** 1329-1364.

ROBERTSON, D. & BOLTON, M. 2001. DEM simulations of crushable grains and soils. *Powders and Grains,* 1.

SCHMERTMANN, J. H. 1991. The mechanical aging of soils. *Journal of Geotechnical Engineering,* 117**,** 1288-1330.

SCHOLZ, C. & ENGELDER, J. The role of asperity indentation and ploughing in rock friction—I: Asperity creep and stick-slip. International Journal of Rock Mechanics and Mining Sciences & Geomechanics Abstracts, 1976. Elsevier, 149-154.

SCHÖPFER, M. P., ABE, S., CHILDS, C. & WALSH, J. J. 2009. The impact of porosity and crack density on the elasticity, strength and friction of cohesive granular materials: insights from DEM modelling. *International Journal of Rock Mechanics and Mining Sciences,* 46**,** 250-261.

SEED, B. 1979. Soil liquefaction and cyclic mobility evalution for level ground during earthquakes. *Journal of geotechnical and geoenvironmental engineering,* 105.

SKEMPTON, A. 1986. Standard penetration test procedures and the effects in sands of overburden pressure, relative density, particle size, ageing and overconsolidation. *Geotechnique,* 36**,** 425-447.

SUN, Z., TANG, H., ESPINOZA, D. N., BALHOFF, M. T. & KILLOUGH, J. E. 2018. Discrete element modeling of grain crushing and implications on reservoir compaction. *Journal of Petroleum Science and Engineering,* 171**,** 431-439.

TAVENAS, F. & AUDY, R. 1972. Limitations of the driving formulas for predicting the bearing capacities of piles in sand. *Canadian Geotechnical Journal,* 9**,** 47-62.

VALLEJO, L. E. Fractal analysis of granular materials. International journal of rock mechanics and mining sciences and geomechanics abstracts, 1995. 371A.

VEECO INSTRUMENTS, I. 2004. NanoScope Software 6.13 User Guide 004-132-000.

VEECO INSTRUMENTS, I. 2010. Veeco Dimension Icon Instruction Manual 004-1023-000.

WANG, P., BAKHTIARY, E., ECKER, S., ARSON, C., CHRISTOPHER, T. & FRANCIS, K. Discrete Element modeling and analysis of shielding effects during the crushing of a grain. 2015. Georgia Institute of Technology.

WANG, Y.-H., XU, D. & TSUI, K. Y. 2008. Discrete element modeling of contact creep and aging in sand. *Journal of geotechnical and geoenvironmental engineering,* 134**,** 1407-1411.

WANG, Z. 2017. Contact maturing and aging of silica sand. *Ph.D. Dissertation, Department of Civil and Environmental Engineering, University of Michigan, Ann Arbor.*

WANG, Z. & MICHALOWSKI, R. L. 2015. Contact fatigue in silica sand—Observations and modeling. *Geomechanics for Energy and the Environment,* 4**,** 88-99.

WANG, Z. & MICHALOWSKI, R. L. 2018. An Apparatus for Testing Static Fatigue at Sand Grain Contacts. *Geotechnical Testing Journal,* 41.

WANG, Z., PARK, D. & MICHALOWSKI, R. L. Contact maturing in silica sand. Int. Conf. Soil Mech. Geotech. Eng., Sept. 17-11, 2017 2017 Seoul, South Korea. Springer, 1103-1106.

ZHANG, X.-P. & WONG, L. N. Y. 2013. Crack initiation, propagation and coalescence in rock-like material containing two flaws: a numerical study based on bonded-particle model approach. *Rock mechanics and rock engineering,* 46**,** 1001-1021.

ZHANG, Z. & WANG, Y.-H. 2014. Examining setup mechanisms of driven piles in sand using laboratory model pile tests. *Journal of Geotechnical and Geoenvironmental Engineering,* 141**,** 04014114.

ZHANG, Z. & WANG, Y.-H. 2016. DEM modeling of aging or creep in sand based on the effects of microfracturing of asperities and evolution of microstructural anisotropy during triaxial creep. *Acta Geotechnica,* 11**,** 1303-1320.